Department of Physics and Astronomy

University of Heidelberg

Master thesis

in Physics

submitted by

Bastian Bernarding

born in Wiesbaden

2016

Towards Unfolding Topologies

Proof of Concept within a Monojet Analysis

This Master thesis has been carried out by Bastian Bernarding

at the

Kirchhoff-Institute for Physics

under the supervision of

Dr Monica Dunford

Abstract

The process of unfolding is used in particle physics to obtain kinematic distributions which are independent of the detector. This study explores the potential of a new unfolding method. This method aims at unfolding an inclusive reconstructed data distribution without performing any background subtraction and is referred to as topology unfolding. The results of topology unfolding in the framework of a monojet analysis are compared to the ones from a conventional unfolding method and are shown to be consistent with these results. The new method of topology unfolding can reduce the overall uncertainties of the unfolded distributions by 20 % to 80 % at high energies due to using the full statistical power of the reconstructed distribution and a robustness of the topology unfolding matrix. In addition to the validation of the new method, exclusion limits on the fundamental Planck scale in the ADD model are derived at reconstruction and at particle level using the event selection of a typical monojet search and the 2015 data set of proton-proton collisions recorded at the Large Hadron Collider corresponding to an integrated luminosity of $3.2\,\mathrm{fb}^{-1}$. The limits obtained from topology unfolding are shown to be consistent with the limits at reconstruction level as well as with the limits obtained from the conventional way of unfolding.

Zusammenfassung

Der Prozess der Entfaltung wird in der Teilchenphysik genutzt um Verteilungen kinematischer Variablen zu erhalten, die den großen Vorteil haben, nicht von dem Detektor abzuhängen mit dem sie gemessen wurden. Diese Arbeit erforscht die Möglichkeiten einer neuen Entfaltungsmethode. Diese Art der Entfaltung zielt darauf ab, eine inklusive rekonstruierte Verteilung zu entfalten ohne eine Subtraktion des Untergrundes vorzunehmen und nennt sich Topologieentfaltung. Die Ergebnisse der Topologieentfaltung im Rahmen einer Monojet-Analyse werden mit denen einer etablierten Entfaltungsmethode verglichen. Der Vergleich zeigt konsistente Ergebnisse zwischen beiden Methoden, wobei die Topologieentfaltung die Gesamtunsicherheit der entfalteten Verteilungen um 20 % bis 80 % im Bereich hoher Energien reduzieren kann. Der Grund für diese Reduktion liegt darin, dass die neue Methode die volle Statistik der rekonstruierten Verteilung nutzt und die Entfaltungsmatrix dieser Methode eine gewisse Robustheit zeigt. Zusätzlich werden Ausschlussgrenzen auf die fundamentale Planck-Skala im Rahmen des ADD Modells auf Rekonstruktions- und Teilchenebene bestimmt, wobei die Ereignisselektion einer typischen Monojet-Suche und die Proton-Proton Kollisionsdaten genutzt werden, die von dem Großen Hadronen-Speicherring im Jahre 2015 aufgenommen wurden und einer integrierten Luminosität von $3.2\,\mathrm{fb}^{-1}$ entsprechen. Die Ausschlussgrenzen, die unter Anwendung der Topologieentfaltung erhalten werden, stimmen sowohl mit den Ausschlussgrenzen auf Rekonstruktionsebene als auch mit den Ausschlussgrenzen, welche durch eine etablierte Entfaltungsmethode bestimmt werden, überein.

Contents

Introduction

Unfolding is a powerful concept that results in a sustainable way of how experimental physicists can present their results. This thesis represents a proof of concept study that validates an new method of unfolding and starts to explore its possibilities. In addition, it is a general motivation for using unfolding techniques in searches for new physics. The thesis is structured as follows. In section 1.1 the Standard Model of particle physics is reviewed and the monojet signature introduced, together with the ADD model. Chapter 2 discusses the ATLAS experiment at the Large Hadron Collider and explains the origin of particle jets at collider experiments. A general motivation for unfolding is given in chapter 3 followed by an explanation of the topology unfolding method. In chapter 4, the validation of the topology unfolding technique is performed using Monte Carlo simulations and the event selection of a typical monojet search. Finally, the topology unfolding is applied to a realistic monojet search in chapter 5 using proton-proton collision data recorded in 2015 by the Large Hadron Collider in order to set limits at reconstruction and particle level on the fundamental Planck scale of the ADD model.

1. The Standard Model of particle physics and beyond

1.1. The Standard Model

The Standard Model (SM) of particle physics is a renormalizable gauge theory which describes the electromagnetic, the weak and the strong interactions of elementary particles through the exchange of spin one gauge bosons. Gravity is not included. The underlying local gauge symmetry is $SU(3)_C \times SU(2)_L \times U(1)_Y$, which gets reduced to $SU(3)_C \times U(1)_Q$ through the mechanism of spontaneous electroweak symmetry breaking. The algebra of the group corresponding to the symmetry $SU(3)_C \times SU(2)_L \times U(1)_Y$ is generated by the Gell-Mann matrices, the Pauli matrices and the hypercharge operator Y. The SM of particle physics was constantly under development starting from the middle of the last century. The development was driven by principles of symmetries, more importantly principles of approximate symmetries, new ideas that emerge while facing major difficulties in the fundamental understanding of the nature of particle physics and the always present ambition to match the constantly growing experimental knowledge of particle physics. Some of these important new ideas are

- the idea that (local) gauge symmetries should dictate the form of a theory's interactions, which was put forward by Yang and Mills in the 1950s by constructing a non-abelian gauge theory based on $SU(2)$ hoping to find a theory of the strong interactions,
- the quark model proposed by Gell-Mann and Zweig in the 1960s, which brought order into the growing menu of hadrons known at that time,
- the idea of a symmetry of the Lagrangian which is not a symmetry of the vacuum (spontaneous symmetry breaking) later on used to produce mass terms for gauge bosons and fermions. [1]

This section reviews briefly the current form of the SM. The particle content of the SM is summarized in figure 1.1. It consists of twelve spin one gauge bosons being the mediators of the three fundamental interactions, twelve fermions with spin one half which can be divided into six leptons and six quarks and the Higgs boson with spin zero. In addition, an antiparticle exists to each fermion having the same properties but opposite charge compared to its fermion partner.

Electroweak Interaction The electromagnetic and the weak interactions were unified into the so-called electroweak theory based on $SU(2)_L \times U(1)_Y$ by Glashow [3] in 1961. This unification is often seen as the first step towards the SM of particle physics in its current form. The Lagrangian of the electroweak interaction can be divided into a part describing the dynamics and self interaction of the gauge bosons and a part describing the interaction of the fermions with the gauge bosons. The Lagrangian of the gauge

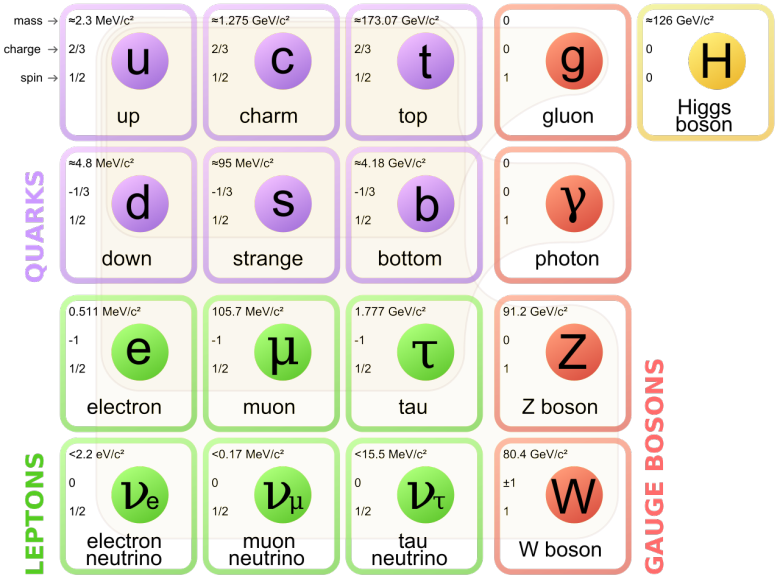

Figure 1.1.: The particle content of the SM: twelve spin one gauge bosons (eight gluons, Z, $W^{\pm}$ and the photon), six leptons and six quarks together with their antiparticles (not shown here) and the Higgs boson [2].

sector is

$$\mathcal{L}_{\text{gauge}} = -\frac{1}{4}W^a_{\mu\nu}W^{a\mu\nu} - \frac{1}{4}B_{\mu\nu}B^{\mu\nu}, \tag{1.1}$$

where $B_{\mu\nu} = \partial_\mu B_\nu - \partial_\nu B_\mu$ is the field strength tensor of the $U(1)_Y$ hypercharge interaction with B_μ being the gauge boson of the electromagnetic interaction and $W^a_{\mu\nu} = \partial_\mu W^a_\nu - \partial_\nu W^a_\mu + ig\epsilon^{abc}W^b_\nu W^c_\mu$ the field strength tensor of the $SU(2)_L$ weak interaction with ϵ^{abc} being the Levi-Civita tensor and a, b, c running from 1 to 3 refering to the three gauge bosons of the weak interaction W^a_μ. The constant g is the coupling constant of the weak interaction. The interaction and the kinematic terms for the leptons are given by

$$\mathcal{L}_{\text{leptons}} = \sum_i i\bar{l}_{L,i}\gamma^\mu(\partial_\mu + igW^a_\mu\sigma^a/2 + ig'Y_{l_{L,i}}B_\mu)l_{L,i} \tag{1.2}$$

$$+ i\bar{e}_{R,i}\gamma^\mu(\partial_\mu + ig'Y_{l_{R,i}}B_\mu)e_{R,i}, \tag{1.3}$$

where i runs over the three lepton flavors, $L_{L,i} = (\nu_{L,i}, e_{L,i})^T$ is the left-handed lepton doublet under $SU(2)_L$, $e_{R,i}$ the right-handed singlet under $SU(2)_L$ of flavor i and g' the coupling constant of the electromagnetic interaction. Here, it was introduced by hand that the gauge bosons W^a_μ of $SU(2)$ couple only to left-handed particles in order to match experimental observations. The electroweak Lagrangian for the quarks is constructed in a similar way

$$\mathcal{L}_{\text{quarks}} = \sum i\bar{Q}_{L,i}\gamma^\mu(\partial_\mu + igW^a_\mu\sigma^a/2 + ig'Y_{Q_{L,i}})Q_{L,i} \tag{1.4}$$

$$+ i\bar{u}_{R,i}\gamma^\mu(\partial_\mu + ig'Y_{u_{R,i}}B_\mu)u_{R,i} \tag{1.5}$$

$$+ i\bar{d}_{R,i}\gamma^\mu(\partial_\mu + ig'Y_{d_{R,i}}B_\mu)d_{R,i}, \tag{1.6}$$

where i runs over the three quark families, $Q_{L,i} = (u_{L,i}, d_{L,i})^T$ is the left-handed quark doublet under $SU(2)_L$ and $u_{R,i}$ and $d_{R,i}$ the right-handed quark singlets under $SU(2)_L$.

The electroweak unification identifies the physical states of the photon A_μ and the Z_μ boson as a mixture of the gauge boson B_μ of $U(1)_Y$ and the gauge boson W_μ^3 of $SU(2)_L$ as follows

$$\begin{pmatrix} A_\mu \\ Z_\mu \end{pmatrix} = \begin{pmatrix} \cos\theta_w & \sin\theta_w \\ -\sin\theta_w & \cos\theta_w \end{pmatrix} \begin{pmatrix} B_\mu \\ W_\mu^3 \end{pmatrix}, \tag{1.7}$$

where θ_w is the mixing angle. According to this, the part of the electroweak Lagrangian for the quarks and leptons can be written in the following form, which reflects better the underlying interactions

$$\mathcal{L}_{\text{leptons}} = \sum_i i\bar{\nu}_{L,i}\gamma^\mu\partial_\mu\nu_{L,i} + i\bar{e}_i\gamma^\mu\partial_\mu e_i + e\bar{e}_i\gamma^\mu A_\mu e_i \tag{1.8}$$

$$- \frac{e}{2\sin 2\theta_w}\nu_i\gamma^\mu(1-\gamma^5)Z_\mu\nu_i + \frac{e}{2\sin 2\theta_w}\bar{e}_i\gamma^\mu(1-4\sin^2\theta_w-\gamma^5)e_iZ_\mu \tag{1.9}$$

$$- \frac{e}{2\sqrt{2}\sin\theta_w}\nu_i\gamma^\mu(1-\gamma^5)W_\mu^+e_i - \frac{e}{2\sqrt{2}\sin\theta_w}\bar{e}_i\gamma^\mu(1-\gamma^5)W_\mu^-\nu_i \tag{1.10}$$

with $e_i = e_{L,i} + e_{R,i}$ and $W_\mu^\pm = 1/\sqrt{2}(W_\mu^1 \mp iW_\mu^2)$ being the physical W bosons. Since the Z_μ boson is a mixture of B_μ and W_μ^3 it couples to both right- and left-handed leptons but with different strength. The $W_\mu^\pm$ bosons couple only to left-handed particles. This chiral structure is called $V-A$ (vector minus axial) interaction and breaks parity explicitly. Similarly, the electroweak Lagrangian for the quarks turns into

$$\mathcal{L}_{\text{quarks}} = \sum_i iu_i\gamma^\mu\partial_\mu u_i + id_i\gamma^\mu\partial_\mu d_i - \frac{2}{3}e\bar{u}_i\gamma^\mu A_\mu u_i + \frac{1}{3}e\bar{d}_i\gamma^\mu A_\mu d_i \tag{1.11}$$

$$- \frac{e}{2\sin 2\theta_w}\bar{u}\gamma^\mu(1-\frac{8}{3}\sin^2\theta_w-\gamma^5)Z_\mu u_i + \frac{e}{2\sin 2\theta_w}\bar{d}_i\gamma^\mu(1-\frac{4}{3}\sin^2\theta_w-\gamma^5)Z_\mu d_i \tag{1.12}$$

$$- \frac{e}{2\sqrt{2}\sin\theta_w}\bar{u}_i\gamma^\mu W_\mu^+(1-\gamma^5)d_i - \frac{e}{2\sqrt{2}\sin\theta_w}\bar{d}_i\gamma^\mu W - \mu^-(1-\gamma^5)u_i, \tag{1.13}$$

with $u_i = u_{L,i} + u_{R,i}$ and $d_i = d_{L,i} + u_{R,i}$.

Higgs mechanism Introducing mass terms for fermions and gauge bosons by hand would break explicitly the $SU(2)_L \times U(1)_Y$ local gauge symmetry. To avoid breaking the symmetry in an explicit way, the Higgs mechanism is used for creating mass terms. It introduces a complex scalar $SU(2)_L$ doublet H which can be written as

$$H = \begin{pmatrix} 0 \\ \frac{h+v}{\sqrt{2}} \end{pmatrix} \tag{1.14}$$

in unitary gauge with a vacuum expectation value $v \neq 0$. The extension of the SM Lagrangian involving the new doublet is defined as

$$\mathcal{L}_{\text{Higgs}} = (D_\mu H)^\dagger(D^\mu H) - V_H, \tag{1.15}$$

where $D_\mu = \partial_\mu + igW_\mu^a\sigma^a/2 + ig'\frac{1}{2}B_\mu$ is the covariant derivative and V_H the Mexican hat potential

$$V_H = -\mu^2H^\dagger H + \lambda(H^\dagger H)^2, \tag{1.16}$$

with $\lambda > 0$ and $-\mu^2 < 0$. The kinetic term of the Higgs doublet couples the Higgs boson h to the gauge bosons. This results in a mass term for $W_\mu^\pm$ and Z_μ but not for the photon and in interaction between the Higgs particle h and the massive gauge bosons. The masses of the gauge bosons are proportional to the vacuum expactation value v of the Higgs doublet. The fermion masses are generated by adding the so-called Yukawa couplings

$$\mathcal{L}_{\text{Yukawa}} = \sum_i y_{l,i} \bar{l}_{L,i} H e_{R,i} + y_{u,i} \bar{Q}_{L,i} \tilde{H} u_{R,i} + y_{d,i} \bar{Q}_{L,i} H d_{R,i} \tag{1.17}$$

to the Lagrangian of the SM, with $\tilde{H} = i\sigma_2 H^*$. This results in mass terms for the fermions proportional to v and also couplings between the massive fermions and the Higgs boson h. Having the mass terms for fermions and bosons included, the system with a non-zero vacuum expactation value is no longer invariant under $SU(2)_L \times U(1)_Y$ transformations. However, this (spontaneous) breaking of the symmetry through a non-zero vacuum expectation value is from a conceptional point of view a better founded approach than breaking the symmetry explicitly by just inserting mass terms by hand to match the observation of massive particles. It stresses the general importance of principles connected to gauge symmetries for the description of nature.

Strong interaction The strong interaction refers to the interaction of objects which carry color charge, namely quarks and gluons, and is described by the theory of Quantum Chromodynamics (QCD). QCD is a non-abelian gauge theory based on the $SU(3)_C$ gauge group with the following Lagrangian

$$\mathcal{L}_{\text{QCD}} = -\frac{1}{4}(G^a_{\mu\nu} G^{a\mu\nu}) + \sum_i \bar{q}_{i,\alpha} i\gamma^\mu \partial_\mu q_{i,\alpha} - g_s \sum_i \bar{q}_{i,\alpha} \gamma^\mu G^a_\mu (\lambda^a/2)^{\alpha\beta} q_{i,\beta}, \tag{1.18}$$

where the index i runs over all quark flavors (u, d, c, s, t, b), α is the color index (r, g, b), λ^a are the Gell-Mann matrices ($a = 1, ..., 8$) and g_s the couplings constant of the strong interaction. $q_{i,\alpha}$ is the quark field spinor of a quark with flavor i and color α. The gluon field strength tensor is defined as $G^a_{\mu\nu} = \partial_\mu G^a_\nu - \partial_\nu G^a_\mu + i g_s f^{abc} G^b_\mu G^c_\nu$ with G^a_μ being the eight gluon fields and f^{abc} the structure constants of $SU(3)_L$. The first term of the Lagrangian is the kinetic term of the gluons including their self interactions with triple and quartic gluon vertices. The self interaction arise from the non-abelian structure of QCD ($[G_\mu, G_\nu] \neq 0$ with $G_\mu = G^a_\mu \lambda^a/2$) and gives rise to two important features of the theory: color confinement and asymptotic freedom. The second term is the kinematic term of the quarks. The last term describes the interaction between two quarks and a gluon.

Color confinement is a hypothesis which states that colored objects are always confined to color singlet states and therefore objects with color charge cannot propagate as free particles. This hypothesis is used to explain why free quarks have never been observed in experiments, although there is no analytic proof for this concept. The idea arises from the fact that the strong force between two colored objects increases linearly with the distance as a result of the self interaction of the gluons. For this reason the existence of two free objects with color charge separated at a macroscopic distance would correspond to an enormous amount of energy stored in the gluon field between them. Therefore, colored objects arrange themselves into colorless hadrons. In section 2.4 it will be discussed in more details how the color confinement is responsible for the production of particle jets.

Asymptotic freedom refers to the fact that the strong interaction gets reduced with increasing energies or decreasing distances and quarks asymptotically act as free particles.

At low energies the strong coupling $\alpha_s \propto g_s$ is of the order $\mathcal{O}(1)$ and therefore perturbation theory cannot be applied. However, going to higher energies α_s approaches smaller values entering the perturbative regime. This running of α_s is mainly determined by the gluon self interaction and strongly connected to the concept of renormalization, which is not further discussed here. The term asymptotic freedom might be misleading to some extend since it could imply that predictions can be made for high energy experiments on the basis of quasi-free particles and therefore leading order calculations. However, even at the energies of modern particle physics experiments α_s is still large enough ($\alpha_s \approx 0.1$ at 100 GeV) so that higher-order corrections cannot be neglected.

1.2. Physics beyond the Standard Model

The SM of particle physics managed to withstand an enormous amount of experimental tests and represents up to now the best theory of the interaction of nature's fundamental particles. The process of mankind understanding nature and the world of fundamental particles is constantly developing and great progress could be achieved also during the last decades.

Most importantly, the Higgs boson being the only particle of the SM which had not been observed was discovered in 2012 [4, 5]. Because the idea of generating mass through the Higgs mechanism is deeply connected to the conceptual difference between breaking a gauge theory explicitly or keeping the symmetry of the Lagrangian but breaking it through the vacuum, the experimental confirmation of the Higgs mechanism showed above all that quantum field theory in form of a renormalizable gauge theory really is the right way to describe interactions between elementary particles. Furthermore, the observation of neutrino oscillation [6, 7] revealed that neutrinos do have mass and that the accidental lepton flavor symmetry of the SM is, at least in the uncharged leptonic sector, broken. Other fields of physics closely related to particle physics, like e.g. cosmology, also discovered new insights on nature and the universe. For example, the observation of supernovae revealed that the expansion of the universe undergoes a positive acceleration [8] and the structure of the cosmic microwave background strongly suggest that we live in a flat universe [9], which is the only mathematically beautiful universe. Despite these ongoing achievements in understanding nature and the universe, several questions remain unanswered and also the SM of particle physics incorporates some shortcomings. Currently, one of the major drawbacks of the SM is the fact that it does not provide a particle with suitable properties which could serve as a dark matter candidate in order to explain the overwhelming experimental evidence for dark matter. Dark matter is believed to be a new type of massive particle that might interact with the SM particles through the weak interaction. Evidence for dark matter is found e.g. in observing the motions of galaxies [10], gravitational lensing [11] as well as angular fluctuations in the cosmic microwave background [9]. In 2016, a galaxy has been observed which is believed to consist almost only (98 %) out of dark matter [12]. Furthermore, it has not been possible so far to include the gravitational interaction to the SM. In addition, it is unclear what mechanism is responsible for giving mass to neutrinos. The SM also does not provide an answer for the question of the matter antimatter asymmetry in the universe. Another conceptional difficulty is the so-called hierarchy problem which will be discussed in the following section. New ideas and theories are developed to address these shortcomings of the SM. The predicitons done by these new theories describing physics beyond the SM is tested in experiments. The model that is tested in this thesis is the so-called ADD model which addresses the hierarchy problem and is also discussed in the following section.

1.2.1. The hierarchy problem and large extra dimensions

The hierarchy problem rises the question why the electroweak scale ($\mathcal{O}(1000\,\mathrm{GeV})$) is so much smaller than the Planck scale ($\approx 10^{19}\mathrm{GeV}$), the scale at which quantum gravity becomes as relevant as the gauge interactions of the SM. In other words the hierarchy problem asks for a reason explaining why the gravitational interaction is so weak. This problem is connected to the question why the mass of the Higgs boson is relatively small although its loop corrections are quadratically sensitive to higher energy scales. After the naturalness criterion of G. 't Hoof [13], a physical parameter is allowed to have a small value only if the replacement of that value by zero would increase the symmetry of the system. For example, small fermion masses would be allowed in the SM because for $m_f = 0$ the SM Lagrangian would recover an additional chiral symmetry that allows to rotate left- and right-handed fermions independently. But for the Higgs mass such a symmetry does not exist in the SM.

The ADD model [14] is one of the theories that addresses the hierarchy problem. This model postulates the unification of gravitational and gauge interactions at the electroweak scale. The weakness of gravity is explained by the existence of $n \geq 2$ large compactified extra spatial dimensions. Gravitons can freely propagate in the new dimensions while SM particles are mostly localized in the usual four dimensions. The Planck scale is considered as not being a fundamental scale and its large value is connected to the size of the extra dimensions. For n extra dimensions with a radius R, Gauss's law for two masses with a distance r would be modified to

$$V(r) = \frac{m_1 m_2}{M_D^{n+2}} \frac{1}{r^{n+1}} \qquad \text{for } r \ll R, \tag{1.19}$$

where M_D is the new Planck scale for $n+2$ dimensions. For larger distances the usual $1/r$ potential

$$V(r) = \frac{m_1 m_2}{M_D^{n+2} R^n} \frac{1}{r} \qquad \text{for } r \gg R \tag{1.20}$$

is recovered because the gravitational flux lines cannot penetrate the extra dimensions at these distances. The effective Planck scale for n extra dimensions is therefore connect to the normal Planck scale M_{Pl} via

$$M_{\mathrm{Pl}}^2 \propto M_D^{n+2} R^n. \tag{1.21}$$

Assuming M_D at the order of the electroweak scale in order to solve the hierarchy problem the modification of the gravity potential would not be noticeable for $n \geq 2$ at distances that can be probed by modern high precision experiments measuring gravity. However, the ADD model could result in possible signals in hardon collider experiments. The following section describes how such a signal predicted by the ADD model could look like.

1.3. Monojet signature in searches

An event with a large amount of missing transverse energy and one high energetic jet is referred to as *monojet signature*. It is one of the leading signatures in the search for dark matter particles and gravitons at the LHC. In the SM, mainly events from $Z \to \nu\nu$ decays and leptonically decaying W bosons result in a monojet signature. Many theories describing physics beyond the SM predict additional contributions to this event topology.

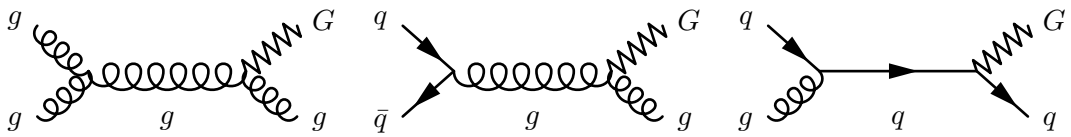

(a) (a) (a)

Figure 1.2.: Feynman diagrams for three different graviton (G) production mechanisms involving quarks and gluons in the initial and final state.

Especially, theories providing a suitable dark matter candidate predict processes that would increase the event yield of a monojet search. In addition, the ADD model, discussed in the previous section, would also contribute to this signature, if it was realized in nature. Figure 4.1 shows three different mechanism in which a graviton and a gluon or a quark are produced in the final state. The graviton produces a large amount of missing transverse energy and the outgoing quark or gluon is observed as a high energetic jet of particles (discussed in section 2.4) and therefore the event results into a monojet signature. From an experimental point of view it is interesting that the cross section σ_{ADD} of the graviton production is independent of the mass m_0 of the graviton and that it holds

$$\sigma_{ADD} \propto \frac{1}{M_D^{n+2}}, \tag{1.22}$$

with M_D being the fundamental Planck scale and n being the number of extra dimensions. This relation will be used later on to translate the limit on the cross section into a limit on the fundamental Planck scale M_D.

The searches for dark matter particles or gravitons using monojet signatures define an event selection optimized for this signature and examine a possible excess of events in the tail of the missing energy distribution. The sensitivity of these searches depends strongly on how precise the SM background can be determined. To minimize the uncertainty on the background estimate, (semi) data-driven strategies are used for the dominant backgrounds. However, theoretical predictions in form of Monte Carlo (MC) simulations are still needed for the background determination in most cases. Typically, the searches are limited by the uncertainty of the jet energy scale and theoretical uncertainties coming e.g. from the choice of the renormalization and factorization scale or the parton density function. In chapter 3 the conventional way of such a search and its limitations are discussed in more detail. In addition, an alternative is proposed involving the new method of *topology unfolding* that can be used in searches for new physics.

2. The ATLAS experiment

The following chapter introduces the ATLAS experiment at the Large Hadron Collider (LHC). After a brief review of the LHC (section 2.1) the most important physics aspects of detecting particles are discussed in section 2.2, followed by a description of the ATLAS detector in section 2.3. In addition, a discussion of particle jets is presented in section 2.4, since the event signature used in this thesis is mainly based on jets and missing transverse energy.

2.1. Large Hadron Collider

The LHC is the world's largest particle collider located at CERN[1] near Geneva. It is a cricular hadron collider located in a tunnel, which hosted previously the Large Electron Positron collider (LEP), with a circumference of 27 km about 100 m below ground level. The LHC is designed to perform mainly proton-proton but also heavy ion collisions at a center-of-mass energies up to 14 TeV. For the LHC, the limitating factor concerning the center of mass energy is the bending power which is necessary to keep the protons inside the ring. Over one thousand superconducting dipole magnets are needed for this purpose being able to produce a magnetic field of up to 8.4 T. For proton-proton collisions, two separate beam pipes contain so-called bunches of $\mathcal{O}(10^{11})$ protons with a distance of 25 ns. After being pre-accelerated in a system of smaller accelerators the protons reach their final energy in the ring of the LHC. At the location of the experiments the two beams get strongly focused and their lines intersect so that a collision can occur. The measure that describes the proton beams is the instantaneous luminosity $\mathcal{L}_{inst}$ defined as

$$\mathcal{L}_{inst} = \frac{nN_1N_2f}{4\pi\sigma_x\sigma_y}, \tag{2.1}$$

where n is the number of bunches, N_1 (N_2) the number of protons in the first (second) beam, f the frequency of bunch collisions and $\sigma_{x,y}$ the root-mean-squared horizontal and vertical beam sizes. Since the instantaneous luminosity is directly proportional to the event rate, it is desired to be as high as possible. This means that the number of protons per bunch and the number of bunches are desired to be maximized whereas the distance between the bunches and the bunch beam size are desired to be minimized. The integrated luminosity $\mathcal{L}$ is obtained by integrating the instantaneous liminosity over time

$$\mathcal{L} = \int \mathcal{L}_{inst}\mathrm{d}t. \tag{2.2}$$

The data sample of proton-proton collisions which is used in this thesis was recorded in 2015 and corresponds to an integrated luminosity of $\mathcal{L} = 3.2\,\mathrm{fb}^{-1}$ at a center of mass energy of $\sqrt{s} = 13\,\mathrm{TeV}$.

[1] CERN - European Organisation for Nuclear Research

Besides the ATLAS[2] experiment there are three other main experiments at the LHC: ALICE[3], CMS[4] and LHCb[5]. The physics program of ATLAS and CMS is dedicated to the discovery of the Higgs boson as well as precision measurements of parameters of the SM. In addition, searches for physics beyond the SM are performed. The focus of the ALICE experiment is to study the so-called quark-gluon plasma in heavy ion collisions, a hypothetical state of matter which is expected to exist at extremely high temperatures and densities and in which the universe might have found itself right after the Big Bang. The LHCb experiment is designed to shed light on the matter antimatter asymmetry of the universe and studies therefore the CP violation in rare b quark decays. [15]

2.2. Physics of particle detection

All kind of particle detectors are based on how the particles that should be detected interact with matter. The way and the magnitude of the interaction is different for each kind of particle, which is used to identify and distinguish different kinds of particles in collider experiments.

Ionization and tracking When a relativistic, *charged* particle passes through matter, it interacts with the atomic electrons of the medium through the electromagnetic force. The particle can ionize the atoms and therefore loses energy. This energy loss $\frac{\mathrm{d}E}{\mathrm{d}x}$ is described by the Bethe-Bloch equation

$$\frac{\mathrm{d}E}{\mathrm{d}x} \approx -4\pi\hbar^2 c^2 \alpha^2 \frac{nZ}{m_e v^2} \left(\ln \left[\frac{2\beta^2\gamma^2 c^2 m_e}{I_e} - \beta^2 \right] \right). \tag{2.3}$$

Here, $v = \beta c$ is the velocity of the particle, Z the atomic number, n the number density and I_e the effective ionization potential of the material. Because of the $1/v^2$ term, the energy loss due to ionization is larger for low-velocity particles. In modern particle physics, often very high velocities of particles occur diminishing the influence of energy loss due to ionization. However, for one type of relativistic particles ionization is the dominant mechanism of how to lose energy in a detector. This is the case for *muons* with energies below 100 GeV, because other mechanisms like Bremsstrahlung is suppressed for these particles, as discussed later. Therefore, since the energy lost through ionization of high relativistic particles is quite moderate, muons travel significant distances even in dense materials and so reach into the outermost regions of a detector, where other particles cannot get.

The fact that charged particles ionize the material and leave a trail of ionized atoms and liberated electrons is used to measure their trajectories, referred to as *tracking*. There are mainly two techniques of how to measure this ionization of the material. First, large gaseous volumes can be used in which a strong electric field accelerates the freed electrons towards sense wires where they producing a signal. The second technique is based on semiconductor technology, often based on silicon. Here, the traversing charged particle creates typically $\mathcal{O}(10.000)$ electron-hole pairs in an appropriately doped wafer through ionization. Again, an electric field is applied and the holes drift in its direction before being collected by p-n junctions. Several hits in different layers of wafers can be combined into a track. In addition, a strong magnetic field, e.g. in the direction of the beam axis

[2] ATLAS - A Toroidal LHC Apparatus
[3] ALICE - A Large Ion Collider Experiment
[4] CMS -Compact Muon Solenoid
[5] LHCb - Large Hadron Collider Beauty

of a collider experiment, can be applied to bend the trajectories of charged particles due to the Lorentz force. This is used to perform a momentum measurement because the bending radius R is proportional to the momentum p of the particle $R \propto p$.

Bremsstrahlung, pair production and electromagnetic calorimeters Bremsstrahlung refers to a charged particle that radiates a photon in the electrostatic field of a nucleus. For relativistic *electrons*, this represents a much larger effect compared to ionization, which is only dominant below roughly $800\,\mathrm{MeV}/Z$ for this kind of particle. The rate of bremsstrahlung is inversely proportional to the square of the particle's mass

$$R \propto \frac{1}{m_e^2}. \tag{2.4}$$

Since electrons are much lighter than muons, bremsstrahlung gives rise to a much higher loss of energy for electrons. Muons are, because of their relatively large mass, dominated by ionization.

Pair production is the dominant interaction of *photons* with an energy $> 10\,\mathrm{MeV}$ and describes the process in which the photon annihilates into an electron and a positron in the electromagnetic field of a nucleus. The photoelectric effect, dominant at low energies and the Compton scattering process, starting to be dominant around 1 MeV are of subdominant importance for high energy particle physics experiments compared to pair production.

The raditational length X_0, being the average distance over which electrons lose $1/e$ of their energy, characterizes the electromagnetic interactions of high energy electrons and photons in matter. It is approximately proportional to

$$X_0 \propto \frac{1}{nZ^2 \ln(287/Z^{1/2})} \tag{2.5}$$

and therefore shorter for materials with a high atomic number Z. Roughly, it is equal to 7/9 of the mean free path of the pair production process for a high relativistic photon. When high energetic photons or electrons traverse matter, they create a so called electromagnetic shower which describes the alternation between bremsstrahlung and pair production which results in a cascade of electrons, positrons and photons. Such a electromagnetic shower can be detected by a calorimeter. The calorimeter can for example consist of optically transparent crystals with a short radiation length, in which the electrons of the shower produce scintillation light measured by photon detectors. Here, the amount of the scintillation light is proportional to the total energy of the incoming electron or photon. An alternative approach to that consist of using two types of alternating material layers (sampling calorimeter), one type being the passive high Z-material layer in which the shower is mainly built and the other type being an active layer in which the ionization from electrons of the shower can be measured. Both types of electromagnetic calorimeter are used in modern high energy particle physics experiments and typical resolutions for electrons and photons with energy E can be found in the range of

$$\frac{\sigma_E}{E} = \frac{3\% - 10\%}{\sqrt{E}} \tag{2.6}$$

Strong interaction and hadronic calorimeters Charged and uncharged *hadrons* lose energy through a strong interaction with a nucleus while passing matter. Typically, 30%

of the initial energy is lost due to nuclear excitation and break-up. The strong interaction produces many new particles also interacting with the medium, building up a hadronic shower. Frequently occurring π^0 particles decay very rapidly into two photons, which results in the formation of an electromagnetic component of the shower. The nuclear interaction length λ_1 describes a hadronic shower. It is defined as the mean distance between two hadronic interactions. The nuclear interaction length of a material is much larger than its radiation length. Therefore, hadronic calorimeters, designed to measure the showers of hadrons, occupy more space inside a detector compared to electromagnetic calorimeters. For these kind of calorimeters, typically an alternating chain of thick layers of very dense materials and thin layers of an active material is used. Similar to the sampling type of the electromagnetic calorimeter, the shower develops in the passive material layers and its energy deposition is measured in the thin stripes of active material. The resolution of hadronic calorimeters is much worse compared to its electromagnetic counter part:

$$\frac{\sigma_E}{E} \geq \frac{50\%}{\sqrt{E}}. \tag{2.7}$$

This mainly comes from alternating amounts of electromagnetic components of a hadronic shower and alternating the amount of energy that is lost in nuclear break-up. [16]

2.3. The ATLAS detector

Since the physics program of the ATLAS experiment includes besides the discovery of the Higgs boson the precise measurement of SM parameters as well as a wide range of searches for physics beyond the SM, the ATLAS detector [17] is designed as a multi purpose detector in order to cope with many different signal signatures. It has a full 4π angular coverage around the beam pipe, a length of 46 meters and a diameter of 25 meters. In addition to the name giving system of toroidal shaped magnets, the ATLAS detector consists of three main systems: the inner detector, the calorimeter and the muon spectrometer, as can be seen in figure 2.1.

To describe the geometry of physics processes inside the ATLAS detector a right handed coordinate system is used. Its origin is the interaction point at the center of the detector. The positive x-axis points to the center of the LHC ring, the y-axis upwards and the z-axis in the direction of the beam line. Therefore, the $x-y$ plane, referred to as *transverse* plane, lies perpendicular to the beam line. The transverse momentum and the transverse energy

$$p_{\mathrm{T}} = \sqrt{p_{\mathrm{x}}^2 + p_{\mathrm{y}}^2} \qquad\qquad E_{\mathrm{T}} = \sqrt{E_{\mathrm{x}}^2 + E_{\mathrm{y}}^2} \tag{2.8}$$

are defined as the projection of the momentum and the energy into the transverse plane. The azimuthal angle ϕ is the angle in the transverse plane around the beam axis. The polar angel θ refers to the angle relative to the beam axis. Hence the transverse momentum and energy can be calculated as $p_{\mathrm{T}} = p\cos\theta$ and $E_{\mathrm{T}} = E\cos\theta$. Other important variables are the pseudorapidity which is defined as

$$\eta = -\ln\left(\tan\frac{\theta}{2}\right) \tag{2.9}$$

and the angular distance ΔR between two objects

$$\Delta R = \sqrt{(\phi_1 - \phi_2)^2 + (\eta_1 - \eta_2)^2}. \tag{2.10}$$

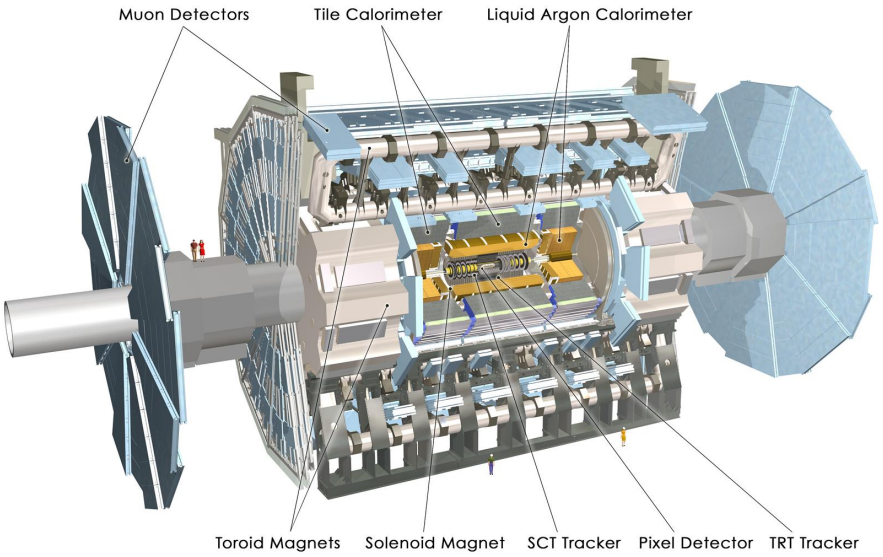

Figure 2.1.: The basic design of the ATLAS detector showing besides the magnet system the inner detector (Pixel Detector, SCT tracker and the TRT tracker), the calorimeter and the muon detectors [18].

The transverse and longitudinal impact parameters are calculated using the coordinates of the point of closest approach between a track and the primary vertex. The transverse impact parameter d_0 refers to the distance of this point to the primary vertex in the transverse plane and the longitudinal impact parameter z_0 is the distance in z direction.

2.3.1. The inner detector

The inner detector measures the momentum and trajectories of charged particles in the central region $|\eta| < 2.5$, performs particle identification and reconstructs the primary vertex as well as additional secondary vertices. It is located inside a magnetic field of 2 T produced by a solenoid magnet (figure 2.1) in order to bend the trajectories of charged particles through the Lorentz force for the momentum measurement. Figure 2.2 shows the layout of the inner detector in the central region of the detector. It consists of three subsystems. The semiconducting Pixel Detector (PD) is located closest to the interaction point and covers the region ($|\eta| < 2.5$). It consists of three cylindrical layers around the beam axis in the central region. Here, an additional pixel layer [19], referred to as the Insertable B-Layer (IBL), was added at a distance of 33 mm to the beam pipe during the first long shutdown of the LHC, which is not shown in figure 2.2. The installation of this additional layer was performed in order to improve the precision of measuring the tracks and vertex locations as well as to provide an increased tracking robustness for higher instantaneous luminosities. At the outer region of the detector the PD consists of discs perpendicular to the beam axis. The pixel sensors of the IBL have a size of $(R-\phi) \times z = 50\times\ 250\,\mu\text{m}$, the pixels sensors of the other three layers $50 \times 400\ \mu\text{m}^2$. The spatial resolution of the IBL is 10 µm in $(R-\phi)$ and 75 µm in z. For the other layers the accuracy is 10 µm in $(R-\phi)$ and 115 µm in z in the central region.

The Semiconductor Tracker (SCT) is, similar to the PD, split into four cylindrical layers in the central region. Each layer has silicon microstrips on the upper and the lower side of the layer. One set of stripes is oriented parallel to the beam direction, the second set of stripes is oriented orthogonal to the first one in order to measure both coordinates

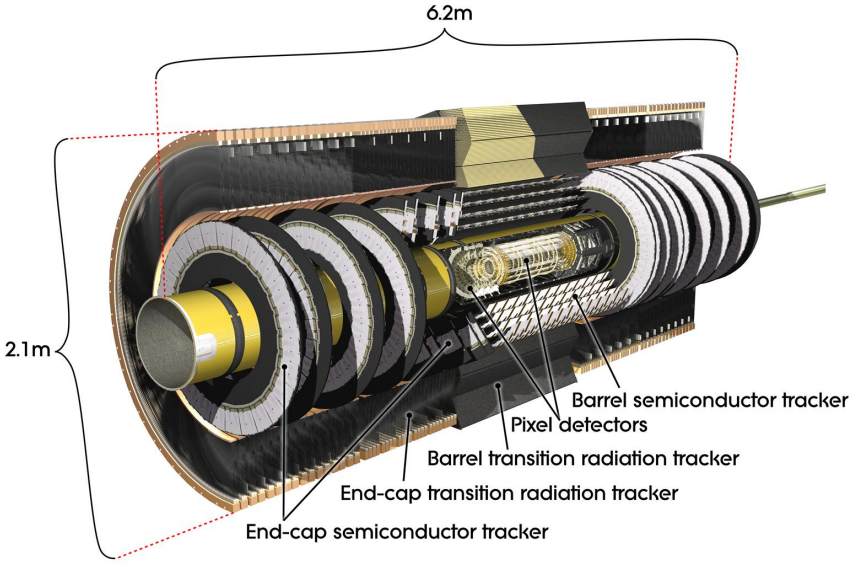

Figure 2.2.: Layout of the inner detector of ATLAS consisting of the Pixel Detector, the Semiconducting Tracker and the Transition Radiation Tracker [20].

($R-\phi$, z). In the outer region of the sub-detector the SCT consists of a set of disks on which microstrips are located radially around the beam axis. In the central region of the detector the SCT reaches an accuracy of 17 µm in $R-\phi$ and 580 µm in z.

The information provided by Transition Radiation Tracker (TRT) is used for tracking as well as for particle identification by measuring the transition radiation in the region $|\eta| < 2.0$. The TRT is built out of layers of straw tubes each with a diameter of 4 mm and filled with a gas mixture out of xenon, carbon dioxide and oxygen. A gold-plated tungsten wire in the center of each tube along its central axis serves as an anode. In the central region the tubes are orientated parallel to the beam axis. In the outer region the tubes are arranged radially around the beam axis. Therefore, the TRT provides only $R-\phi$ information with an accuracy of 130 µm. The transition radiation photons are absorbed in the gas mixture of the tubes yielding larger signal amplitudes than ionizing particles passing through the tubes. The transition radiation signal is distinguished from a simple tracking signal tube by tube with different thresholds in the front-end electronics. Since the mass of electrons is small compared to other particles they produce more transition radiation than other particles. Therefore, the transition radiation signal can be used to identify electrons.

As described, the inner detector of ATLAS makes use of both tracking techniques, semiconductor technology and gaseous volumes for ionization measurements, discussed in section 2.2. In 2015 [21] the resolution of the primary vertex position at a center of mass energy of 13 TeV was measured to be $\sigma_{x,y} \approx 20$ µm in the transverse plane and $\sigma_z \approx 40$ µm in z direction for a number of tracks associated to the vertex of 25 or higher. The IBL installation could improve the transverse (longitudinal) impact parameter resolution up to 40 % (60 %) [22]. The momentum resolution is measured with the 2015 dataset to be 1.7 % for muons in the central detector region coming from $J/\Psi \to \mu\mu$ decays [23].

2.3.2. The calorimeter

The calorimeter of the ATLAS detector measures the energy of particles and jets. In addition, the missing transverse energy of the event is calculated from the energy depositions in the calorimeter. Figure 2.3 shows the layout of the ATLAS calorimeter. It is divided into the electromagnetic calorimeter (ECAL) and the hadronic calorimeter (HCAL), both consisting of different parts, all of them being sampling calorimeters, discussed in section 2.2.

The ECAL is divided into the electromagnetic barrel and the two end-cap components. The electromagnetic barrel calorimeter covers the range $|\eta| < 1.475$ and the end-cap components measure particles between $1.375 < |\eta| < 3.2$. The ECAL uses liquid argon as active material and lead as the passive medium, combined in an accordion shape. Liquid argon was chosen because of its intrinsic linear behavior as well as a pronounced stability in the response over time and its hardness against radiation. Lead offers a high cross section for bremsstrahlung and pair production. The accordion shape provides the advantage of having multiple active layers in depth. The granularity of the ECAL is finest for the first layer of the electromagnetic barrel calorimeter ($\Delta\eta \times \Delta\phi = 0.025/8 \times 0.1$) providing a high precision for measuring electrons and photons. The total depth of the ECAL is 22 radiation length, long enough so that electrons and photons deposit (almost) their full energy in the ECAL. Jets and tau leptons also deposit a large amount of energy in the ECAL. However, their hadronic showers do not end in the ECAL and extend into the HCAL. The energy resolution of the ECAL was measured to be $\sigma_E/E \approx 10\,\%\sqrt{GeV}/\sqrt{E}$ [24].

The HCAL is placed outside the ECAL and consists of the tile calorimeter in the central region, the hadronic end-cap calorimeter and forward calorimeter. The tile calorimeter is divided into the tile barrel ($|\eta| < 1.0$) and two extended barrel components ($0.8 < |\eta| < 1.7$). In the tile calorimeter steel serves as the absorber material and scintillating tiles as the active component. The choice of using scintillating tiles provides a maximal radial depth at a relatively low financial budget. The hadronic end-cap calorimeters is located in the region $1.5 < |\eta| < 3.2$. Here, liquid argon is used as active material and copper as the passive material. The forward calorimeter covers the range $3.1 < |\eta| < 4.9$ and and consists of three different modules all using liquid argon as active material. The first module uses copper as passive material and is optimized for electromagnetic measurements. The other two modules are equipped with tungsten as absorber material and are designed for measuring mostly the energy of hadronic interactions. The energy resolution of the tile calorimeter was measured to be $\sigma_E/E \approx 53\,\%\sqrt{GeV}/\sqrt{E}$ [25]. The energy resolution of the hadronic end-cap calorimeter was determined to be $\sigma_E/E \approx 71\,\%\sqrt{GeV}/\sqrt{E}$ for pions [26]. The forward calorimeter showed an energy resolution of $\sigma_E/E \approx 29\,\%\sqrt{GeV}/\sqrt{E}$ for electrons and $\sigma_E/E \approx 94\,\%\sqrt{GeV}/\sqrt{E}$ for hadrons [27].

2.3.3. The muon spectrometer

The muon spectrometer of the ATLAS detector is designed to determine the momentum of muons by performing a precise measurement of their trajectories which are bent by the presence of a magnetic field. In addition, the muon spectrometer is used to trigger on muon tracks. Figure 2.4 shows the layout of the muon spectrometer. It is a combination of the large superconducting toroid magnets and a system of different types of gaseous tracking chambers for tracking.

In the central region of the detector ($|\eta| < 2.7$), Monitored Drift Tubes (MDT) chambers

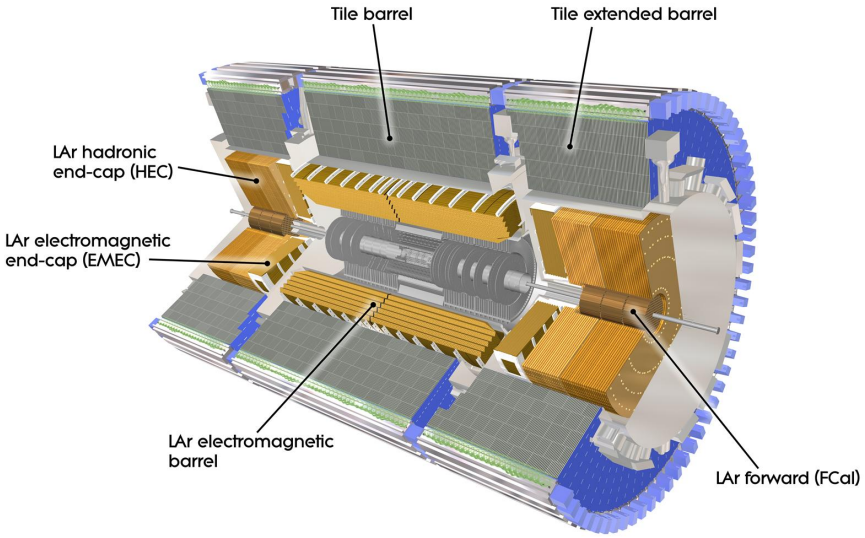

Figure 2.3.: Layout of the calorimeter of the ATLAS detector. The electromagnetic calorimeter consists of the barrel calorimeter and two end-cap components. The hadronic calorimeter is divided into the barrel and extended barrel component as well as the two-end cap and the forward calorimeter [28].

are used to precisely measure the tracks of muons. Each chamber consists of three to eight layers of pressurized drift tubes with a length of 30 mm filled with a mixture of Argon and carbon dioxide. The sense wire in the middle of each tube is made out of tungsten-rhenium and has a diameter of 50 µm and is operated at a voltage of around 3000 V. The MDTs give an average resolution of 80 µm per tube.

The innermost layer of the forward region $2 < |\eta| < 2.5$ is covered by Cathode-Strip Chambers (CSC), since they show a higher rate capability and better time resolution. The CSCs are multiwire proportional chambers. The wires are oriented in the radial direction with a diameter of 30 µm. The two cathodes are divided into strips. One set of strips is orthogonal to the wires, the other set of stripes parallel to the wires. Therefore, both coordinates can be measured. The gas mixture used inside the CSCs is also a mixture of argon and carbon dioxide. The operating voltage is 1900 V. The resolution is 60 µm per CSC plane.

In order to provide the capability to trigger on muon tracks, a system of fast trigger chambers is also installed in the muon spectrometer. The fast trigger chambers are needed to deliver track information within a very short period of time. In the central region ($|\eta| < 1.05$) Resistive Plate Chambers (RPC) and in the end-cap region ($1.05 < |\eta| < 2.4$) Thin Gap Chambers (TGC) are used for this purpose. The RPCs are gaseous parallel electrode-plate detectors, whereas the TGCs are specifications of multi-wire proportional chambers. These two types of trigger chambers can deliver signals within 15-25 ns. The momentum resolution of muons was measured [30] to be $\sigma_p/p \approx 0.25\text{TeV}/p_\text{T} \oplus 0.17 p_\text{T}/\text{TeV}$ in the central region of the detector. [17]

2.3.4. Trigger system

The trigger system of ATLAS [31] is an essential part of the experiment deciding if an event from a bunch-crossing should be recorded for further investigation. It underwent

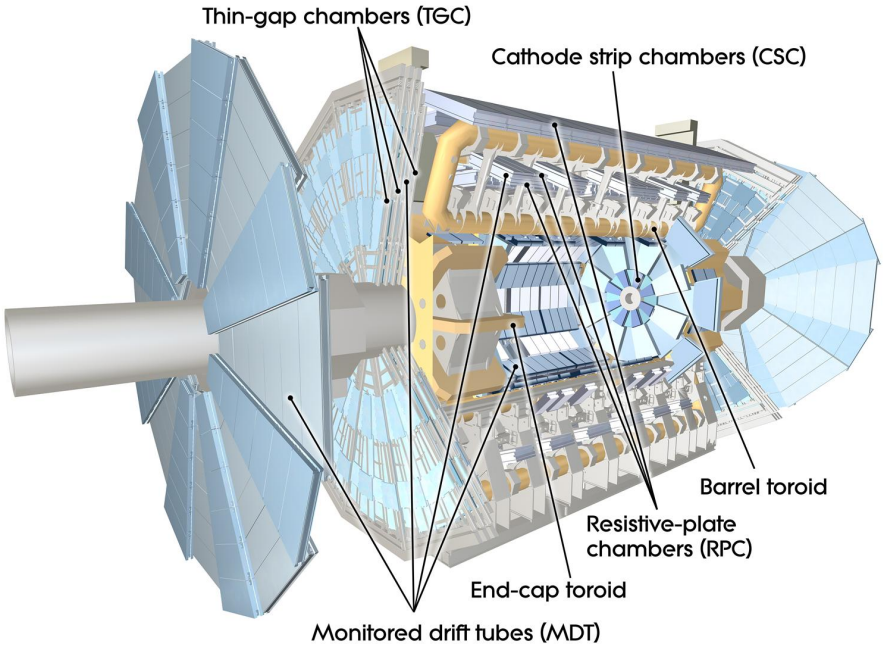

Figure 2.4.: The muon spectrometer and the outer magnet system. The muon spectrometer consists of Monitored Drift Tubes (MDT), Cathode Strip Chambers (CSC) as well as Resistive Plate Chambers (RPC) and Thin Gap Chambers (TGC) [29].

a major update during the first long shutdown of the LHC in 2013 and 2014 in order to improve its performance under an increased center of mass energy, higher luminosity as well as an increased number of proton-proton interactions per bunch crossing. The trigger system consists of a first-level trigger (L1) which is based on hardware and a high-level trigger (HLT), based on software.

The trigger decision on L1 is based on high energetic objects, like photons, electron, muons, tau leptons and jets as well as missing transverse energy. It is made by the Central Trigger Processor (CTP) based on information of the calorimeter and the muon system. The main systems used here are the L1 calorimeter trigger (L1Calo) and the L1 muon triggers.

The L1Calo trigger identifies regions of interest (RoI) and multiplicities for electrons, photons, taus and jets. It consists of the Preprocessor, the Cluster Processor and the Jet/Energy Processor. The Preprocessor digitizes and calibrates the analogue signals and transmits the information to the Cluster Processor and the Jet/Energy Processor. The Cluster Processor defines RoIs for electrons, photons and taus as 2×2 trigger tower clusters, where a trigger tower is built from the cells inside $\Delta\eta \times \Delta\phi = 0.1 \times 0.1$ of the ECAL. A RoI is formed if the summed transverse energy from at least one pair of nearest neighbor towers is larger than a programmable threshold. In addition, different isolation criteria can be used. The RoIs of jets are identified by the Jet/Energy Processor. The jet RoI are found by looking for a set of 4×4 or 8×8 trigger towers for which the sum of the transverse energy is higher than a given threshold and which surrounds a 2×2 trigger tower area that shows a local maximum of energy. The area of the 2×2 trigger tower in the center is the jet RoI. They are used to calculate global sums of scalar and missing transverse energy of the event.

The L1 muon trigger uses the fast trigger chambers (RPCs and TGCs) to look for

muon tracks forming coincidences between the different planes of the trigger chambers. The trajectory of a muon is compared to fixed templates of muon trajectories above a certain transverse momentum threshold.

The information of the L1Calo trigger and the L1 muon trigger are transmitted to the CTP which makes the trigger decision on L1. The initial bunch crossing rate of 40 MHz is reduced to 100 kHz by the L1 trigger [32]. In 2016, a new topological trigger (L1Topo) was added to the detector. L1Topo searches for geometric or kinematic associations between objects from the L1Calo trigger or the L1Muon trigger. Also the missing transverse energy is recalculated using more information. However, the data set used for this thesis was recorded in 2015, before L1Topo was installed.

The HLT processes the events that are accepted by the L1 trigger using finer-granularity calorimeter information as well as tracking information from the muon system and the inner detector. For this the HLT reconstruction can be performed either within the L1 RoIs or for the full detector. Most of the HLT triggers use a two-stage algorithm. The first stage reconstruction filters out most of the events in a small time window. The second stage takes more time for a more precise reconstruction for the events passing stage one. The final recording rate is reduced to 1 kHz by the HLT trigger [32].

2.4. Particle jets in ATLAS

Particle *jets* are the most frequently occurring collision products at the LHC and refer to a collimated cone of hadrons and other particles. This spray of particles is produced as a consequence of the production of quarks or gluons at collider experiments and the confinement of Quantum Chromodynamics, discussed in section 1.1. The process by which the quarks and gluons produce jets at collider experiments is called *hadronization*. It can be explained qualitatively with the example of two quarks being produced in e.g. a $q\bar{q} \to Z \to q\bar{q}$ process in a proton-proton collision drifting apart from each other. The two quarks interact through the exchange of virtual gluons (figure 2.5 (a)). The gluons carry color charge and therefore attractive interactions exist between the exchanged gluons. These interaction squeeze the color field between the quarks into a tube. The energy that is stored in the field increases linearly with the distance of the quarks. The energy density was measured to be approximately 1 GeV/fm. At some point the energy stored in the field is sufficient to produce a new $q\bar{q}$ pair (figure 2.5 (b)), resulting in a breaking of the color field which can be thought of as energetically favorable for nature. This process of creating new $q\bar{q}$ pairs is repeated until all the quarks end up with a relatively low energy and therefore combine into colorless hadrons (figure 2.5 (c)). Some of these hadrons decay before reaching the detector producing also other particles like e.g. photons or leptons. Finally the two spreads of hadrons and other particles originating from the initial quark and antiquark are observed as two jets. On average 60 % of a jet's energy is built up by charged particles, mostly pions, 30 % by photons from neutral pion decays and 10 % by neutral hadrons like neutrons. It is not possible to resolve all particles in a jet because groups of particles hit the same calorimeter cells.

In general, the process of hadronization is poorly understood and no derivation from first-principles has been achieved. Similarly, no analytic proof of the underlying concept of color confinement exists, although progress is made using lattice QCD calculations. In modern particle physics, phenomenological models [33, 34] are used to create a description of hadronization which can describe the experimental data to some extend.

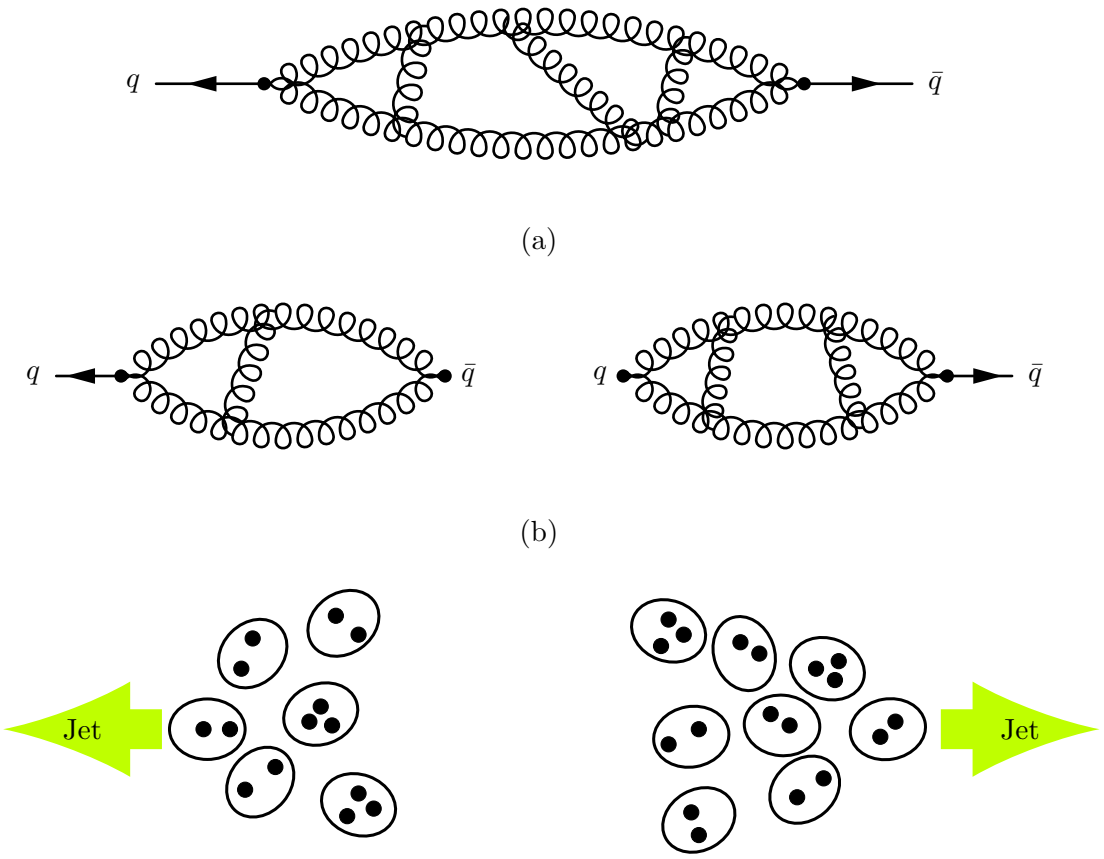

Figure 2.5.: Visualization of jet production originating from two intial quarks flying apart from each other. The interaction of the two quarks through the exchange of virtual gluons and the attractive interaction between these gluons which squeezes the color field is visualized in (a). At a certain distance the energy in the field is large enough to create a second $q\bar{q}$ pair from the vacuum (b). This process is repeated many times until color neutral hadrons are formed (c). These particles and their decay products are observed as a jet.

2.4.1. Jet reconstruction

The strict definition of a jet in collider experiments depends on the algorithm that is used to reconstruct the jet by forming topological clusters of calorimeter cells with energy depositions. The algorithm used throughout this thesis is the anti-k_t algorithm [35]. The input for this algorithm consists of a collection of topological clusters built from a seed calorimeter cell showing a significant energy deposition above a certain noise threshold and the neighboring cells. The *distance measure* d_{ij} between two objects i and j in the anti-k_t algorithm is defined as

$$d_{ij}(R) = \min\left(\frac{1}{p^2_{\mathrm{T},i}}, \frac{1}{p^2_{\mathrm{T},j}}\right)\frac{\Delta R^2_{ij}}{R^2}, \tag{2.11}$$

where $p_{\mathrm{T},i}$ ($p_{\mathrm{T},j}$) is the transverse momentum of the object i (j), ΔR_{ij} the angular distance as defined in equation (2.10) and R the radius input parameter of the algorithm, which is chosen to be $R = 0.4$ for the work of this thesis. In addition, the *exit condition* d_i for the sequential algorithm is defined as

$$d_i = \frac{1}{p^2_{\mathrm{T},i}}, \tag{2.12}$$

The algorithm works as follows. First, the distance measure d_{ij} is calculated for all possible combinations of objects i and j in the event as well as the exit condition d_i for all objects. Next, the smallest value of the distance measures and the exit conditions is identified. If the smallest value is a distance measure d_{ij} the objects i and j are combined by adding their four-vectors. If the smallest value is an exit condition d_i, the object i is identified as a jet and removed from the list of objects. This procedure is repeated until no objects are left.

Effectively, the anti-k_t algorithm starts by recombining the hard objects of the event with the spatial closest ones. This is a result of weighting the distance ΔR^2_{ij} with $1/p^2_T$. The distance measure will be smaller for pairs involving a hard object with a high momentum compared to the distance measure of two soft objects with a similar spatial distance. Therefore, the soft particles get mostly combined with a hard object before the soft particles merge among themselves. If there is no second hard object within $2R$ around the first hard object, this object will accumulate all soft particles within R. The result is a jet with the shape of a perfect cone. If there is a second hard object within a distance of $2R$ but not within R, two hard jets with more complex shapes will be formed. For the case of having two hard objects within a distance of smaller than R, the algorithm will return a single jet with a possibly more complex shape. The important feature of this algorithm is that these complex shapes are determined by the hard objects, namely by the amount of transverse momentum, and not by the soft particles. The robustness against the contributions from soft particles offers some advantages, although it cannot be judged a priori whether a jet algorithm with a resilience or a sensitivity of soft particles should be preferred. A robustness against soft particles can simplify certain theoretical calculations and minimize the decrease of the momentum resolution due to effects coming from the underlying event or additional hard interactions in the same bunch crossing.

2.4.2. Jet calibration

The response of the ATLAS calorimeter is different for electromagnetic energy depositions compared to hadronic energy deposition, referred to as a non-compensating calorimeter.

This results in the challenging task of calibrating the *jet energy scale*. This calibration is done as a relative calibration to the electromagnetic scale. Therefore, the calorimeter is calibrated by default at the electromagnetic scale, which would underestimate the energy of hadronic jets without further corrections. The response of the calorimeter at the electromagnetic scale depends on the energy and the η position of the jet. This section reviews the different steps of the jet energy scale calibration as performed in 2015 by ATLAS [36].

Origin Correction After reconstructing the jets from the topological clusters as explained above the jet direction is corrected so that its origin is compatible with the corresponding primary vertex. This correction is necessary because the topological clustering and the jet reconstruction algorithm use the center of the ATLAS detector as the origin for the four-momenta. The origin correction has no influence on the energy of the jet but improves the η resolution of jets.

Pile-up correction Next, a pile-up correction is performed accounting for additional energy contribution to the jet energy from additional proton-proton interaction in the same (in-time pile-up) as well as in previous and following bunch crossings (out-of-time pile-up). This correction aims at subtracting this additional energy and is carried out in two steps. First, an energy subtraction based on the area A of the jet is performed. This subtraction is based on the median energy density ρ in the $\eta \times \phi$ plane. Second, a residual correction is applied as a function of the number of primary vertices N_{PV} in the event, to cover in-time pile-up contributions, and the average number of proton-proton collisions per bunch crossings $< \mu >$, to cover out-of-time pile-up contributions. The dependence on these two variables is measured to be approximately linear. Therefore, the full pile-up correction on the transverse momentum of the jet can be formulated as

$$p_{\mathrm{T}}^{\mathrm{corr}} = p_{\mathrm{T}}^{EM} - \rho \times A - \alpha \times (N_{\mathrm{PV}} - 1) - \beta \times < \mu >, \tag{2.13}$$

where p_{T}^{EM} is the transverse momentum at the electromagnetic scale after the jet reconstruction is performed.

Jet energy scale and η calibration This calibration step corrects the reconstructed jet energy, after application of the origin and pile-up correction, to the jet energy at particle level and is therefore performed using MC simulations. Reconstructed jets are matched to particle level jets within $\Delta R < 0.3$. For the derivation of the calibration only isolated jets are used to avoid introducing a bias from the geometrical matching. The jet calibration factor for this correction is the inverse average energy response which is defined as the mean of a Gaussian fit to the center of the distribution showing the ratio of the reconstructed energy and the particle level energy of the jet. This correction factor is provided as a function of the energy and η. In addition, biases in the jet η reconstruction are also accounted for. A bias can arise from a jet reconstructed in a transition region between different calorimeter technologies or different calorimeter granularities. The two sides of the transition region show a different energy response, which increases the energy of one side of the jet compared to the other side.

Global sequential calibration The global sequential calibration refers to a series of corrections applied independently one after the other. These corrections take care of the dependence of the jet energy scale on longitudinal and transverse features of the jet, which are (largely) uncorrelated among each other. Such dependencies originate mainly

from the particle composition of a jet, varying between jets initiated from gluons or quarks, and differences in the detector interaction with different particles. The correction are constructed not to change the mean jet energy. In 2015, five corrections were used in the global sequential calibration accounting for the dependencies of the jet energy on the following, by MC simulation well modeled variables: the energy measured in the first layer of the tile calorimeter as well as the one measured in the third layer of the electromagnetic LAr calorimeter, the average momentum weighted transverse distance between the jet and all associated tracks, the number of tracks and the number of muon segments. This correction reduces e.g. flavor dependencies of the jet energy scale.

In-situ calibration In-situ calibration methods are applied only to data in order to account for differences in the jet response between data and MC simulations. These differences come from limitations in the detector material description, the modeling of hadronic and electromagnetic showers as well as the modeling of pile-up effects. The effect of this calibration step is that the jet energy scale in data and in MC simulation are set to *the same scale* by construction.

Several steps are involved in this calibration step. The *η-intercalibration* uses dijet events in order to correct the response of forward jets. The basic idea behind this approach is that the transverse momentum of both jets from a dijet event is expected to be the same. The central region of $|\eta| < 0.8$ is used as a well-understood reference region with a very homogeneous detector geometry. Therefore, for events with one central and one forward jet with $\eta > 0.8$, the well-measured reference jet in the central region can be balanced against the second jet in the forward region.

In addition to the η-intercalibration, three other in-situ calibrations correct the response of central jets with $\eta < 0.8$. Each of these methods focuses on different p_{T} regions using different reference objects recoiling against the jet. Z bosons and photons are used as reference objects for low and intermediate energy ranges. Photons are good reference objects because they are measured (mostly) with the electromagnetic calorimeter. The calibration of Z bosons rely on the leptonic decays into electron-positron or muon-anitmuon pairs, which are again measured with quite high precisions through the tracking and the electromagnetic calorimeter or the muon spectrometer. The Z-jet calibration is limited to $20 < p_{\mathrm{T}} < 506$ GeV due to the statistical limitation of the p_{T} range of the Z boson. Photons can be used in $36 < p_{\mathrm{T}} < 944$ GeV because of the low statistic at higher energies and dijet contamination. Additionally, a multijet balance is performed in order to extend the calibration to higher regions of p_{T}. Here, events with three or more jets are used where one high energetic jet is balanced against several lower energetic jets with energy accessible to the Z/γ-jet calibration.

For each in-situ calibration method the quantity $\mathcal{R}$ is calculated as the p_{T} ratio between a jet and its reference object. The ratio of this quantity in data and in MC simulation

$$c = \frac{\mathcal{R}^{\mathrm{data}}}{\mathcal{R}^{\mathrm{MC}}} \tag{2.14}$$

is used as the estimator of the ratio between the jet energy scale in data and MC simulation as a function of the transverse momentum of the jet and, for the η-intercalibration, also as a function of η. These calibration factors of each in-situ method are combined into a final in-situ calibration which covers the full kinematic region. The size of the overall correction is approximately 4 % at low energies and decreases to 2 % at a transverse momentum of 2 TeV.

Jet energy scale uncertainty The here presented jet calibration includes up to 80 different sources for uncertainties on the jet energy scale. Most of them originate from the in-situ calibration coming from mismodeling of physics effects in the MC simulation, the event selection for the calibration, sample statistics and the electron, muon and photon energy scales. Uncertainties associated to a potential mismodeling of certain physics effects are determined by performing the calibration method with two different MC generators and taking the difference between the two results as the uncertainty. The full uncertainty is provided as a function of p_{T} and η. For a central jet at $\eta = 0$ the uncertainty is approximately 6 % at low energies and decreases to 1 % at 200 GeV. From here up to an energy of 2 TeV the uncertainty stays approximately flat with a small increase due to the decrease in the statistical power related to the in-situ calibration methods. At 2 TeV the overall uncertainty increases again to higher values because the end of the range related to the multijet balance in-situ technique is reached.

2.4.3. Jet cleaning

Jets that are selected by an analysis are required to pass certain quality criteria which increases the probability that the jets come from the proton-proton collision and not from a non-collision origin, such as detector noise or cosmic rays. Two sets of quality criteria are defined, referred to as *loose* and *tight* selection critera [37]. The loose selection criteria result in a selection efficiency for jets from proton-proton collisions of 99.5 % or higher depending on the energy of the jet. The tight selection criteria introduce one additional criterion to the loose selection criteria and is mostly used for analyses being sensitive to non-collision backgrounds. The tight selection criteria result in an efficiency of 95 % or higher.

The loose selection consists of a set of criteria designed to reject jet signals from sporadic noise bursts in the HCAL, large coherent noise or isolated pathological cells in the ECAL, hardware issues, beam induced background and cosmic muon showers. Here, beam induced backgrounds arises from proton losses upstream of the interaction point. Especially hereby produced muons can reach the detector due to their long range in matter and deposit energy in the calorimeter of the detector, which can be interpreted as a jet. Signals from sporadic noise bursts in the HCAL are rejected using variables that describe the quality of the signal pulse shapes and the amount of cells with large negative energy deposits. Signals from noise in the ECAL are rejected by defining criteria on the energy fraction deposited in the ECAL and the energy fraction deposited in the LAr calorimeter cells of jets with poor signal shape quality as well as the average pulse shape quality. Three more general criteria make use of the jet energy fraction coming from charged particles using tracking information, the energy fraction deposited in the energy layer with the most energy deposit and the total energy fraction deposited in the ECAL. These criteria reject signals from hardware issues, beam induced background and cosmic rays.

The tight jet cleaning selection adds one more condition to the loose jet requirements in order to further suppress non-collision backgrounds. This criterion is based on the charged-particle fraction f_{ch} and the maximum fraction of the jet energy collected by a single calorimeter layer f_{max}: $f_{\mathrm{ch}}/f_{\mathrm{max}} > 0.1$, where f_{ch} is defined as the scalar sum of the transverse momenta of tracks which are matched to the primary vertex and lie within $\Delta R < 0.4$ around the jet axis, divided by the jet transverse momentum determined from the calorimeter information $f_{ch} = \sum p_{\mathrm{T}}^{\mathrm{track,\,jet}}/p_{\mathrm{T}}^{\mathrm{jet}}$. This criterion is based on the observation that fake jet candidates tend to have $f_{\mathrm{ch}} \approx 0$ and $f_{\mathrm{max}} \approx 1$, whereas jets from proton-proton collisions have typically $f_{\mathrm{ch}} > 0$ and $f_{\mathrm{max}} < 1$.

3. Unfolding

3.1. Motivation

High energy experiments like ATLAS at the LHC test the SM and search for new physics phenomena, for example gravitons. The usual approach to search for new physics is visualized in figure 3.1. First, one or a group of theoretical models describing physics beyond the SM to be tested is chosen. Then, the corresponding event signature predicted by this specific theoretical framework is identified. As discussed in section 1.3, such a theory could be the ADD model and the corresponding signature could describe a monojet-like event-topology, namely a large amount of missing transverse energy together with a high energetic jet. Afterwards, an event selection is optimized for the specific event-topology and the SM background is estimated. Finally, the event yield of the analysis is compared to the SM expectation in order to determine if events predicted by the theory in question might have been observed. If no excess above the SM prediction can be found, the results of the analysis can be used to set exclusion limits on parameters of the theory, for example on the fundamental Planck scale of the ADD model.

However, in order to set limits on a given theory it is necessary to know the efficiency at which events predicted by this theory pass the event criteria of the analysis. This requires an exact knowledge and understanding of the ATLAS detector, which is combined into a full simulation of the ATLAS detector. The simulation accounts for all imperfections of the detector, such as reconstruction efficiencies, limit acceptance and finite resolutions. This makes it possible to get a theoretical prediction in form of an event yield in a given phase space that can be compared to the event yield of an analysis and used to set limits on the theory. The crucial point is that this simulation of the ATLAS detector and the underlying efficiencies are not available outside the ATLAS collaboration.

Limitations of this approach Since the ATLAS simulation and the underlying efficiencies are not accessible outside the collaboration it becomes very difficult to set limits on other theories that are not included in the original analysis. Typically, in the original publication a few benchmark points of the chosen theory are transfered through the ATLAS simulation and compared to the event yield of the analysis. Limits are set commonly on simplified theories which might later be translated into much weaker limits for more realistic models. In this way, the results of a search analysis are used quite inefficiently since only a very limited amount of theoretical models can be tested. Likewise it is complicated to combine the results from ATLAS analyses with other analyses inside ATLAS or even other experiments, because the observed event yield depends on the detector. This marks a major drawback in the way results from LHC analyses are interpreted because the most powerful limits or signal significances are obtained from analyses that combine several measurements. For example, the discovery threshold of 5σ signal significance in the Higgs boson search could only be reached by ATLAS after combining several measurements analyzing different decay channels of the new fundamental particle.

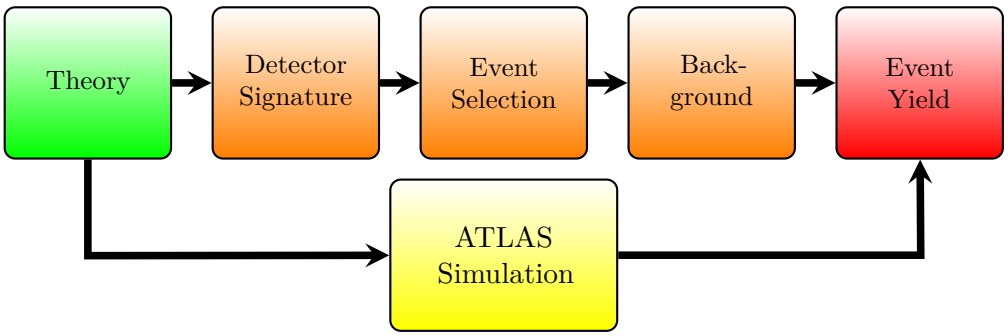

Figure 3.1.: Logic diagram of a typical ATLAS search analysis for physics beyond the Standard Model. First, a theory that should be tested is chosen and the corresponding event signature is identified. Afterwards, an event selection is defined and the backgrounds from SM processes are determined. The final event yield can be compared to the theoretical prediction after the use of the ATLAS simulation, which is not available outside the collaboration.

Unfolding The so called *unfolding* is a process designed to overcome the limitations mentioned above. Unfolding a distribution means correcting it for all detector effects and efficiencies as well as, if desired, for certain physics effects[1] using amongst the detector simulation. Therefore, the distribution at reconstruction level of an analysis can be turned into a *particle* or *parton level* distribution. In the example of the Monojet analysis, the unfolding accounts for example for bin migrations in the energy distribution of the leading jet caused by resolution effects.

The big advantage of unfolded distributions is that they are independent of the detector. Hence, they can be compared to *any* theories and not only to the ones considered in the original analysis.

Therefore, unfolded results can be used for a longer period of time testing future theories that are not formulated yet. In addition, it is much easier to combine unfolded results with other analysis and experiments. Publishing unfolded distributions leads to a more efficient and sustainable way of presenting the results of an analysis.

The strategy for an analysis of the ATLAS collaboration providing unfolded distribution is shown in figure 3.2. First, a signature that is sensetive to a variety of theoretical models is chosen. Then, a corresponding event selection is optimized for that signature and the SM background is determined. The event yield as a function of an observable is then unfolded using the ATLAS simulation. This unfolding procedure produces a well defined cross section in a well defined phase space, which can be easily calculated for a given theory or obtained from MC simulations. Therefore, the unfolded results can be used to test a variety of theories during the analysis or after publication.

[1] When measuring for example the mass peak of a Z boson in a Drell-Yan process at a hadron collider, the presence of e.g. final state radiation has an influence on the Z mass peak. This could also be corrected for in the unfolding.

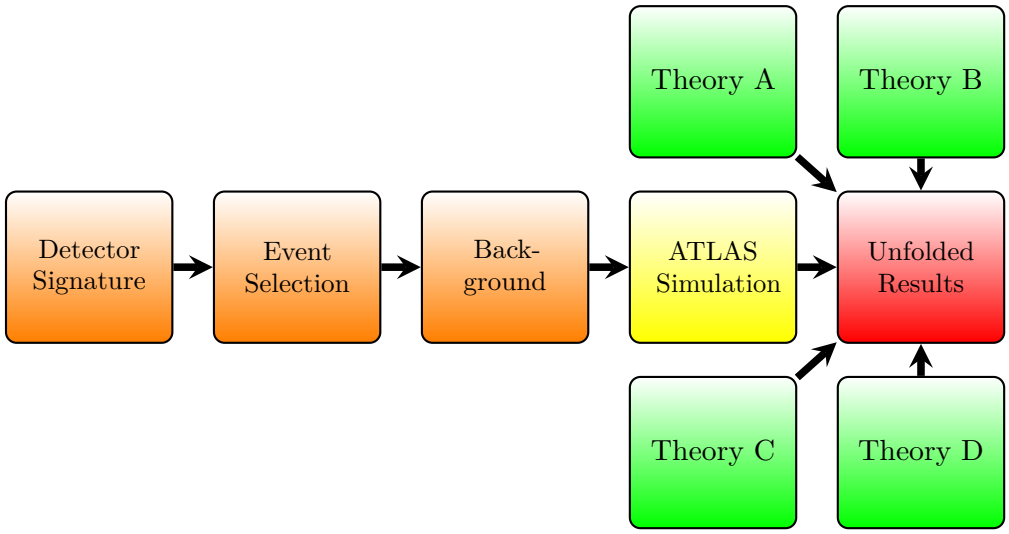

Figure 3.2.: Logic diagram of an ATLAS search analysis using unfolding. After chosing a signature for the analyis an event selection is optimized for this specific signature. The background is estimated and the event yield unfolded using the ATLAS simulation. The unfolded result can be compared to any theory.

3.2. Unfolding topologies

So far, when unfolding was used in ATLAS analyses, mostly a background subtraction from the observed data was performed before the unfolding. That means that one physical process was defined as the *signal*-process and all other processes that also pass the selection of the analysis were considered as *background* processes. The dominant backgrounds are typically estimated using (semi) data-driven methods while sub-dominant backgrounds can be estimated purely using MC simulations. The background is subtracted from the observed data and the resulting distribution is unfolded using an unfolding matrix obtained from a MC simulation of only the signal process, as visualized in figure 3.3. In other words, the distribution that is considered as the input to the unfolding is the difference of the observed data distribution and the background distributions

$$\text{Input}_{\text{Unfolding}} = \text{Data} - \sum_i \text{Background}_i \tag{3.1}$$

This thesis aims at exploring a different strategy of how to use unfolding in an ATLAS analysis. Instead of unfolding a single signal process, an inclusive event topology is unfolded. That means that

---

a selection based on a given event topology is performed, which can be passed by multiple processes, and the resulting distribution is unfolded *without* subtracting any background,

---

as visualized in figure 3.4. The input to the unfolding is the selected data without any subtraction

$$\text{Input}_{\text{Unfolding}} = \text{Data} \tag{3.2}$$

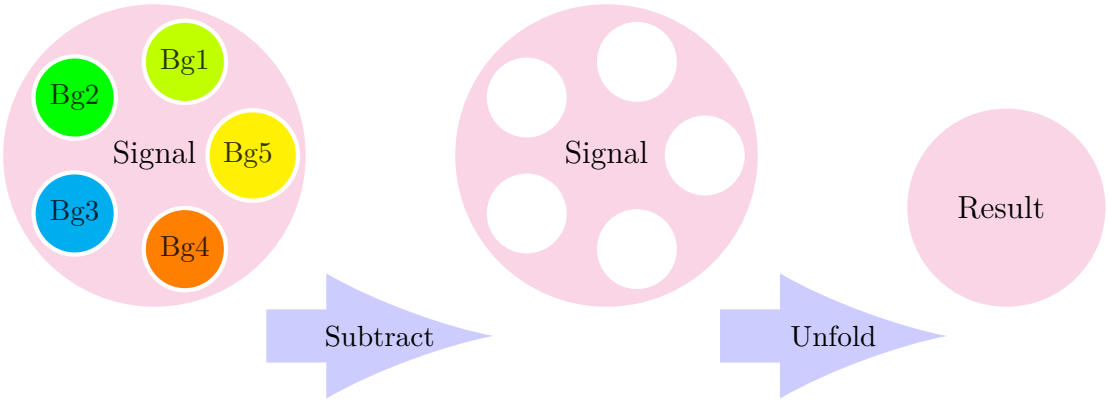

Figure 3.3.: Visualization of the conventional use of unfolding in an ATLAS analysis. The obtained data of events passing the event selection of the analysis incorporates contribution from different processes: one process is defined as the signal (pink), the other processes are considered as background (other colors). After the background determination, the background is subtracted from the signal process. Afterwards, the signal process is unfolded using the unfolding matrix built from this specific signal process.

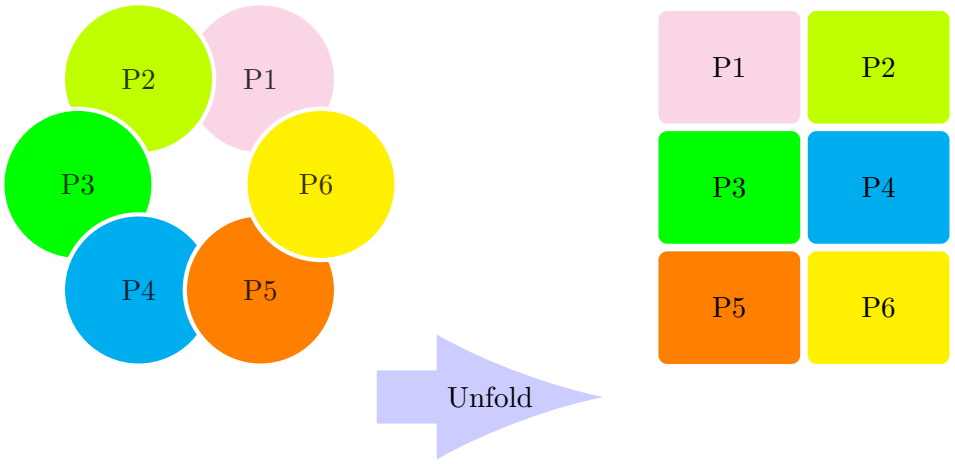

Figure 3.4.: Visualization of topology unfolding. Different processes (P1-P6) pass the event selection. No distinction into signal and background processes is made. The selected data is unfolded using a unfolding matrix which has contributions from each process that pass the selection. Therefore, also the unfolded result consists of contributions from different processes.

This strategy, referred to as *topology unfolding* or *unfolding a topology*, represents a more general method of unfolding, because here a cross section is defined that contains multiple processes and that can correspond to a quite complex event topology, which makes the unfolding more challenging. To explore the potential of the topology unfolding method, a monojet-like topology is tested in the following studies. The results of the newly introduced method is validated by comparing its results to a covnentional way of unfolding. A comparison between the uncertainties on the unfolding methods is presented. In addition, the limits at particle level are set on a parameter of the ADD model using topology unfolding and the conventional unfolding in order to compare the results.

From a conceptional point of view, the topology unfolding method could offer some advantages. Especially the omission of the background subtraction could give rise to a higher sensitivity of searches for new physics, because it is associated with experimental and often also theoretical uncertainties. The subtraction of the background in equation (3.1) is the Achilles' heel of the conventional search. The uncertainties on the background determination have a direct impact on the distribution which is used as input for the unfolding. This might lead to a larger effect of the uncertainties on the unfolded results compared to the topology unfolding method, because here the experimental uncertainties have only an indirect impact on the unfolded result by changing the relative fractions of the different contributions to the unfolding matrix. Furthermore, some uncertainties will be reduced by construction like the uncertainty coming from the limited statistic of the MC simulation used to construct the unfolding matrix, since in the conventional way this matrix is constructed from one single process, whereas for topology unfolding this matrix is the sum of many matrices from different processes. More details on this part of the conceptional difference can be found in section 4.7. In addition, using topology unfolding leads to a clearer separation of experimental and theoretical uncertainties, since the conventional way introduces theoretical uncertainties in many cases already in the measured distribution that serves as input to the unfolding. This comes from the fact that the background determination is done in most cases with *semi* data-driven techniques. These methods still rely on MC simulation and therefore do contain theoretical uncertainties. This can happen for example by introducing a scale factor obtained from MC simulation for transferring a background process from a control region into the signal region, which is a commonly used method for background determination. The theoretical uncertainties in the topology unfolding can again only influence the unfolding matrix. More important is however, that the theoretical uncertainties can be applied to the theoretical expectation to which the unfolded result is compared to in e.g. a limit setting procedure. This creates a more intuitive handling of theoretical uncertainties. This topic is further discussed in section 5.4.1.

3.3. Iterative unfolding using Bayes' theorem

This section describes an unfolding procedure using Bayes' theorem which arises quite naturally from the task that unfolding represents. Thinking of a MC simulation that generates events of a given process, transfers these events through a detector simulation and creates an output at reconstruction level, the problem of unfolding can be formulated in the following way.

Effectively, the simulation creates repeatedly an event in a bin T_j of the parton level distribution of a given observable, which ends up after considering physics effects, like e.g. final state radiation, and detector effects in a bin R_i of the reconstructed distribution. Therefore, the simulation emulates the conditional probability $P(R_i|T_j)$ of observing the

event in the bin R_i given that it was created in the bin T_j. Therefore, accepting that this problem is indeed of a truely probabilistic nature, the number of observed events $N(R_i)$ in the i-th bin can be described as

$$N(R_i) = \sum_j P(R_i|T_j) \cdot N(T_j), \tag{3.3}$$

where $N(T_j)$ represents the number of events that were created in the j-th bin. The process of unfolding aims to estimate the reverse way of this mapping. Given a reconstructed distribution, it tries to estimate how many events were created in each bin of the parton or particle level distribution, which is equivalent to estimate $P(T_j|R_i)$ from $P(R_i|T_j)$ given by the MC simulation

$$P(R_i|T_j) \qquad \longrightarrow \qquad P(T_j|R_i). \tag{3.4}$$

This formulation of the problem that unfolding represents leads directly to Bayes' theorem, which connects two specification of such conditional probabilities:

$$P(A|B) = \frac{P(B|A) \cdot P(A)}{P(B)}. \tag{3.5}$$

Applying Bayes' theorem to the unfolding task gives the following starting point for the conditional probability $P(T_i|R_j)$ in question:

$$\begin{aligned} P(T_i|R_j) &= \frac{P(R_j|T_i) \cdot P_0(T_i)}{P_0(R_j)} \\ &= \frac{P(R_j|T_i) \cdot P_0(T_i)}{\sum\limits_{l=1}^{N_T} P(R_j|T_l) \cdot P_0(T_l)}, \end{aligned} \tag{3.6}$$

where $P_0(T_i)$ and $P_0(R_j)$ describe *prior* probabilities for creating an event or observing an event in bin i or j respectively and N_T the number of bins of the parton or particle level distribution. Then, the number of events in the i-th bin of the parton or particle level distribution $n_{unf}(T_i)$ can be calculated from the number of observed events $n_{rec}(R_j)$ via

$$n_{unf}(T_i) = \sum_{j=1}^{N_R} P(T_i|R_j) \cdot n_{rec}(R_j). \tag{3.7}$$

This considerations takes only the migration of events from one bin to another due to detector or physics effect into account. In order to use Bayes' theorem in a real analysis, it has to be generalized in order to describe two more effects. The first effect arises from events that are created but not observed due to an inefficiency of e.g. the detector, referred to as *miss*-events. The second effect describes events that get reconstructed but have no valid correspondent at parton or particle level, referred in the following to as *fake*-events. Such an event could for example come from an object of the event that fails a kinematic criterion at parton or particle level but passes the criterion at reconstruction-level due to e.g. a smearing of the corresponding kinematic variable due to the finite resolution of the detector. Considering these two effects in addition, equation (3.6) and equation (3.7) turn into the final expression for the distribution at

parton or particle level estimated from the reconstructed distribution:

$$P(T_i|R_j) = \frac{P(R_j|T_i) \cdot P_0(T_i)}{\sum_{l=1}^{N_T+1} P(R_j|T_l) \cdot P_0(T_l)} \tag{3.8}$$

$$\begin{aligned} n_{unf}(T_i) &= \frac{1}{\epsilon_i} \sum_{j=1}^{N_R} P(T_i|R_j) \cdot n_{rec}(R_j) \\ &= \sum_{j=1}^{N_R} M_{ij} \cdot n(R_j), \end{aligned} \tag{3.9}$$

where M is the so-called *unfolding matrix*. The generalization of Bayes' theorem reveals itself in two parts. First, the inefficiencies are corrected for by multiplying an overall factor $1/\epsilon_i$, where ϵ_i describes an overall reconstruction efficiency for the bin i. Second, the fake-events are accounted for on the one hand in the normalization of $P(T_j|R_i)$ where an extra bin has been added and in the other hand in the normalization of the prior probability. The following list provides the definition of every single component of the unfolding formula.

- $P_0(T_i) = \frac{n_0(T_i)}{n_0(T_{tot})+n^{MC}(fakes_{tot})}$ is the prior probability of the i-th bin. It is calculated by dividing the number of events created in the i-th bin divided by the overall number of generated events plus the number of overall fake-events.
- $P(R_j|T_i) = \frac{N_{ij}}{n_0^{MC}(T_i)}$ is calculated by dividing the ij-th entry of the so-called *response* matrix N by the total number of generated events in the i-th bin. The entry N_{ij} quotes how many events that are generated in bin i get reconstructed in bin j.
- Since the last summand of the denominator in equation (3.8) takes the fake-events into account, the definition is here slightly changed to $P(R_j|T_i)_{fake} = \frac{n^{MC}(fakes_j)}{n^{MC}(fakes_{tot})} = \frac{n_{rec}(R_j) - \sum_{i=1}^{N_T} N_{ij}}{\sum_{l=1}^{N_R} \left(n_{rec}(R_l) - \sum_{i=1}^{N_T} N_{il} \right)}$ and $P_0(T_l)_{fake} = \frac{n^{MC}(fakes_{tot})}{n^{MC}(fakes_{tot})+n_0^{MC}(T_{tot})}$.
- $\epsilon_i = \sum_{k=1}^{N_R} P(R_k|T_i)$ is the efficiency of observing an event that was generated in the i-th bin of the parton- or particle-level distribution in any valid bin of the reconstruction-level distribution.

The physics effect that should be corrected for in the unfolding can be handled through the event or object selection on particle or parton level. Final state radiation can for example be accounted for in the unfolding by selecting the particles on parton level directly after the hard interaction before they can radiate off any other particles. [38]

Iterative unfolding procedure In a real analysis, the response matrix and the parton or particle level distributions is taken from MC simulations. Especially the use of a prior probability that has to be determined by the simulation of the same process that should be measured in the analysis seems to be a conceptional limitation of this approach. Therefore, an *iterative unfolding procedure* has been developed which aims at reducing

the influence of choosing the prior probability. In each step of this iterative procedure the parton or particle level distribution $n_0(T_i)$ used to calculate $P_0(T_i)$ is replaced by the unfolded result of the previous iteration $n_{unf}(T_i)$. So after the first step of the unfolding where as a particle or parton distribution a MC simulation was used, the replacement

$$P_0^{\text{1st step}}(T_i) = \frac{n_0^{MC}(T_i)}{n_0^{MC}(T_{tot}) + n^{MC}(fakes_{tot})} \tag{3.10}$$

$$\downarrow \tag{3.11}$$

$$P_0^{\text{1st iter.}}(T_i) = \frac{n_{unf}^{\text{1st step}}(T_i)}{n_{unf}^{\text{1st step}}(T_{tot}) + n^{MC}(fakes_{tot})} \tag{3.12}$$

takes place, where the fake distribution stays the same. In the second iteration $n_{unf}^{\text{1st step}}(T_i)$ is replaced by $n_{unf}^{\text{1st iter.}}(T_i)$ and so on. It can be shown for simulated data that the probability obtained from the unfolding P_0^{unf} lies between P_0^{MC} and the true probability.

In addition, the remaining bias resulting from the choice of the prior distribution can be estimated in a dedicated test and its result is considered as a systematic uncertainty. Typically, the resulting uncertainty is sub-dominant compared to other uncertainties introduced by the unfolding. Furthermore, studies were completed in the past performing unfolding with initial prior probabilities that showed a completely different shape than the underlying parton distribution showing that this procedure is still able to obtaining convincing results. More crucial for this unfolding method seems to be the response matrix and therefore the underlying detector simulation as well as the distribution at reconstruction level is unfolded.

Making use of this iterative procedure requires the formulation of a convergence criterion that determines how many iterations are performed. In principle, a smaller number of iterations should result in a larger bias from the choice of the initial prior probability, whereas a higher number of iterations increases the statistical uncertainties and their correlation between the bins. If too few iterations are performed a signal of new physics that might be present in the data distribution but not in the MC simulation used for the unfolding could potentially be lost since the unfolding procedure needs a few iterations to incorporate the signal into the prior probability. Two criteria are used in the following analysis to determine a suitable number of iteration. First, the unfolded distribution of the current iteration j is compared to the unfolded distribution of the previous iteration $j-1$ using the following definition

$$\chi^2_{red} = \frac{1}{N_{\text{bins}}} \sum_{i=1}^{N_{\text{bins}}} \frac{(n_{unf}^{j} - n_{unf}^{j-1})^2}{(\sigma_i^j)^2 + (\sigma_i^{j-1})^2}, \tag{3.13}$$

where σ_i^j is the uncertainty of the i-th bin of the unfolded distribution from the j-th iteration. If the two distributions are statistically consistent in terms of

$$\chi^2_{red} < 1, \tag{3.14}$$

no further iterations are performed. This criterion ensures that a signal present only in the data cannot be lost by performing too few iteration. Second, the dedicated uncertainty describing the bias from choosing the initial MC prior probability is required to be sufficiently small.

Uncertainty propagation The uncertainties of the measured distribution $n_{rec}(R_j)$ are propagated through the unfolding by taking into account that also the unfolding matrix M_{ij} depends on this distribution after the first step of the unfolding because the MC prior distribution is replaced by the unfolded result after each iteration. Since the unfolding takes the migration of bins into account, it correlates the uncertainties between different bins. As explained later on, it is important to provide correlation matrices for the unfolded distributions. In addition, the uncertainties on the reconstructed distribution that should be unfolded might already be correlated between the different bins at reconstruction level.

The uncertainty $\sigma^2_{unf}(T_i)$ of the i-th bin of the unfolded distribution is calculated by

$$\sigma^2_{unf}(T_i) = \sum_{j=1}^{N_R} \left(\frac{\partial n_{unf}(T_i)}{\partial n_{rec}(R_j)} \right)^2 \sigma^2_{rec}(R_j) \tag{3.15}$$

$$+ \sum_{k=1}^{N_R} \sum_{l=1, l\neq k}^{N_R} \left(\frac{\partial n_{unf}(T_i)}{\partial n_{rec}(R_k)} \right) \left(\frac{\partial n_{unf}(T_i)}{\partial n_{rec}(R_l)} \right) \rho^{rec}_{kl} \sigma_{rec}(R_k) \sigma_{rec}(R_l), \tag{3.16}$$

where $\rho^{rec}_{kl} = \frac{\mathrm{cov}^{rec}(k,l)}{\sigma_{rec}(R_k)\sigma_{rec}(R_l)}$ is the correlation coefficient, giving the correlation between the two uncertainties $\sigma_{rec}(R_k)$ and $\sigma_{rec}(R_l)$ of the reconstructed distribution in bin k and bin l using the covariance $cov(k,l)$ of these two uncertainties. The correlation matrix ρ could be diagonal for uncorrelated uncertainties. This could correspond to the statistical uncertainties of the reconstructed distribution, which are in general not correlated between bins for a given distribution. However, ρ could also not be diagonal for an uncertainty that shows a correlation between bins, like an uncertainty coming from the jet energy scale.

For the first unfolding step, calculating $\partial n_{unf}(T_i)/\partial n_{rec}(R_j)$ is trivial, since the unfolding matrix does not depend on the reconstructed distribution. Therefore, the unfolded distribution is just a linear combination of the different bins of reconstructed distribution and it holds that

$$\left(\frac{\partial n_{unf}(T_i)}{\partial n_{rec}(R_j)} \right)^{\text{1st step}} = M_{ij}. \tag{3.17}$$

The covariance matrix of the unfolded distribution is then simply

$$\mathrm{cov}(i,j)^{unf}_{\text{1st step}} = \sum_k \sum_l M_{ik} \mathrm{cov}(k,l)^{rec} M_{jl} \tag{3.18}$$

or

$$\mathrm{cov}^{unf}_{\text{1st step}} = M \mathrm{cov}^{rec} M^T. \tag{3.19}$$

For the first iteration, this does not hold anymore, because now the unfolding matrix depends also on the reconstructed distribution. Therefore, the unfolded result is no longer just a linear combination of bins of the reconstructed distribution. The Jacobi

matrix becomes

$$J_{ij} = \frac{\partial n_{unf}(T_i)}{\partial n_{rec}(R_j)} \tag{3.20}$$

$$= M_{ij} + \frac{1}{\epsilon_i} \sum_{k=1}^{N_R} \frac{P(R_k|T_i)}{\sum_{l=1}^{N_T+1} P(R_k|T_l) \cdot n_0(T_l)} \frac{\partial n_0(T_i)}{\partial n_{rec}(R_j)} n_{rec}(R_k) \tag{3.21}$$

$$- \frac{1}{\epsilon_i} \sum_{k=1}^{N_R} \frac{P(R_k|T_i) \cdot n_0(T_i)}{\left(\sum_{m=1}^{N_T+1} P(R_k|T_m) \cdot n_0(T_m) \right)^2} \sum_{l=1}^{N_T+1} P(R_k|T_l) \frac{\partial n_0(T_l)}{\partial n_{rec}(R_j)} n_{rec}(R_k) \tag{3.22}$$

$$= M_{ij} + \sum_{k=1}^{N_R} M_{ik} n_{rec}(R_k) \left(\frac{1}{n_0(T_i)} \frac{\partial n_0(T_i)}{\partial n_{rec}(R_j)} - \sum_{l=1}^{N_T+1} \frac{\epsilon_l}{n_0(T_l)} \frac{\partial n_0(T_l)}{\partial n_{rec}(R_j)} M_{lk} \right), \tag{3.23}$$

where the second summand takes the dependency of M_{ij} on $n_{reco}(R_j)$ after the first iteration into account. The term $\partial n_0(T_i)/\partial n_{rec}(R_j)$ is the same element of the Jacobi matrix from the previous iteration until the first unfolding step is reached. Here, n_0 is the MC particle level distribution n_0^{MC} and is therefore independent of the reconstructed distribution

$$\frac{\partial n_0^{MC}(T_i)}{\partial n_{rec}(R_j)} = 0. \tag{3.24}$$

The elements of the Jacobi matrix are used for the uncertainty propagation but also for providing the covariance matrix of the unfolded distribution which is now

$$\mathrm{cov}(i,j)^{unf} = \sum_k \sum_l J_{ik} \mathrm{cov}(k,l)^{rec} J_{jl} \tag{3.25}$$

or

$$\mathrm{cov}^{unf} = J \mathrm{cov}^{rec} J^T. \tag{3.26}$$

From this result the correlation matrix

$$\rho_{ij}^{unf} = \frac{cov^{unf}(i,j)}{\sigma_i^{unf} \sigma_j^{unf}} \tag{3.27}$$

can be calculated. Some examples for such a correlation matrix are given later on when the unfolded results will be discussed and an explanation is given why it is important to calculate and publish these correlation matrices. [39]

4. Topology unfolding

This chapter presents the validation of the newly introduced method of topology unfolding. The object and event selection used for this analyis represents the selection of a typical monojet search and is defined in section 4.2. MC simulations of the two dominant Standard Model backgrounds, $Z \to \nu\nu$ and $W \to \tau\nu$ in association with jets, are used for this study. The two MC simulations are split event by event into *pseudo-data* and *MC background*. The splitting is done by assigning every second event to the pseudo-data and the rest of the events to the MC background sample independent of the fact if the event passes the selection criteria or not. This choice tries to avoid a bias in the splitting and is chosen because the events in the MC simulations are sorted by the transverse momentum of the gauge bosons. After studying the resolution (section 4.3), the distribution obtained by applying the selection are shown in section 4.4 in order to check if a bias was introduced by the splitting algorithm. Next, the relevant quantities for the unfolding are presented in section 4.5.1. After performing a closure test for the unfolding, the pseudo-data is unfolded as described in section 4.5.2 and section 4.5.3. Finally, the topology unfolding method is validated by comparing it to a conventional way of unfolding (section 4.6). In addition, the uncertainties on the unfolding and the influence of systematic uncertainties of the MC and data input on these two methods are compared in section 4.7.

4.1. The dominant Standard Model contribution

The dominant SM background contribution in monojet searches are given by the $Z \to \nu\nu$ and $W \to \tau\nu$ events in association with jets. Two Feynman diagrams for these processes are shown in figure 4.1. The Z boson is produced in association with a jet originating from an outgoing quark and decays into a neutrino and an antineutrino, which results into a significant amount of missing transverse energy. Alternatively, the jet can also occur from initial state radiation. The event topology of these events is the same as the expected signal event topology, which makes the $Z \to \nu\nu$ process in association with jets an irreducible background. The second dominant background is the production of a W boson decaying into a tau lepton and a tau antineutrino, also in combination with jets. Because the tau lepton has a short lifetime of about 290 femto seconds [40], it decays before reaching the detector predominantly into a tau neutrino and one or three charged and additional uncharged pions. The resulting detector signature is similar to an energetic QCD-jet. The missing transverse energy comes from the neutrinos of the W boson and the tau lepton decay.

4.2. Object and event selection

The object selection provides the definition of jets, electrons, muons, photons and missing energy as used in the analysis. A distinction into *baseline* and *good* objects is made for muons and jets. Baseline objects fulfill basic selection criteria and are used as input for an overlap removal routine, a lepton veto and the missing transverse energy calculation.

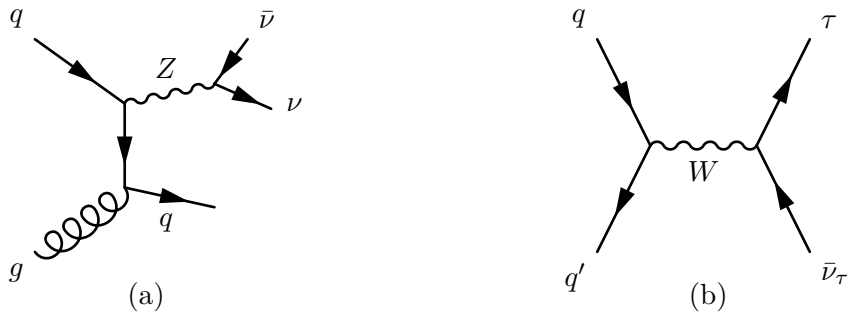

Figure 4.1.: Two examples for Feynman diagrams of the two dominant Standard Model processes for the monojet search. A Z boson is produced in association with a quark jet and decays into a neutrino and an antineutrino (a). A quark and an antiquark produce a W boson which decays into a tau lepton and a tau antineutrino (b).

Good muons and jets fulfill stricter criteria compared to the baseline selection and are used in the final event selection of the signal and control regions. In general, the here presented object and event selection follows very closely the selection of a recently published monojet search [41]. The same selection will also be used in chapter 5 in order to be able to compare results to the already published analysis.

4.2.1. Jet definition

Jets are reconstructed using the anti-k_t algorithm, discussed in section 2.4.1, with a radius parameter of 0.4. After calibration, jets are required to have a transverse momentum of $p_{\mathrm{T}} > 20\,\mathrm{GeV}$ and lie within $|\eta| < 2.8$. In addition, the jet candidates have to pass the loose jet cleaning criteria, as discussed in section 2.4.3.

For low energetic central jets with $|\eta| < 2.4$ and $20\,\mathrm{GeV} < p_{\mathrm{T}} < 50\,\mathrm{GeV}$ a jet-vertex fraction (JVT) value of > 0.64 is required in order to suppress jets coming from pileup collisions. The jet vertex fraction is defined as the sum of the transverse momentum of the tracks associated to the jet and the primary vertex divided by the sum of all tracks associated to the jet. Jet candidates that fulfill these criteria are considered as baseline jets and are used in the overlap removal routine and the missing energy calculation. If the jet candidate fulfills in addition the requirements imposed by the overlap removal routine, as discussed in section 4.2.5, and has a transverse momentum of $p_T > 30\,\mathrm{GeV}$, it is considered as a good jet.

4.2.2. Muon definition

Muons used in this analysis are reconstructed using the so-called *combined* (CB) and *stand-alone* (SA) type definitions. CB muons are formed by combining tracks of the muon spectrometer with tracks from the inner detector and form the class of muons with the best sample purity and momentum resolution. SA muons are reconstructed from trajectories that are built only from signals of the muon spectrometer. Both types of muons are reconstructed using the *Chain 3* algorithm as defined in [42]. In the identification step, a set of quality criteria is applied on these reconstructed muons, mainly to minimize the misidentification of hadrons as muons and ensure a robust momentum measurement. In this analysis the baseline and good muons are required to pass the *Medium* identification criteria defined in [43], which are designed to minimize the systematic uncertainties associated with the reconstruction and calibration of muons. These identification criteria

include requirements on the number and location of the signals corresponding to muon tracks in the MDT and CSC as well as selection criteria on the compatibility between the ID and MS momentum measurements. In addition, baseline muons are required to have a transverse momentum of $p_T > 10\,\text{GeV}$ and a pseudorapidity of $|\eta| < 2.5$. These muons are used for the overlap removal and the lepton veto in the signal region. Good muons are selected by requiring in addition the following criteria on the transversal and longitudinal impact parameters: $d_0/\sigma_{d0} < 3\,\text{mm}$, $|z_0 \sin\theta| < 0.5\,\text{mm}$, which aims at increasing the probability that the muon originates from the primary vertex.

4.2.3. Electron definition

Electrons are reconstructed from energy depositions in the ECAL that are matched to a track in the inner detector. The identification of electrons consists of criteria on different variables describing the longitudinal and transverse shape of the EM showers, the properties of the tracks from the inner detector and matching criteria between tracks and energy clusters in the calorimeter. These variables are combined to form a multivariate analysis. An electron likelihood is defined using uncorrelated signal and background probability density functions (PDF), which are obtained from data. An overall probability is calculated for each object to be signal and a second probability to be background. These two probabilities are used to define a single discriminant on which a selection criterion can be applied. This analysis uses the *loose* selection as defined in [44], whose selection of variables is focused on discriminating electrons against light-flavor jets. In addition, a transverse momentum criterion of $p_T > 20\,\text{GeV}$ and a pseudorapidity of $|\eta| < 2.47$ is required. These electrons are used for the overlap removal, the electron veto in the signal and control regions as well as for the calculation of the missing transverse energy.

4.2.4. Photon definition

Photons are reconstructed based on their energy depositions in the ECAL. Since the photon passes through matter when transversing the inner detector, it can convert into an electron-positron pair. Therefore, two different approaches exist when it comes to defining a track criterion in the photon reconstruction. If a cluster in the ECAL has no associated tracks from the inner detector, it is considered as an *unconverted photon* candidate. If a cluster is matched to a pair of oppositely-charged tracks, that are compatible with electrons in the transition radiation tracker or only to one track, it is considered as a *converted photon* candidate. To discriminate the photon candidates with one associated track from an electron that was produced at the interaction point, the track is required to have no hits in the innermost layer of the pixel detector. The photon identification aims at discriminating photons from hadrons and background photons from hadron decays. Hadrons release typically a significant fraction of energy in the HCAL and result in a broader shower. Photons from hadron decays are often pairs of two photons that are close to each other, e.g. from a decay of an uncharged pion. Therefore, the photon identification uses discriminating variables describing the energy fraction released in the HCAL and the shower shape. For this analysis the *tight* identification is used as defined in [45], which uses the full granularity of the ECAL and different requirements on the discriminant variables for converted and unconverted photons. In addition, the photons are required to have a transverse momentum of $p_T > 20\,\text{GeV}$. Photons fulfilling these criteria are used for the calculation of the missing transverse energy.

4.2.5. Overlap removal

After selecting the baseline objects as defined in the previous sections an overlap removal routine based on the angular and tracking information of the objects is performed in order to avoid associating one objects to more than one object class. A baseline jet is removed if an electron exists in the event that satisfies $\Delta R(jet, e) < 0.2$, or if the jet has less than three tracks and a baseline muon exists in the event with $\Delta R(jet, \mu) < 0.4$. An electron is removed if any baseline jet in the event lies within a range of $0.2 < \Delta R(j, e) < 0.4$ to the electron. A baseline muon is rejected from the event in case a jet with at least three tracks can be found satisfying $\Delta R(jet, \mu) < 0.4$.

4.2.6. Missing transverse energy definition

Conservation of momentum in the plane transverse to the beam axis implies that in an ideal case in which every particle can be detected and measured precisely, the transverse momentum of the decay products of each collision should sum up to zero. However, some particles do not interact with the detector and leave it therefore undetected. The SM provides only one type of particle of that kind, neutrinos. In addition to undetected particles, also detected particles with a mismeasured energy create an energy imbalance in the transverse plane. This imbalance is referred to as missing transverse energy. In this analysis the components of the missing transverse energy are calculated from the energy deposits associated to jets, electrons, photons or softer energy contributions not associated to any of these objects as

$$E_{x(y)}^{\text{miss}} = E_{x(y)}^{\text{miss},jet} + E_{x(y)}^{\text{miss},e} + E_{x(y)}^{\text{miss},\gamma} + E_{x(y)}^{\text{miss},soft}. \tag{4.1}$$

Each term represents the negative vectorial sum of the momenta of the corresponding objects defined in the previous sections. The soft term is based on tracks associated to the hard scattering vertex, which makes it more robust against pileup compared to a soft term based on calorimeter depositions. The term missing transverse energy usually refers to the magnitude of the vector

$$E_{\text{T}}^{miss} = \sqrt{(E_x^{\text{miss}})^2 + (E_y^{\text{miss}})^2} \tag{4.2}$$

Muons are treated as invisible particles throughout this analysis. [46]

4.2.7. Event selection on reconstruction level

The basis of the event selection of this analysis in the signal and control regions is a trigger logic selecting events with $E_{\text{T}}^{miss} > 70\,\text{GeV}$ (HLT_xe70). Each event is required to have a reconstructed primary vertex with at least two associated tracks each carrying a transverse momentum of $p_{\text{T}} > 0.4\,\text{GeV}$[1]. A standard event cleaning is performed ensuring all components of the detector were working normally. Events are rejected if they contain baseline jets failing the *loose* jet quality criteria [37] after the overlap removal. As discussed in section 2.4.3, applying this criterion rejects jet signals coming from noise in the ECAL or HCAL and reduces the influence of hardware issues, beam-induced backgrounds and cosmic muons. In addition to these basic selection criteria, the following event selection criteria are applied, summarized in table table 4.1.

[1] In the case where several vertices fulfill this criterion, the primary vertex is identified by selecting the one with the largest sum of p_{T}^2 of the associated track.

Event Selection		
All		
HLT_Xe70		
primary vertex		
loose jet cleaning		
$E_{\mathrm{T}}^{miss} > 250\,\mathrm{GeV}$		
1 to 4 good jets		
tight jet cleaning $j1$		
$p_{\mathrm{T}}^{j1} > 250\,\mathrm{GeV}$		
$\lvert\eta^{j1}\rvert < 2.4$		
$\Delta\phi(j, \vec{E}_{\mathrm{T}}^{miss}) > 0.4$		
SR	$Z \to \mu\mu$ CR	$W \to \tau\nu$ CR
veto baseline el.	veto baseline el.	veto baseline el.
veto baseline mu.	two good muons	one good muon
	veto other muons	veto other muons
	$66\,\mathrm{GeV} < m_{\mu\mu} < 116\,\mathrm{GeV}$	$30\,\mathrm{GeV} < m_{\mathrm{T}} < 100\,\mathrm{GeV}$

Table 4.1.: Criteria of the event selection on reconstruction level common to all regions (All), the signal region (SR) as well as the $Z \to \mu\mu$ and $W \to \tau\nu$ control region (CR).

The events are required to have a missing transverse energy larger than 250 GeV, to ensure that the used trigger is fully efficient as shown in [47]. The number of good jets in the event has to be between one and four, whereas the leading jet is required to have a transverse momentum of $p_{\mathrm{T}} > 250$ GeV and a pseudorapidity of $|\eta| < 2.4$. The transverse momentum criterion for the leading jet and the transverse energy criterion are symmetric, because in the signal process the leading quark or gluon jet recoils against the missing energy produced by a graviton. This is also the case for the diagram of the leading SM contribution ($Z \to \nu\nu$) as shown in figure 4.1 (a). The criterion of having a maximum of four good jets in the event is applied because the signal is not expected to have a large jet multiplicity while this criterion decreases contributions from some SM backgrounds like $t\bar{t}$ events. The *tight* jet cleaning criterion [37], as discussed in section 2.4.3, is applied to the leading jet in order to further suppress non-collision backgrounds. In addition, a requirement on the azimutal angle between any jet of the event and the direction of the missing transverse energy $\Delta\phi(j, \vec{E}_{\mathrm{T}}^{miss}) > 0.4$ is used to reduce the background from multijet events, where the energy of one of the jets is mismeasured. In case of an underestimation of the jet energy the direction of the missing transverse energy points into the direction of the mismeasured jet. In case of an overestimation of the energy, the missing energy tends to point into the opposite direction of this jet and since the dominant contribution to multijet events is the dijet production, this direction falls also in a direction of a jet. For the signal region events are rejected if they contain a baseline electron or muon. For the $Z \to \mu\mu$ control region exactly two good muons and no additional baseline muons or electrons are required, in addition to a criterion of the invariant mass of the two muons of 66 GeV $< m_{\mu\mu} <$ 116 GeV. For the $W \to \mu\nu$ control region exactly one good muon and no other baseline muons or electrons are required. Here, the transverse mass, defined as $m_{\mathrm{T}} = \sqrt{2p_{\mathrm{T}}^{\mu}p_{\mathrm{T}}^{\nu}[1 - \cos(\phi^{\mu} - \phi^{\nu})]}$ with

p_{T}^{μ} being the transverse momentum of the muon and p_{T}^{ν} being the missing transverse energy and with ϕ^{μ} and ϕ^{ν} being the corresponding azimuthal angles, is required to be 30 GeV $< m_{\mathrm{T}} <$ 100 GeV.

4.2.8. Object and event selection at particle level

This analysis unfolds the reconstructed distributions to particle level. Therefore, a selection at particle level has to be defined. This selection follows closely the one on reconstruction level in order to avoid an extrapolation into kinematic regions that are not considered at reconstruction level, which is usually connected with additional uncertainties. Jets at particle level are reconstructed through the anti-k_t algorithm with a radius parameter of 0.4. The kinematic criteria on p_{T} and $|\eta|$ are the same as on reconstruction level for jets, muons and electrons. At particle level, a baseline jet is removed if a muon or an electron exists in the event within $\Delta R < 0.4$ of the jet. The event selection at particle level consists of a subset of the criteria used for the event selection on reconstruction level. The same criteria are used for the missing transverse energy, the number of jets, the leading jet p_{T} and $|\eta|$ requirement, the number of baseline and good electrons and muons, the $\Delta\phi$ criterion between the missing transverse energy and the jets of the event as well as for the $m_{\mu\mu}$ and the m_{T} criterion for the two control regions.

4.3. Resolution

The main purpose of studying the resolution is to find adequate bin sizes for the different distributions that is robust against the finite resolution of the detector. Therefore, the detector resolution for variables that are used later on is determined in this chapter. These variables are the missing transverse energy of the event, the transverse momentum of the leading and second leading jet as well as the invariant mass of the two leading jets, which is defined as

$$m_{jj} = \sqrt{(E_{j1} + E_{j2})^2 - |\vec{p}_{j1} + \vec{p}_{j2}|^2}. \tag{4.3}$$

To obtain the resolution, the value of a given variable on particle level is compared to its value on reconstruction level in the following way.

First, a matching of jet objects between particle level and reconstruction level is performed. A jet is declared as matched between these two levels if $\Delta R(\mathrm{jet}_{\mathrm{part.}}, \mathrm{jet}_{\mathrm{reco.}}) <$ 0.1. This matching of jet objects is performed for all variables except the missing transverse energy which is a global variable of the event. Next, the distribution of e.g. the missing transverse energy on reconstruction level is divided by the distribution on particle level. This division is performed bin by bin in different ranges of the corresponding variable. To illustrate this procedure, the resulting distribution of the ratio is shown in figure 4.2 for the missing transverse energy in the region $1050 < E_{\mathrm{T}}^{\mathrm{miss}} < 1250\,\mathrm{GeV}$. The distribution shows a large population around a ratio of one and sharp falling tails to higher and lower values of the ratio. Then, a Gaussian function is fitted to the central part of the ratio distribution. The resolution is defined as the width of resulting fitted function. Therefore, the resolution of the missing transvers energy in the range $1050\,\mathrm{GeV} < E_{\mathrm{T}}^{\mathrm{miss}} < 1250\,\mathrm{GeV}$ corresponds to the width of the Gaussian function indicated by the purple, dashed line in figure 4.2. The fit is only performed at the center of the distribution around its mean because the outer parts of the distribution show a non Gaussian behavior. However, the tails are not expected to have any influence on the analysis, such that they can safely be

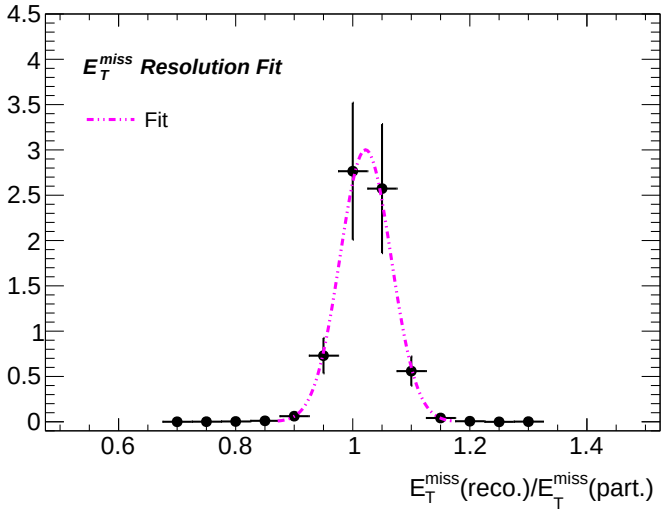

Figure 4.2.: Example for the ratio distribution of the reconstructed and generated missing transverse energy in the range $1050\,\text{GeV} < E_\text{T}^\text{miss} < 1250\,\text{GeV}$ of the $Z \to \nu\nu$ simulation. The purple line shows the result of fitting a Gaussian function to the central part of the distribution around its mean.

neglected. This procedure is performed for the whole range of the missing transverse energy and also the other variables mentioned at the beginning of this section.

The resolution of the missing transverse energy and the leading jet transverse momentum are shown in figure 4.3. Here, the results obtained from using different sizes for the ranges in which the resolution is determined are shown. For all variables the results from using different sizes for the regions are consistent. The resolution of the missing energy and the leading jet transverse momentum are almost constant throughout the whole energy range with a slow decrease twoards higher energies. The resolution for both variables is located around 3 % to 5 %. The resolution of the invariant mass of the two leading jets and the transverse momentum of the second leading jet are shown in appendix A.1 and have a slightly more distinct decrease towards higher energies. In these distribution the fit quality at lower energy is not as good as it is at higher energies. Since the most interesting part of the distribution for a search is in general the high energy regime, a conservative estimate of 10 % can be made for the low energy region ($< 400\,\text{GeV}$) for these two distributions. This does not effect the choice of the binning for these variables defined at the end of this section. The resolution at the higher energies is around 5 %. As expected, no significant difference can be observed between the resolution of the two simulated processes in all four variables. Based on these results, the bin size for the four distributions is chosen to be 50 GeV up to energies of 1 TeV and 100 GeV for higher energies. This choice ensures that the bin size at a given energy is always larger than the corresponding resolution.

4.4. Results at reconstruction and particle level

This section presents the several distributions on reconstruction and particle level obtained with the object and event selection described in section 4.2. Different kinematic distributions are evaluated with respect to the agreement between pseudo-data and MC background in the signal region, both consisting of simulated $Z \to \nu\nu$ and $W \to \tau\nu$

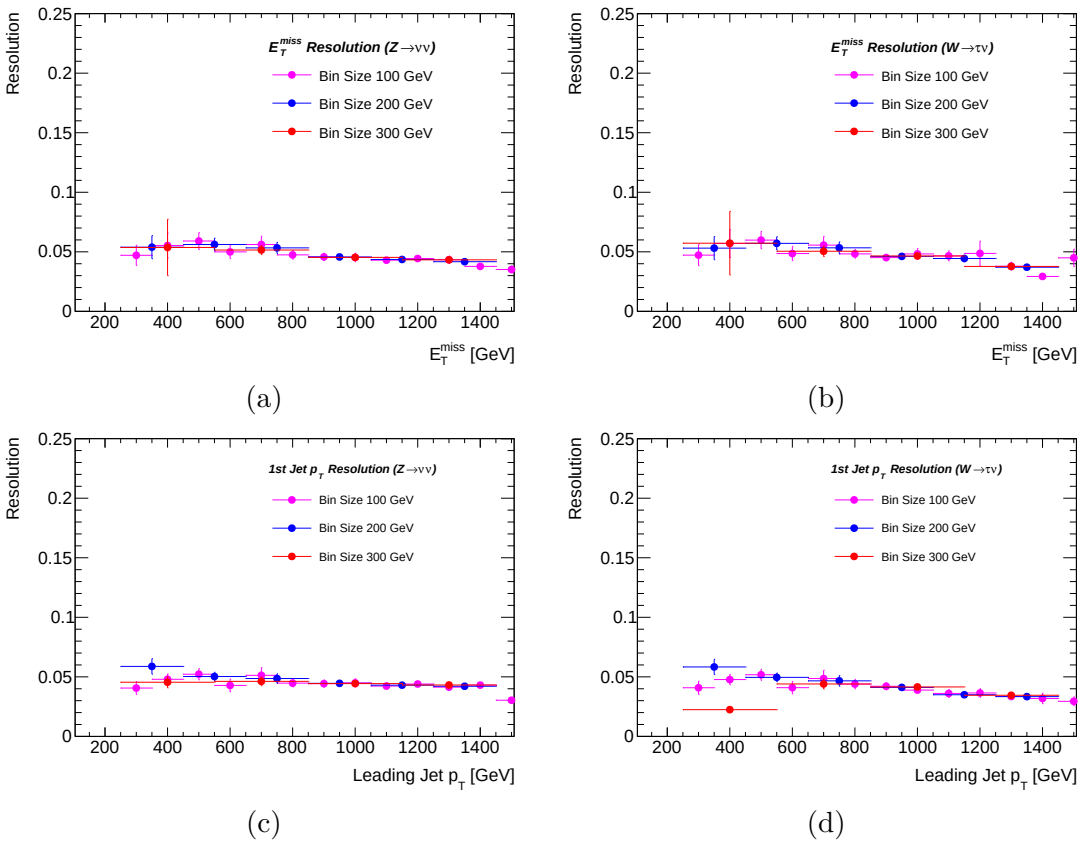

Figure 4.3.: The resolution of the missing transverse energy and transverse momentum of the leading for the $Z \to \nu\nu$ (a,c,e,g) and $W \to \tau\nu$ (b,d,f,h) simulation.

events. To simplify the comparison of the event yield with the analysis performed in chapter 5, all distributions are normalized to an integrated luminosity of $3.2\,\mathrm{fb}^{-1}$. The contribution to the event yield in the signal region of the $Z \to \nu\nu$ process is roughly three times higher than the contribution of the $W \to \tau\nu$ process. Figure 4.4 shows the distributions of the missing transverse energy, the transverse momentum of the leading jet, the pseudorapidity of the leading jet, the number of jets, the transverse momentum of the second leading jet and the invariant mass of the two leading jets on reconstruction level. The ratio of pseudo-data and the sum of the two MC backgrounds is shown in the lower part of each distribution. Here, the uncertainties include only the statistical uncertainty of the pseudo-data and the MC background. In the vast majority of the bins of each distribution the ratio is compatible with one, which shows that the splitting of the MC simulations into MC background and pseudo-data did not introduce a bias. A similarly good agreement between pseudo-data and MC background can also be observed in the particle level distributions, shown in figure 4.5. This high level of agreement between the pseudo-data and the MC background in the distributions on reconstruction and particle level validates the splitting algorithm and is important for further studies.

4.5. Unfolding

The following section consists of validation studies concerning the input of the unfolding. First, the reconstruction efficiencies, fake rates, purities and response matrices are presented. Afterwards, a closure test validates the unfolding procedure, followed by an explanation of the uncertainties that are considered in the upcoming analysis. First results for the uncertainties on each unfolding step are presented as well.

4.5.1. Efficiency, fake rate, purity and response matrix

The reconstruction efficiency, the fake rate, the purity as well as the response matrix represent import quantities for the unfolding. As explained in section 3.3 the reconstruction efficiency ϵ_i is used to correct for events that are not reconstructed due to any kind of imperfection of the detector. Its definition given in section 3.3 is equivalent to

$$\epsilon_i = \sum_{k=1}^{N_R} \frac{N_{ik}}{n_0^{MC}(T_i)}, \tag{4.4}$$

where N_{ik} is the ik-th entry of the response matrix and $n_0^{MC}(T_i)$ the i-th bin entry of MC distribution on particle level. In other words, the efficiency for a particle level bin i is computed by dividing the number of events that pass the selection criteria on particle level in this bin and the requirements on reconstruction level in any bin by the overall number of events that pass the particle level criteria in the i-th bin. The reconstruction efficiency for the missing transverse energy, the transverse momentum of the leading and second leading jet and the invariant mass of the two leading jets are shown in figure 4.6. In general, the efficiency is quite high and apart from one bin approximately constant for all distributions. It lies roughly between 80% to 95% for $Z \to \nu\nu$ and between 70% to 85% for $W \to \tau\nu$ events depending on the distribution. The difference between the two processes could arise from the different nature of the (leading) jet coming from a quark or gluon for $Z \to \nu\nu$ events and from a τ lepton for $W \to \tau\nu$ events and the corresponding jet reconstruction efficiencies. The efficiency for the sum of the processes is located quite close to the dominant $Z \to \nu\nu$ process, which can be seen in the lower plots showing the

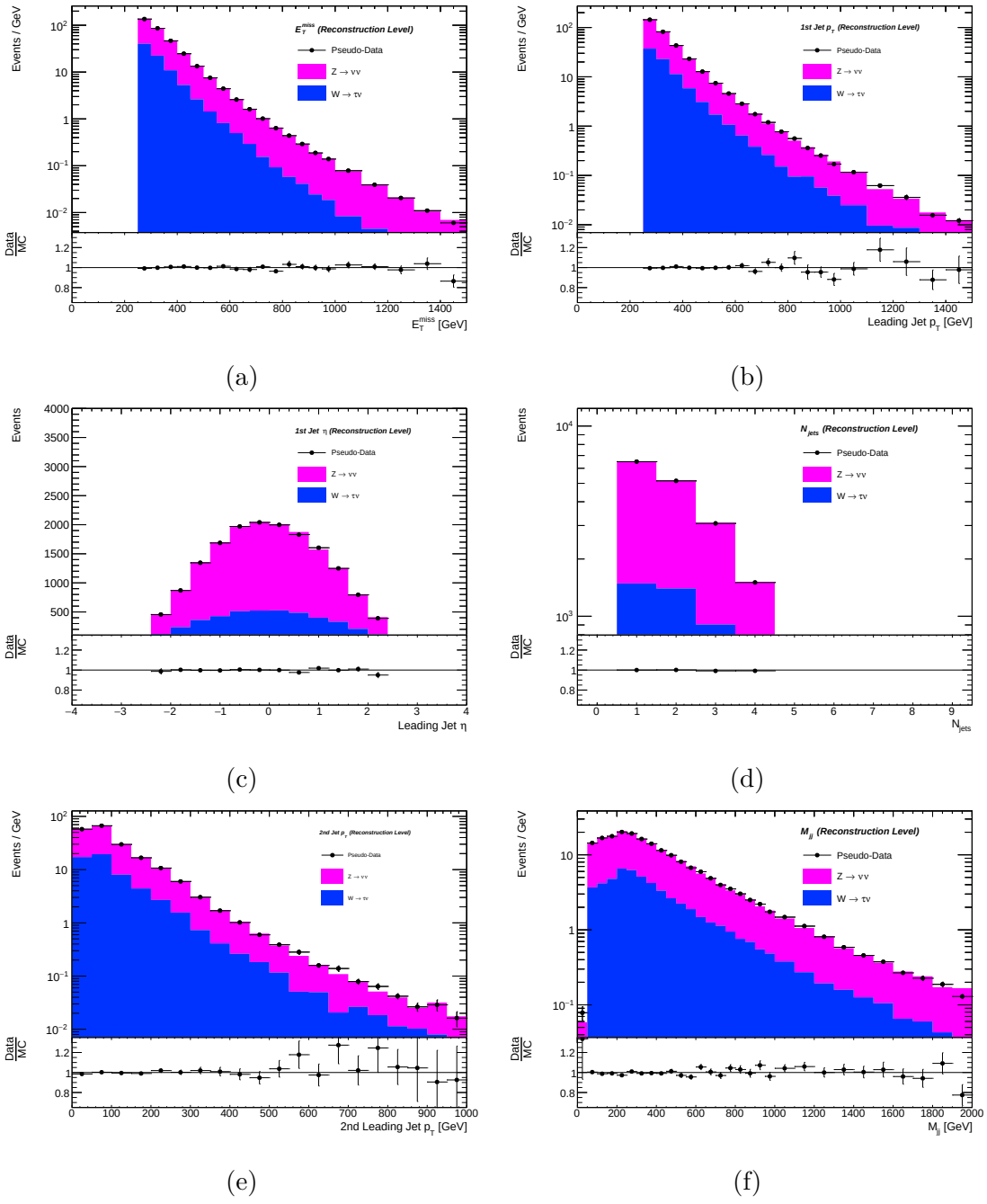

Figure 4.4.: The results on reconstruction level obtained from splitting the MC simulations for the processes $Z \to \nu\nu$ and $W \to \tau\nu$ into MC background (blue, pink) and pseudo-data (black). Shown are the distributions of the missing transverse energy (a), the transverse momentum of the leading jet (b), the pseudorapidity of the leading jet (c), the number of jets (d), the transverse momentum of the second leading jet (e) and the invariant mass of the two leading jets (f). The lower plot of each distribution shows the ratio of the pseudo-data and the sum of the two MC backgrounds.

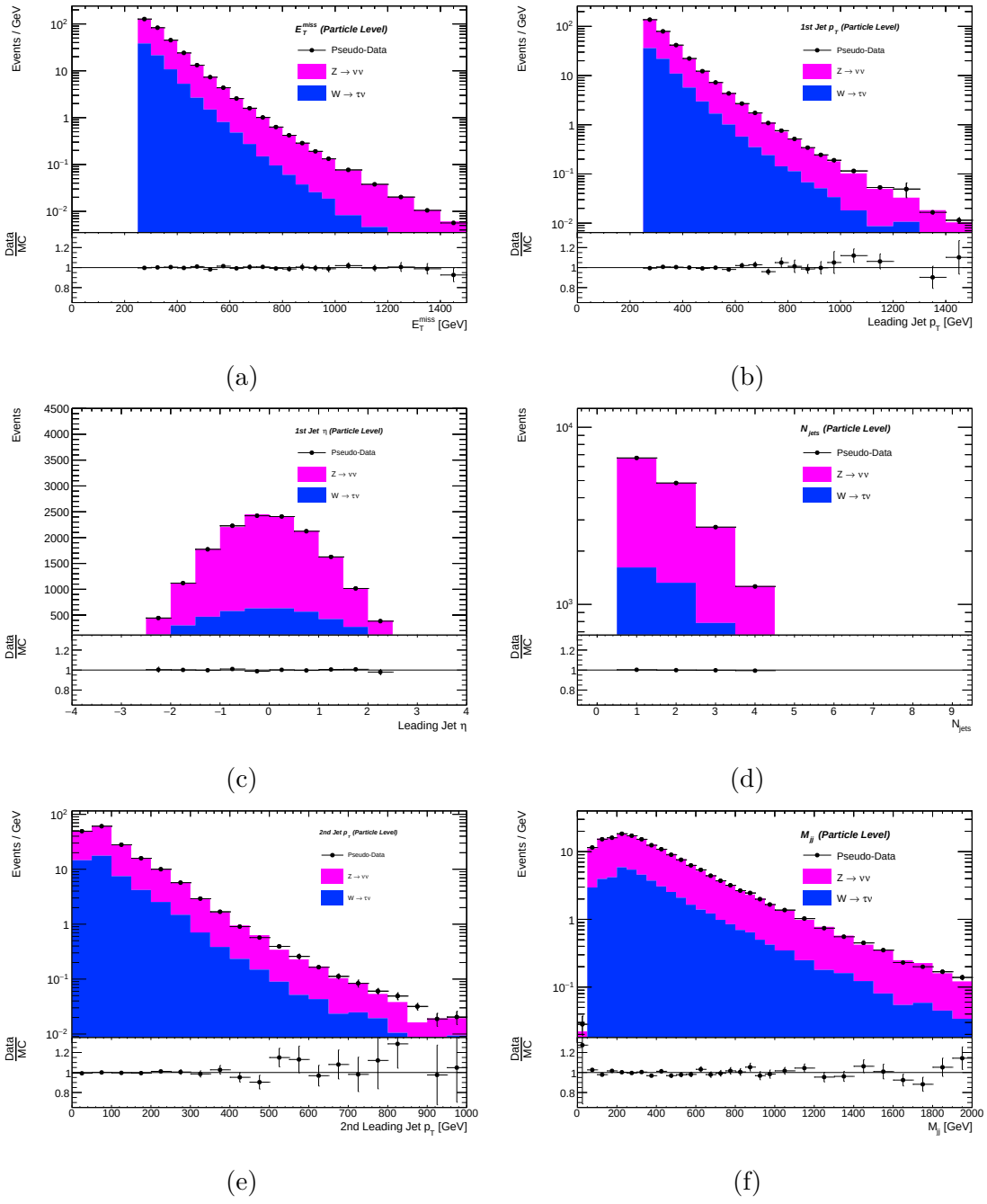

Figure 4.5.: The results on particle level obtained from splitting the MC simulations for the processes $Z \to \nu\nu$ and $W \to \tau\nu$ into MC background (blue, pink) and pseudo-data (black). Shown are the distributions of the missing transverse energy (a), the transverse momentum of the leading jet (b), the pseudorapidity of the leading jet (c), the number of jets (d), the transverse momentum of the second leading jet (e) and the invariant mass of the two leading jets (f). The lower plot of each distribution shows the ratio of the pseudo-data and the sum of the two MC backgrounds.

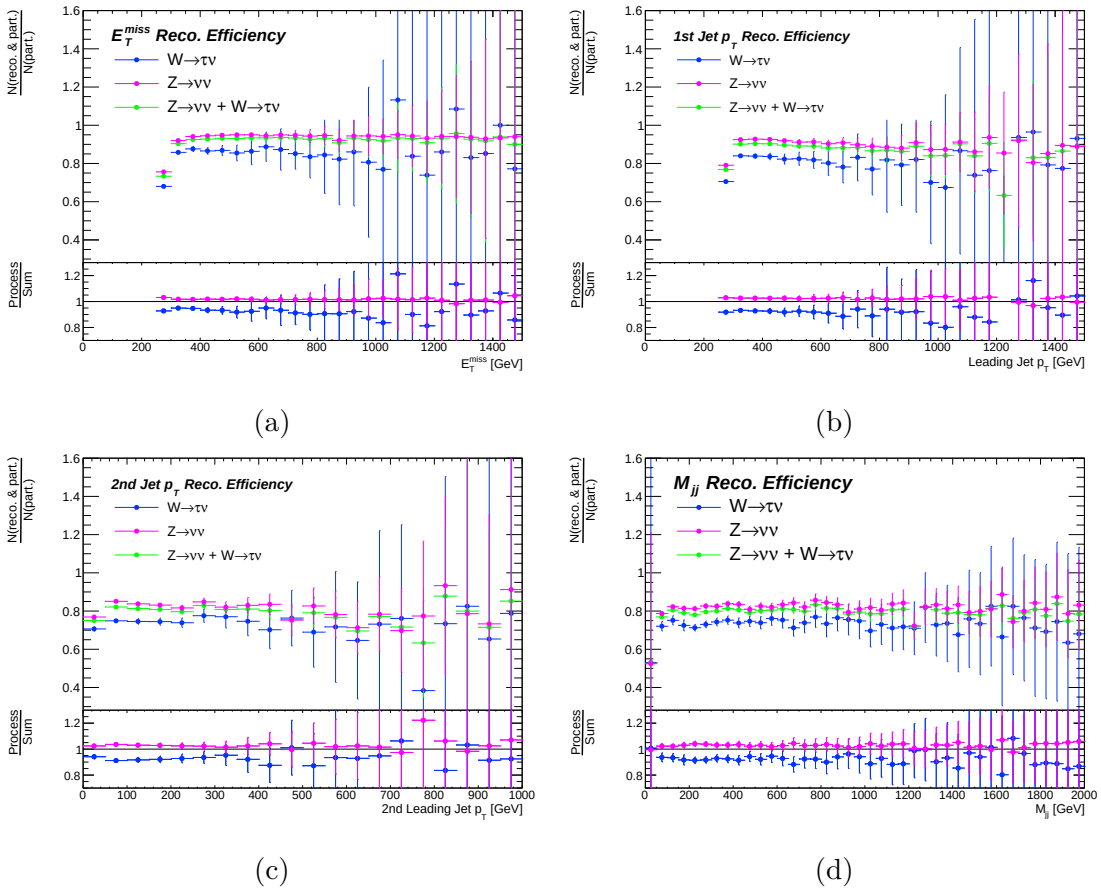

Figure 4.6.: The reconstruction efficiencies for the missing transverse energy (a), the transverse momentum of the leading (b) and second leading jet (c) and the invariant mass of the two leading jets (d) for the $Z \to \nu\nu$ (pink) and $W \to \tau\nu$ (blue) process as well as for the sum of these two processes (green). The lower plots show the ratio distributions of the efficiency of one process and the efficiency for both processes.

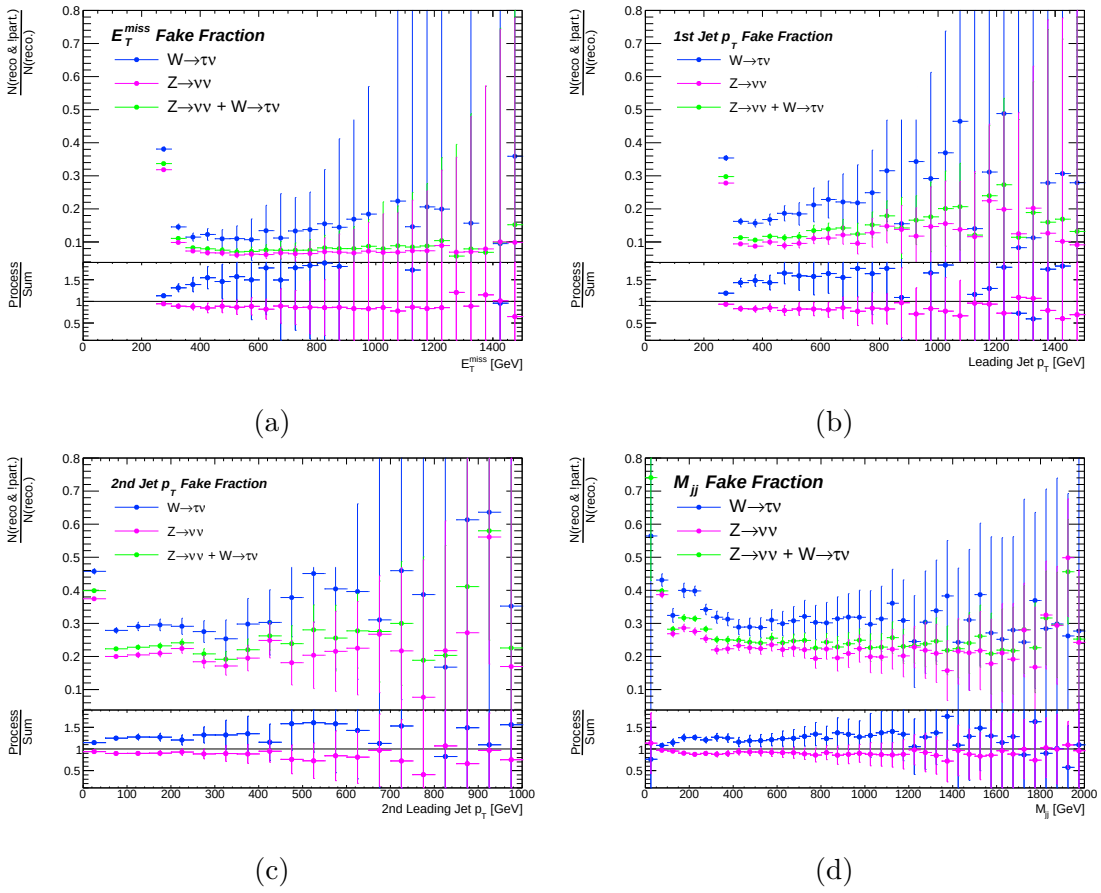

Figure 4.7.: The fake rates for the missing transverse energy (a), the transverse momentum of the leading (b) and second leading jet (c) and the invariant mass of the two leading jets (d) for the $Z \to \nu\nu$ (pink) and $W \to \tau\nu$ (blue) process as well as for the sum of these two processes (green).

efficiency of one process divided by the efficiency for both processes. For some values of the transverse missing energy above 1 TeV the reconstruction efficiency is larger than one for the $W \to \tau\nu$ process. The reason for this can be found in the weights of the MC simulation, which can be positive or negative. That is the reason why the sum of weights of a subset can be larger than the sum of the total set. However, this only occurs in low statistics regions with very few events. Therefore, the influence of these weights is small.

The fake rate of bin i is defined as the ratio of events that pass the selection criteria on reconstruction level in this bin but *not* on particle level in any bin and the overall number of events that pass the reconstruction requirements in this bin:

$$f_i = \frac{n^{MC}(R_i) - \sum_{k=1}^{N_T} N_{ki}}{n^{MC}(R_i)}. \tag{4.5}$$

The fake rate is a measure for the fake-events discussed in section 3.3. Figure 4.7 presents the fake rates as a function of the same variables as for the reconstruction efficiencies. For the missing transverse energy and the leading jet transverse momentum a larger fake rate in the first bin is observed coming from events with a missing transverse energy or a leading jet transverse momentum on particle level just smaller than the

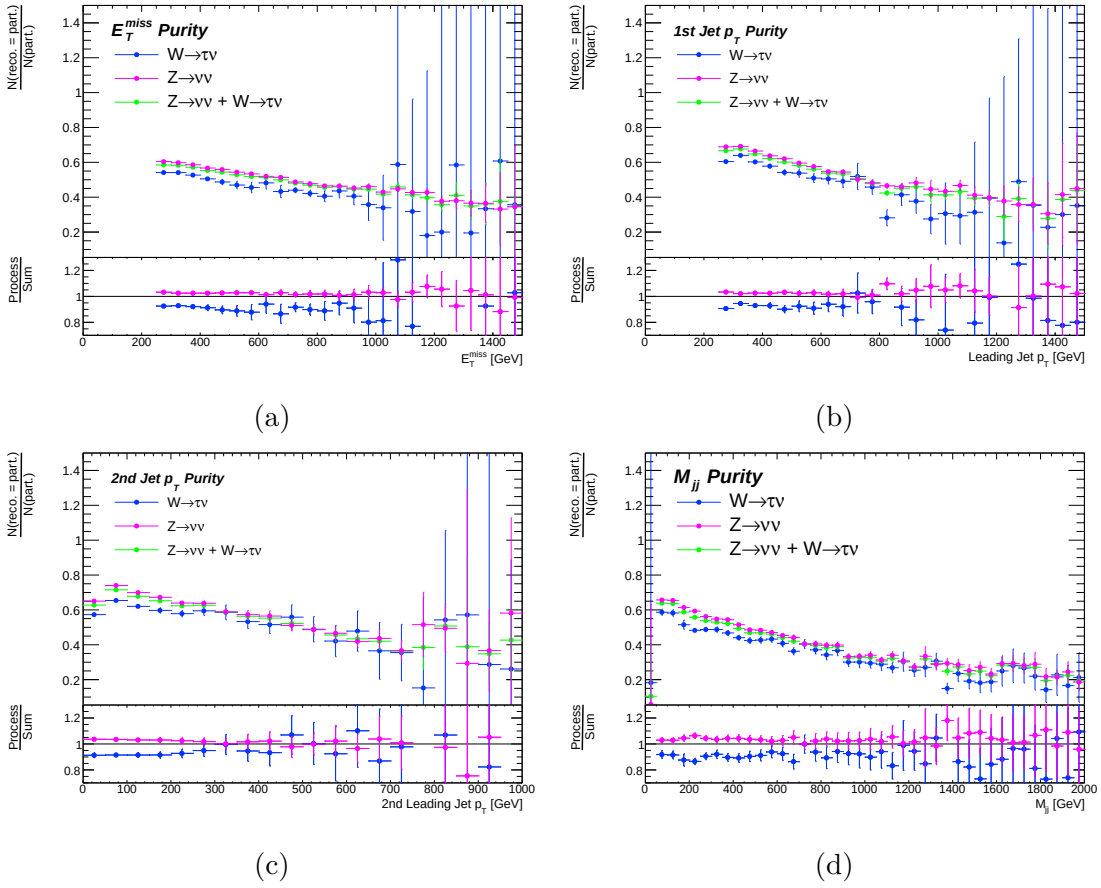

Figure 4.8.: The purity for the missing transverse energy (a), the transverse momentum of the leading (b) and second leading jet (c) and the invariant mass of the two leading jets (d) for the $Z \to \nu\nu$ (pink) and $W \to \tau\nu$ (blue) process as well as for the sum of these two processes (green).

corresponding selection criterion. Therefore, they do not pass the particle level selection. The reconstructed values for the $E_{\mathrm{T}}^{\mathrm{miss}}$ or the leading jet p_{T} migrate just above the selection criterion and end up in the first bin of the corresponding distribution. A smaller increase of the fake rate at low energies can also be observed for the second leading jet transverse momentum or the invariant mass distribution. The fake rates decrease towards higher energies for all distributions and stays approximately constant. The $Z \to \nu\nu$ process shows a smaller fake rate throughout all distributions.

The purity of bin i is defined as the number of events that pass the selection criteria at particle and at reconstruction level in the same bin i divided by the overall number of events that pass the selection criteria in this bin on particle level:

$$p_i = \frac{N_{ii}}{n_0^{MC}(T_i)}. \tag{4.6}$$

It corresponds to the diagonal entries of the response matrix and is therefore a measure for the amount of bin to bin migration from particle to reconstruction level, where a higher purity means less migration. The purity distributions are shown in figure 4.8. For the studied variables the purity is between 60 % to 70 % at lower energies and shows a decreasing behavior towards higher energies for all distributions. Therefore, a higher relative amount of migration between bins takes place at higher energies. The

$Z \to \nu\nu$ process shows for nearly all phase space regions a higher purity and therefore less migration.

The high fraction of events reconstructed in the same bin on particle and reconstruction level can also be seen by directly looking at the response matrices, shown in figure 4.9 for the missing transverse energy and transverse momentum of the leading jet. The response matrix of the $Z \to \nu\nu$ process appears to have a wider spread of events off the diagonal. However, the values of these entries are far below one event and come from the higher statistics compared to the $W \to \tau\nu$ process. Therefore, the purity is a better way to judge the migration of events. Response matrices for other variables are shown in appendix A.2.

The event selection presented here results in a modest task for an unfolding procedure. High reconstruction efficiencies and low fake rates are the reason why the distributions on reconstruction and particle level (compare figure 4.4 and figure 4.5) show no big difference concerning their overall number of events. The relatively high purity ensures a modest amount of bin-to-bin migration. Therefore, the presented event selection offers a good opportunity to test the newly proposed unfolding strategy. Once the topology unfolding method is validated for such an relatively easy unfolding task, it can be tested in more complex scenarios with e.g. a much lower reconstruction efficiency. However, the first proof of concept studies are performed with an selection that results in a modest unfolding task to estimate the potential of the new method. By taking into account several distributions with different values but a similar behavior in e.g. the reconstruction efficiency, the robustness of the results from the unfolding studies can be tested in addition. That is the reason why also distributions like the invariant mass of the leading jets are considered in these studies, although it is not expected that these distributions are sensitive to new physics in a monojet search.

The presented event selection offers a good opportunity to explore the possibilities of the new method of topology unfolding. Different kinematic distributions are considered for robustness studies.

4.5.2. Closure test

The following study presents an established way of validating the implementation of the unfolding. The reconstructed distribution from the same MC simulation that is used for the unfolding input, namely the response matrix, the prior probabilities as well as the estimate of the fake- and miss-events, is unfolded. For the first unfolding step, the particle level information of the MC is used for the prior probability

$$P_0(T_i) = \frac{n_0^{MC}(T_i)}{n_0^{MC}(T_{tot}) + n^{MC}(fakes_{tot})}. \tag{4.7}$$

Therefore, using the definitions given in section 3.3 the conditional probability $P(T_i|R_j)$ reduces for the first unfolding step to

$$P^{\text{1st step}}(T_i|R_j) = \frac{N_{ij}}{\sum_{l=1}^{N_T+1} N_{lj}} = \frac{N_{ij}}{\sum_{l=1}^{N_T} (N_{lj} + n^{MC}(fakes_j))} \tag{4.8}$$

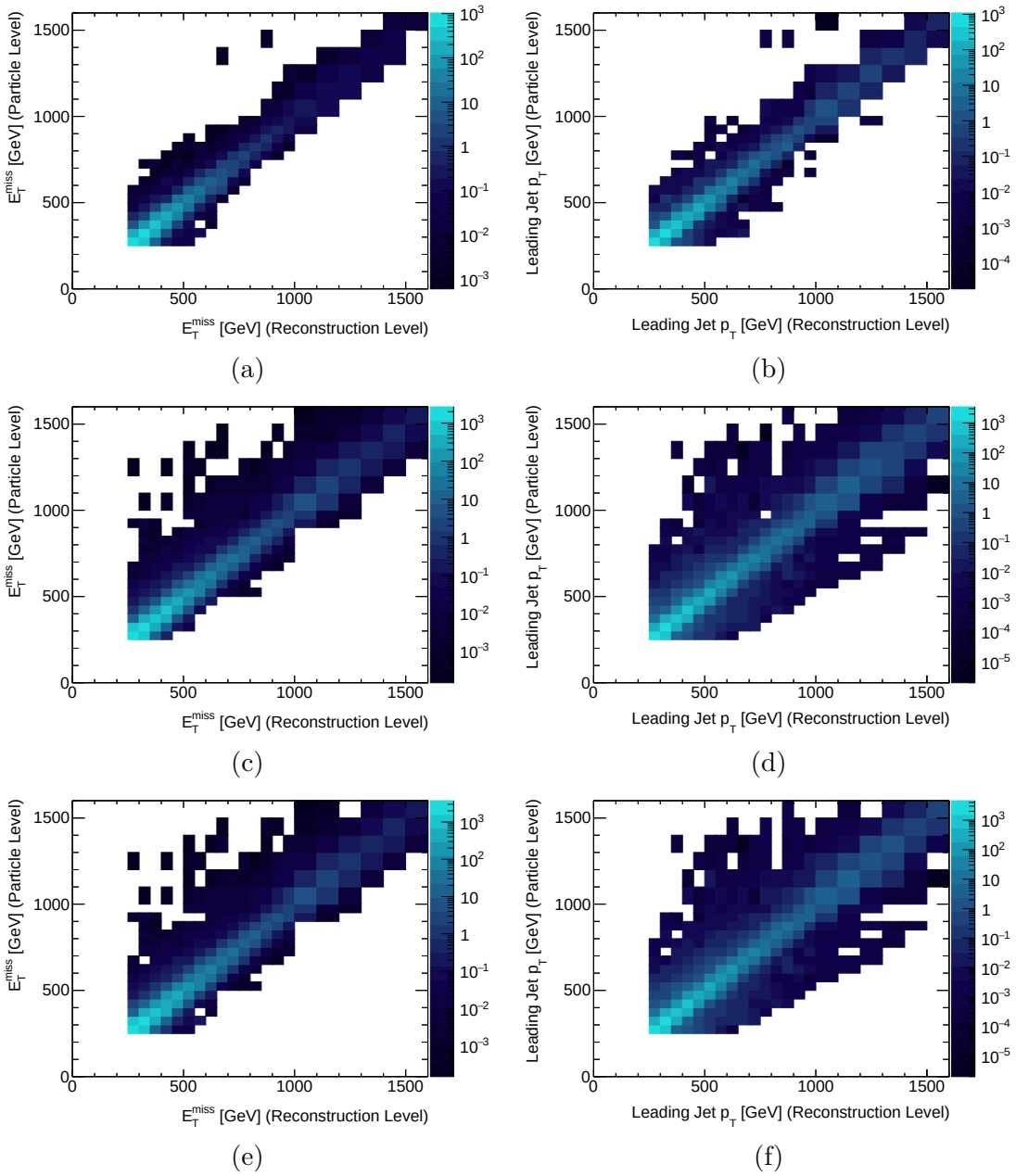

Figure 4.9.: The response matrices for the missing transverse momentum (a,c,e) and the transverse momentum of the leading jet (b,d,f) for the $W \to \tau\nu$ (a,b), the $Z \to \nu\nu$ process (c,d) and the sum of the two processes (e,f) as used for topology unfolding.

Unfolding the reconstructed MC distribution yields

$$n_{unf}^{\text{1st step}}(T_i) = \frac{1}{\epsilon_i} \sum_{j=1}^{N_R} P(T_i|R_j) \cdot n_{rec}^{MC}(R_j) \tag{4.9}$$

$$= \frac{1}{\sum_{k=1}^{N_R} \frac{N_{ik}}{n_0^{MC}(T_i)}} \sum_{j=1}^{N_R} \frac{N_{ij}}{\sum_{l=1}^{N_T} (N_{lj} + n^{MC}(fakes_j))} \cdot n_{rec}^{MC}(R_j) \tag{4.10}$$

The reconstructed distribution of the MC simulation is the sum of the events that also pass the selection criteria on particle level plus the fake events

$$n_{rec}^{MC}(R_j) = \sum_{l=1}^{N_T} \left(N_{lj} + n^{MC}(fakes_j)\right). \tag{4.11}$$

Using this expression in equation (4.10) yields the final result for the unfolded distribution of the first unfolding step:

$$n_{unf}^{\text{1st step}}(T_i) = n_0^{MC}(T_i), \tag{4.12}$$

which is exactly the particle level distribution of the MC simulation. Therefore,

---

the basic principle of the closure test is to unfold the reconstructed distribution of the MC simulation that was used for the unfolding inputs and check if the result is equal to the MC particle level distribution.

The closure test is performed by unfolding each process individually and also by unfolding the sum of the two processes (topology unfolding). Figure 4.10 shows the results of the closure test for the missing transverse energy and the transverse momentum of the leading jet for unfolding the $Z \to \nu\nu$ process and for topology unfolding. The closure test for other distributions and for the unfolding of the $W \to \tau\nu$ process can be found in appendix A.3. The ratio plots show a very good agreement between the unfolded results and the particle level distribution. However, some small discrepancies can be noticed in a few bins, mostly at high energies. This can be explained again by negative MC weights. A bin on particle level can e.g. have a positive number of events, but is split into an input for the response matrix (events passing the criteria at particle level *and* reconstruction level) and an input for miss-events (events passing only the particle level criteria). If the number of events on particle level is small, e.g. at high energies, this splitting into response matrix and miss-events can produce a negative number of events for one of these inputs. This can also happen for the splitting of events into events for the response matrix and fake events. In addition, in each reconstruction bin of the response matrix there are particle level bins with low statistics and vice versa. These are the bins far away from the diagonal of the response matrix and therefore also negative number of events can occur here. A negative number of fake-, miss- or matched events is not physically. The fact that these negative numbers of events appear really means that there is not a sufficent amount of statistical power to make any prediction of these extrem phase spaces. Therefore, negative number of events are *not* used when building the unfolding matrix. This follows the intention to keep the physical meaning of the procedure but leads to small deviations in the closure test. However, having understood this effect, the result of the closure test demonstrates the correct implementation of the unfolding algorithm using Bayes' theorem.

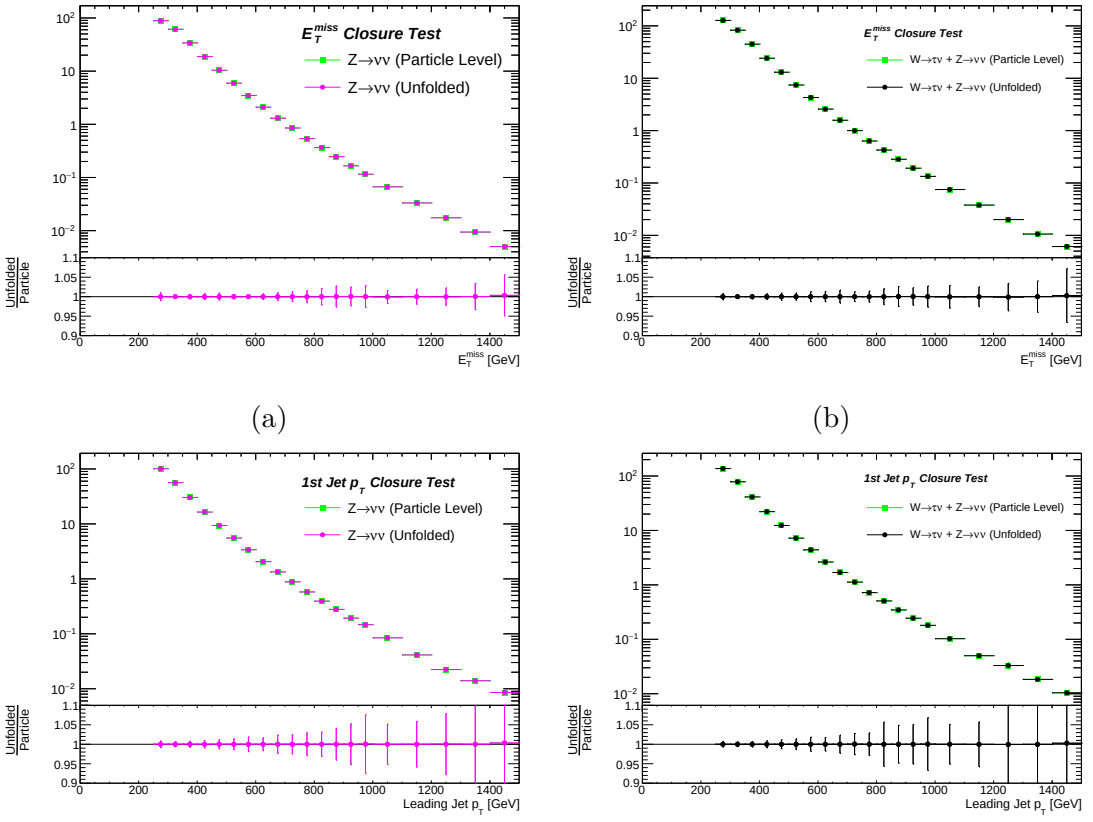

Figure 4.10.: The results of the closure test for the missing transverse energy (a,b) and the transverse momentum of the leading jet (c,d) for unfolding the $Z \to \nu\nu$ process (a,c) and for topology unfolding (b,d). The lower plots show the ratio between the unfolded result and the particle level distribution.

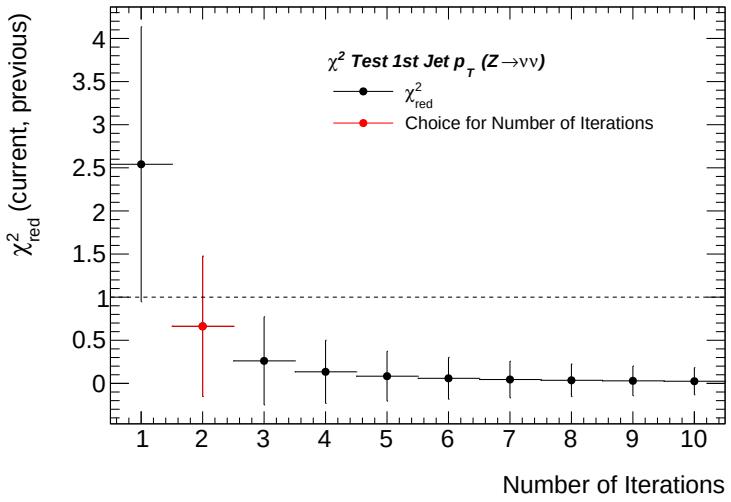

Figure 4.11.: The reduced χ^2_{red} distribution between the unfolded result of the current and the previous iteration for unfolding the transverse momentum distribution of the leading jet for the $Z \to \nu\nu$ process. The first bin shows the χ^2_{red} value between the distribution coming from the first step of the unfolding and the first iteration. For this case, performing two iterations results already into a reduced $\chi^2 < 1$.

4.5.3. Unfolded results

In order to unfold the pseudo-data distributions the number of iteration is chosen first. Afterwards three different ways of unfolding are performed. First, the two processes $Z \to \nu\nu$ and $W \to \tau\nu$ are unfolded individually. This means that for unfolding the $Z \to \nu\nu$ process the $W \to \tau\nu$ MC estimate is subtracted from the pseudo-data distribution and the remaining spectrum is unfolded with the unfolding matrix of the $Z \to \nu\nu$ process and vice versa. The third option is the topology unfolding method which means that the full pseudo-data is unfolded without performing a background subtraction. The unfolding matrix used here carries information from the MC simulations of both processes. All unfolding procedures are compared to the results of the so-called *bin-by-bin* unfolding and the corresponding particle level distributions.

Choosing the number of iterations The number of iterations is chosen with the help of the criterion defined in section 3.3. An example for the χ^2_{red} distributions discussed earlier is shown in figure 4.11 for unfolding the transverse momentum of the leading jet of the $Z \to \nu\nu$ estimate. The chosen number of iterations for all kinematic variables are listed in table 4.2 for the three unfolding procedures. For the missing transverse energy and the leading jet distribution the χ^2_{red} criterion is fulfilled after two iterations for all unfolding methods. The distribution of the transverse momentum of the second leading jet and the invariant mass of the two leading jets need four and three iterations to meet the criterion. One possible reason for this is the fact that the agreement between pseudo-data and MC background for these two variables is slightly worse compared to the $E_{\text{T}}^{\text{miss}}$ and the p_{T} distribution of the second leading jet. Therefore, the unfolding procedure needs to update the prior probability once or twice more often to get closer to the prior probability of the pseudo-data until convergence is reached. The criterion used shows a robustness against the choice of the unfolding method.

	Number of Iterations			
	$E_{\mathrm{T}}^{\mathrm{miss}}$	$p_{\mathrm{T}}^{j_1}$	$p_{\mathrm{T}}^{j_2}$	m_{jj}
$W \to \tau\nu$	2	2	4	3
$Z \to \nu\nu$	2	2	4	3
$Z \to \nu\nu$ + W$\to\tau\nu$	2	2	4	3

Table 4.2.: The number of iterations for the missing transvers energy, the transverse momentum of the leading and second leading jet and the invariant mass of the two leading jets for unfolding $W \to \tau\nu$ and $Z \to \nu\nu$ individually and for topology unfolding.

Unfolded distributions The unfolding is performed with the number of iterations described in the previous section. Figure 4.12 and figure 4.13 show the unfolded distributions for the missing transverse energy and the transverse momentum of the leading jet. The uncertainties shown include only the statistical uncertainty from the reconstructed pseudo-data distribution propagated through the unfolding as discussed in section 3.3. Other unfolded distributions can be found in appendix A.4. The figures also show the corresponding particle level distribution of the pseudo-data and the results from the bin-by-bin unfolding method. The latter is calculated for each bin via:

$$n_{unf}(T_i) = \frac{n^{MC}(T_i)}{n^{MC}(R_i)} \cdot n_{rec}(R_i). \tag{4.13}$$

Here, the reconstructed data distribution $n_{rec}(R)$ is multiplied by the ratio of the MC distribution on particle level and the MC distribution on reconstruction level in each bin. This procedure ignores any migration of events between bins. As can be seen in figure 4.12 and figure 4.13, the unfolding using Bayes' theorem and the bin-by-bin unfolding agree well at low energies where the purity is high and therefore less migration occurs compared to higher energies. Hence, the difference between the two methods gets larger with higher energies, but both approaches agree still within their statistical uncertainties. This reflects again that the amount of migration between bins is moderate. However, the iterative procedure using Bayes' theorem should be preferred over the bin-by-bin unfolding, because it accounts for the migration between bins and is therefore well-founded from a conceptional point of view. The unfolded results and the particle level simulations agree very well for the missing energy distribution even up to high energies. For the leading jet transverse momentum distribution the agreement worsens slightly at higher energies due to MC events with large weights. The $W \to \tau\nu$ distribution for example contains an event with a large positive weight in the bin $1200\,\mathrm{GeV} < p_{\mathrm{T}} < 1300\,\mathrm{GeV}$ of the particle level distribution (compare section 4.4, figure 4.5) leading to an excess of events in the unfolded distribution in this bin and through migration also in the neighboring bins. In the same bin the particle level distribution of the $Z \to \nu\nu$ pseudo-data distribution has an excess due to an event with a large weight, which also worsens the agreement between the unfolded result and the particle level distribution.

This observation underlines the importance of using MC simulations with a sufficient amount of statistics for the unfolding in order to minimize the influence of simulated events with large weights.

Topology unfolding has in general a higher statistical power, which reduces the effect of this problem.

Since the unfolding accounts for bin to bin migration, it correlates the uncertainties between bins. To visualize this, the correlation matrix, discussed in section 3.3, is given for each unfolded distribution in figure 4.12 and figure 4.13 for the statistical uncertainties of the reconstructed pseudo-data distribution. A value of one, minus one or zero reflects fully correlated, fully anti-correlated or fully uncorrelated uncertainties. The correlation of uncertainties between bins can be interpreted as moderate. The correlation seems to be significant only for directly neighboring bins. For projects like [48], which aim at setting limits on physical models from combining different analysis, it is very important to publish information about the correlation of the uncertainties between different bins. The reason for this is that the full potential of combining different analysis can only be exploited if the combination takes the correlation of the uncertainties among different analyses into account.

Therefore, researchers using unfolding techniques in their analyses should be encouraged to include information about the correlation of uncertainties when publishing their analyses.

4.5.4. Definition of uncertainties

This section discusses the uncertainties that are considered in the analysis and partially also in chapter 5. Besides the statistical uncertainties of the distributions that are unfolded several sources of systematic uncertainties are taken into account: the limited statistics of the MC simulation used for the unfolding, the resulting bias of choosing the prior probability, the cross section of the MC processes as well as the shape of the pseudo-data distribution. Possible differences in the impact that these uncertainties have on the unfolded distributions between the conventional way of unfolding and the topology unfolding method are studied in section 4.7.

Statistical uncertainty

The statistical uncertainty of the reconstructed distribution that is unfolded is propagated through the unfolding procedure as discussed in section 3.3. This uncertainty propagation takes into account that the unfolding matrix itself is affected by the statistical uncertainties of the reconstructed distribution after the first unfolding step, because for the first iteration the prior probability is calculated using the unfolded result of the first unfolding step. This method of handling the statistical uncertainties was validated e.g. in [49] by comparing it to a different method using toy MC samples.

Since the full data yield is unfolded in topolgy unfolding, the relative statistical uncertainty on the result is expected to be smaller compared to the conventional unfolding method in which only one process is unfolded.

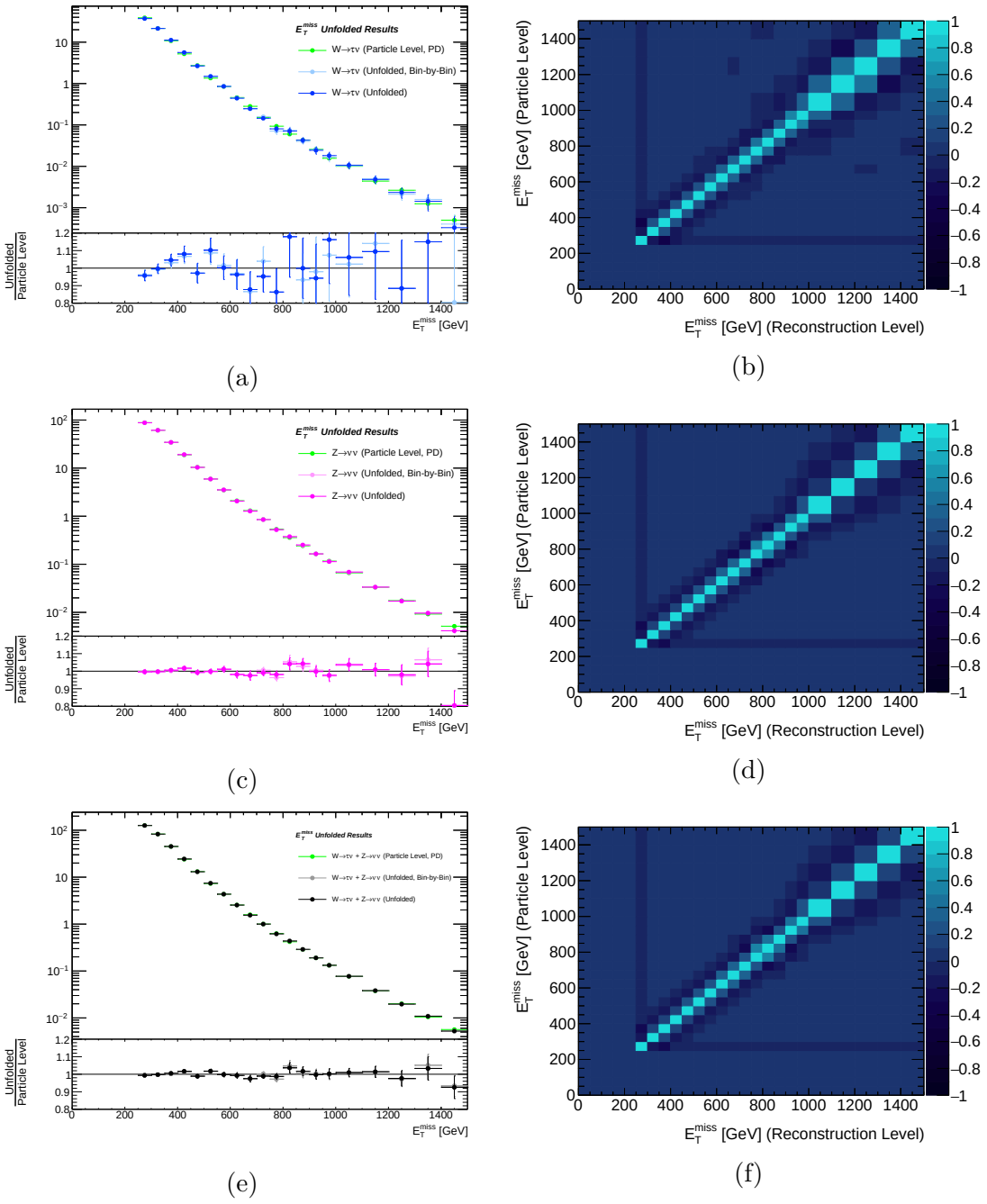

Figure 4.12.: Unfolded distributions for the transverse missing energy and the correlation matrices of the statistical uncertainty coming from the reconstructed pseudo-data distribution for unfolding the $W \to \tau\nu$ (a,b), the $Z \to \nu\nu$ (c,d) process and topology unfolding (e,f). The unfolded result is compared to the result obtained from bin-by-bin unfolding and the particle level distribution of the pseudo-data (PD, green).

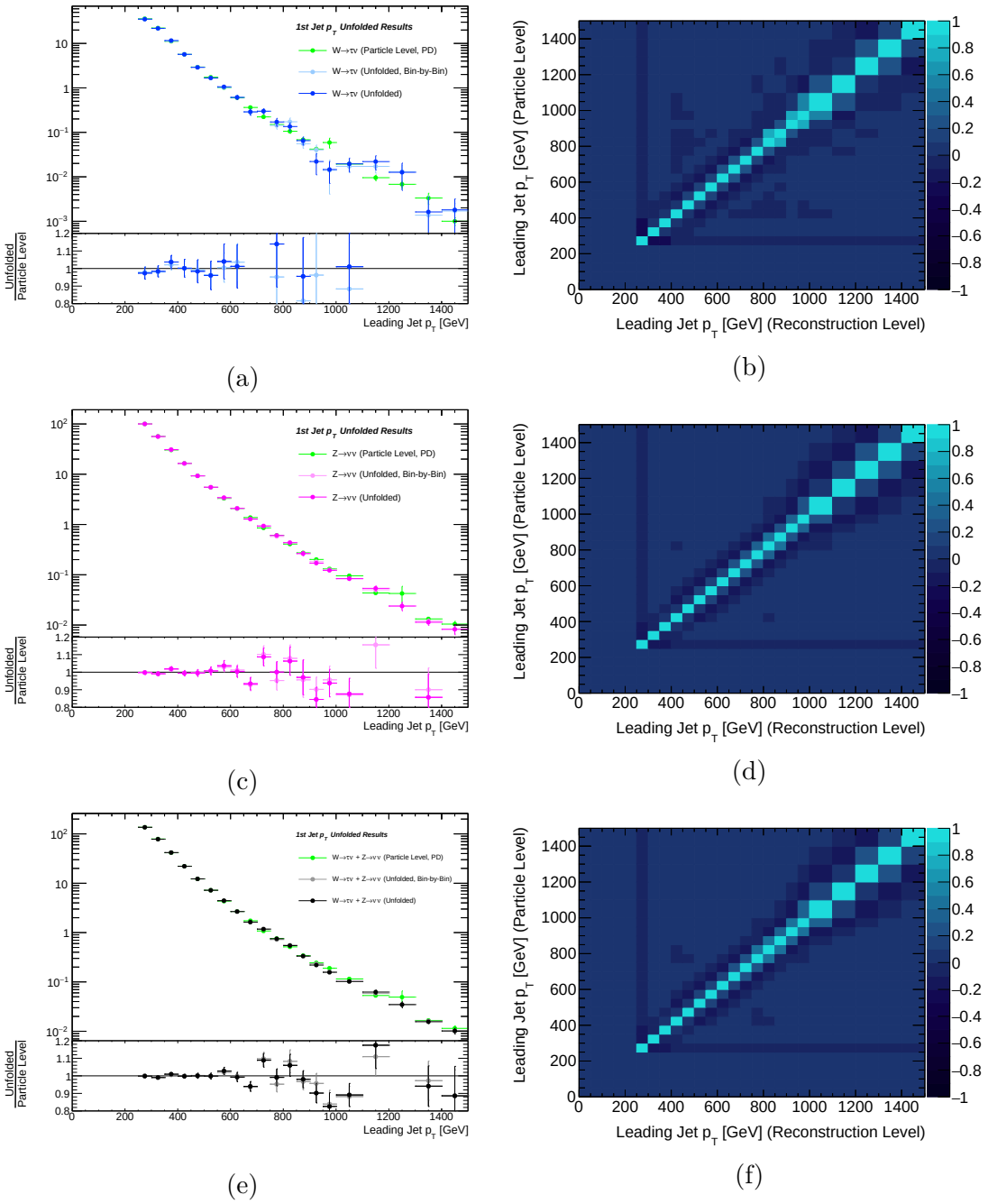

Figure 4.13.: Unfolded distributions for the transverse momentum of the leading jet and the correlation matrices of the statistical uncertainty coming from the reconstructed pseudo-data distribution for unfolding the $W \to \tau\nu$ (a,b), the $Z \to \nu\nu$ (c,d) process and topology unfolding (e,f). The unfolded result is compared to the result obtained from bin-by-bin unfolding and the particle level distribution of the pseudo-data (PD, green).

Systematic uncertainty from limited MC statistics

The limited statistics from the MC simulation used as input for the unfolding results in a systematic uncertainty on the unfolded result. To estimate this uncertainty, each entry of the response matrix is varied by drawing random numbers for each bin from a Gaussian distribution. The mean of the Gaussian distribution corresponds to the nominal entry of the bin and its width to the statistical uncertainty of the bin entry. Each bin of the fake- and miss-events is varied simultaneously in the same way. After having varied each bin of the response matrix as well as the estimate of the fake- and miss-events, the nominal distribution is unfolded with the new matrix and the new fake- and miss-estimates. This procedure is repeated 100 times for each distribution, giving 100 outcomes of the unfolded distribution. The systematic uncertainty for the i-th bin of the unfolded distribution is defined as the standard deviation of the distribution that is build from the 100 unfolded results of the bin i.

The topology unfolding method can be more robust against these variations of the unfolding matrix, because it is built from several processes and not from only one like in the conventional way of unfolding.

Systematic uncertainty from MC cross section

The cross section used for the MC simulations is not exactly known because of uncertainties on theoretical input parameters like the renormalization and factorization scale, the parton density function (PDF) or the modeling of the initial and final state radiation. Since this chapter describes a proof of concept study, the exact value of this uncertainty is not deciding and therefore the uncertainty on the cross section is taken to be 10 % for both processes. This corresponds to the typical order of magnitude for these uncertainties. The value of the cross section of one processes is increased and decreased by 10% and the unfolding is performed again for both cases. The associated systematic uncertainty is defined as the maximal difference in each bin between the nominal unfolded result and the result obtained from performing the unfolding with the lowered or increased cross section.

It is important to notice that an uncertainty on the cross section used in the MC simulation affects the two unfolding methods differently. The conventional unfolding method unfolds a background subtracted data distribution with an unfolding matrix built from the MC simulation of a single process, e.g. $Z \to \nu\nu$. A variation of the cross section has no effect on the matrix, since it contains only probabilities and efficiencies obtained from number of event ratios of this simulation. An overall change of the normalization has no effect. However, in case that MC simulation is used for the background subtraction, a variation of the cross section affects the reconstructed distribution that is unfolded through this subtraction of the backgrounds. This is not the case for the topology unfolding method, because here no background subtraction is performed. The unfolding matrix is not built from a single process and has contributions from different processes in this method. Here, the change of the cross section affects the unfolding matrix, because it changes the relative contribution of the different processes. Since the matrix is dominated by one process and the unfolding matrix of the different processes is not expected to be very different, the topology unfolding can be less sensitive to such an uncertainty.

The uncertainty of the MC cross sections affects the two unfolding methods in a different way. The topology unfolding method is supposed to be more stable against such an uncertainty.

Systematic uncertainty from MC mis-modeling

The following procedure estimates the uncertainty coming from a possible mis-modeling of the shape of the MC simulation on particle or parton level. With a perfect modeling of the parton and particle level distribution as well as a perfect detector simulation, the reconstructed MC distribution would look exactly like the data distribution.

In this test, every discrepancy between the reconstructed MC distribution and the data is interpreted as a result of a mis-modeling of the MC simulation at parton or particle level.

The detector simulation is assumed to be perfect. Ideally, to perform this test, a new particle or parton level distribution would be generated, which would result in a reconstructed MC distribution that looks exactly like the data distribution. Then, the unfolding would be performed using this new MC simulation and the difference to the unfolded result obtained from using the nominal MC simulation could be used as an uncertainty. However, the generation of a new MC simulation presents a far too big effort for the underlying purpose. Therefore, the following procedure is performed in order to estimate this uncertainty.

First, a *reweighted reconstructed* MC distribution is obtained by multiplying a weight to each bin of the nominal reconstructed MC distribution that contains only events which pass the selection criteria at reconstruction as well as at particle or parton level. This reconstructed distribution is obtained bin by bin from the response matrix by adding up all entries of a column

$$\mathrm{MC}_i^{\mathrm{reco}'} = \sum_{k=1}^{N_T} N_{ki}. \tag{4.14}$$

Miss- or fake-events are not considered in this uncertainty since they present only a minor contribution for the presented event selection. Each bin i of this reconstructed MC distribution is multiplied by a weight w_i. This weight is calculated by dividing the number of events of the data distribution by the number of events of the reconstructed MC distribution in this bin:

$$w_i = \frac{N(\mathrm{data})_i}{N(\mathrm{MC})_i}. \tag{4.15}$$

The reweighted MC distribution shows now, per construction, a perfect agreement with the data distribution.

Second, a *reweighted parton or particle level* MC distribution is obtained bin by bin by adding all entries of a column, each weighted by the factor w_j, of the response matrix N

$$\mathrm{MC}_i^{\mathrm{particle}'} = \sum_{j=1}^{N_R} N_{ij} w_j. \tag{4.16}$$

Effectively, the weights from comparing the reconstructed MC distribution with data are transfered through the response matrix in order to obtain a particle or parton level distribution $\mathrm{MC}_i^{\mathrm{particle}'}$ which results in a reconstructed MC distribution that agrees well with data when applying the detector simulation to it.

Finally, the reweighted MC distribution $\mathrm{MC}_i^{\mathrm{reco}'}$ is unfolded using the nominal response matrix. The difference between the unfolded result and the reweighted parton or particle MC distribution $\mathrm{MC}_i^{\mathrm{particle}'}$ is interpreted as a systematic uncertainty coming from a mis-modeling of the MC simulation on parton or particle level.

Systematic shape uncertainty

The influence of a systematic uncertainty modifying the shape of the reconstructed distributions is studied. Such an uncertainty corresponds for example to variations of the jet energy scale in a real analysis distorting e.g. the shape of the leading jet p_{T} distribution.

To simulate such an uncertainty, the transverse momenta of all jets in the event are distorted by multiplying the jet momenta with a random number. The underlying distribution of the random numbers is a Gaussian distribution with a mean which varies as a function of the jet p_{T} from one to higher values and a width of 0.1. The shift of the mean is defined as

$$s = (p_{\mathrm{T}}[\mathrm{GeV}] - 250) \cdot \frac{0.5}{1500 - 250}, \tag{4.17}$$

where 250 and 1500 GeV are the beginning and the end of the spectrum of the leading jet p_{T}. Therefore, the shift changes between 0 ($p_{\mathrm{T}} = 250\,\mathrm{GeV}$) and 0.5 ($p_{\mathrm{T}} = 1500\,\mathrm{GeV}$) as a linear function of the jet p_{T}. The mean of the corresponding shifted Gaussian distribution takes values from 1 to a maximum of 1.5. The distortion of the distribution comes from the fact that all distributions considered in the unfolding show a falling spectrum towards higher energies. The distortion of the transverse momentum of e.g. the leading jet might migrate the corresponding entry of the leading jet distribution into one of the neighboring bins.

Since more events are located in the i-th bin compared to the i+1-th bin, more entries are expected to migrate from bin i to bin i+1 than from bin $i+1$ to bin i. This decreases the negative slope of the spectrum.

The difference of the distorted and the nominal distributions is scaled by a factor of 0.01 in order to produce a realistic order of magnitude of the uncertainty. With these parameters a relative distortion of around 2 % can be reached for the $Z \to \nu\nu$ unfolding and the topology unfolding as shown in figure 4.14. This corresponds roughly to the order of magnitude of the jet energy scale uncertainty for central anti-$\mathrm{k_t}$ jets at the energy above 250 GeV [50]. For unfolding one process individually, the pseudo-data distribution and the MC background distribution of the second process are distorted. Then, the distorted MC background distribution is subtracted from the distorted pseudo-data. For topology unfolding, the pseudo-data distribution is distorted. As can be seen in figure 4.14, the relative change resulting from the distortion procedure is larger for the $W \to \tau\nu$ unfolding compared to the other unfolding procedures, because here the dominant background

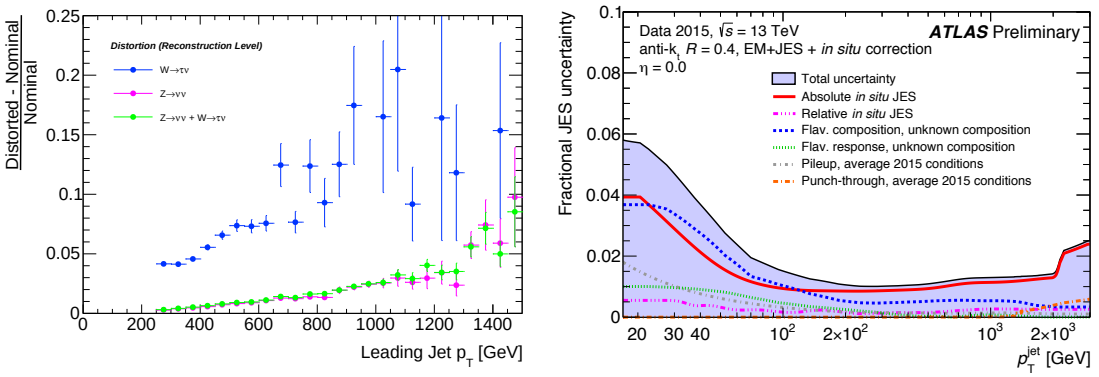

(a) (b)

Figure 4.14.: The relative difference between the distorted and nominal distribution as a function of the transverse momentum of the leading jet (a). For the $W \to \tau\nu$ process (blue), the distorted MC $Z \to \nu\nu$ distribution is subtracted from the distorted pseudo-data distribution. For the $Z \to \nu\nu$ process (magenta) the distorted MC $W \to \tau\nu$ distribution is subtracted from the distorted pseudo-data. For the topology unfolding input (green) the pseudo-data is distorted. The jet energy scale uncertainty for central anti-k_t jets is shown in (b) [50]. The order of magnitude of the uncertainties on reconstruction level is compatible for (a) and (b).

$(Z \to \nu\nu)$ is distorted and subtracted from the distorted pseudo-data, producing a larger relative change.

After the distortion of the transverse momenta of the jets in the event, all other variables based on these quantities are recalculated, including e.g. the missing transverse energy of the event, the invariant mass of the two leading jets and the number of jets. The event selection for the distorted values of the variables is done in parallel to the event selection for the nominal values. This procedure results in a duplicate of each distribution with a distorted shape. The distorted distribution is unfolded and the difference to the nominal unfolded result is interpreted as the underlying uncertainty.

4.5.5. Uncertainties of unfolded distributions

The uncertainties of the unfolded results are shown in figure 4.15 and figure 4.16. The total uncertainty is calculated as the square root of the quadratic sum of the single uncertainties. When unfolding the two processes $Z \to \nu\nu$ and $W \to \tau\nu$ individually, the uncertainty on the MC background cross section is important. For unfolding the dominant process $(Z \to \nu\nu)$ the cross section uncertainty of the other process is dominant at low and intermediate energies. For unfolding the sub-dominant process $(W \to \tau\nu)$, the cross section uncertainty for the $Z \to \nu\nu$ process is one of the dominant uncertainties over the whole energy spectrum. This underlines the crucial role the background subtraction plays for the result on reconstruction as well as on particle level for the conventional way of unfolding. The topology unfolding is not affected by this uncertainty. It is subdominant throughout the whole spectrum for all variables. The unfolding matrix is therefore quite insensitive to a shift of the contributions from the different processes. At higher energies the statistics of the reconstructed distribution becomes important for both unfolding strategies. Also the shape uncertainty plays an important role at higher energies for $Z \to \nu\nu$ and topology unfolding. The uncertainty from MC mis-modeling is

quite moderate except from a few excesses , which justifies the choice of the number of iterations in addition to the χ^2_{red} criterion. The limited statistics of the MC input to the unfolding seems to have no influence on the unfolded result.

4.6. Validation of topology unfolding

In order to validate the newly introduced topology unfolding method, its results are compared to the conventional way of unfolding, which refers to unfolding a single signal process of a data set after background subtraction. For this, the results of unfolding the $Z \to \nu\nu$ and the $W \to \tau\nu$ process individually (compare section 4.5.3) are added together, referred to as *process by process* (PbyP) unfolding. The results are compared to the results of topology unfolding. For this comparison, the statistical and the systematic uncertainties discussed in the previous section are included. Figure 4.17 shows the comparison of the unfolded results. For the great majority of the bins,

---

the two results from the different unfolding methods agree within their statistical uncertainties. This agreement validates the newly introduced topology unfolding procedure.

The direct comparison of the transverse momentum distribution of the second leading jet shows again that the topology unfolding is slightly more robust against distortion of the spectrum coming from large weights of the MC simulation. At high energies, the distributions indicate that the systematic and the statistical uncertainties of the process by process unfolding are larger compared to topology unfolding. However, this comparison is not of a fair nature, because in a real analysis the process by process unfolding would not be used. Instead, only the dominant process would be unfolded. This is the reason why the following section describes the comparison of the uncertainties between the topology unfolding method and unfolding only the $Z \to \nu\nu$ process.

4.7. Comparison of uncertainties

Figure 4.18 presents the relative fractions of the uncertainties described in section 4.5.4 for the $Z \to \nu\nu$ unfolding (magenta) and the topology unfolding (black) as a function of the missing transverse energy and the transverse momentum of the leading jet. These distribution of other observables are shown in appendix A.5. The statistical uncertainty of the reconstructed pseudo-data distribution results, as expected, for the $Z \to \nu\nu$ unfolding into a larger relative uncertainty of the unfolded distributions. The uncertainty coming from the limit MC statistics used for the unfolding has a significantly smaller contribution to the total uncertainty. For both unfolding methods this uncertainty is below 1 % for most parts of the distributions. Only the transverse momentum distribution of the second leading jet is more sensitive to this uncertainty at higher energies. However, this uncertainty does not show a significant difference between the two unfolding methods. The uncertainty coming from a potential mis-modeling of the MC simulation is also quite compatible between the two methods with the $Z \to \nu\nu$ unfolding showing a slightly higher fractional uncertainty. For the missing energy distribution, this uncertainty is at the 1 % level or below for both unfolding methods. The transverse momentum distributions of the leading and second leading jet show a small relative uncertainty at low energies

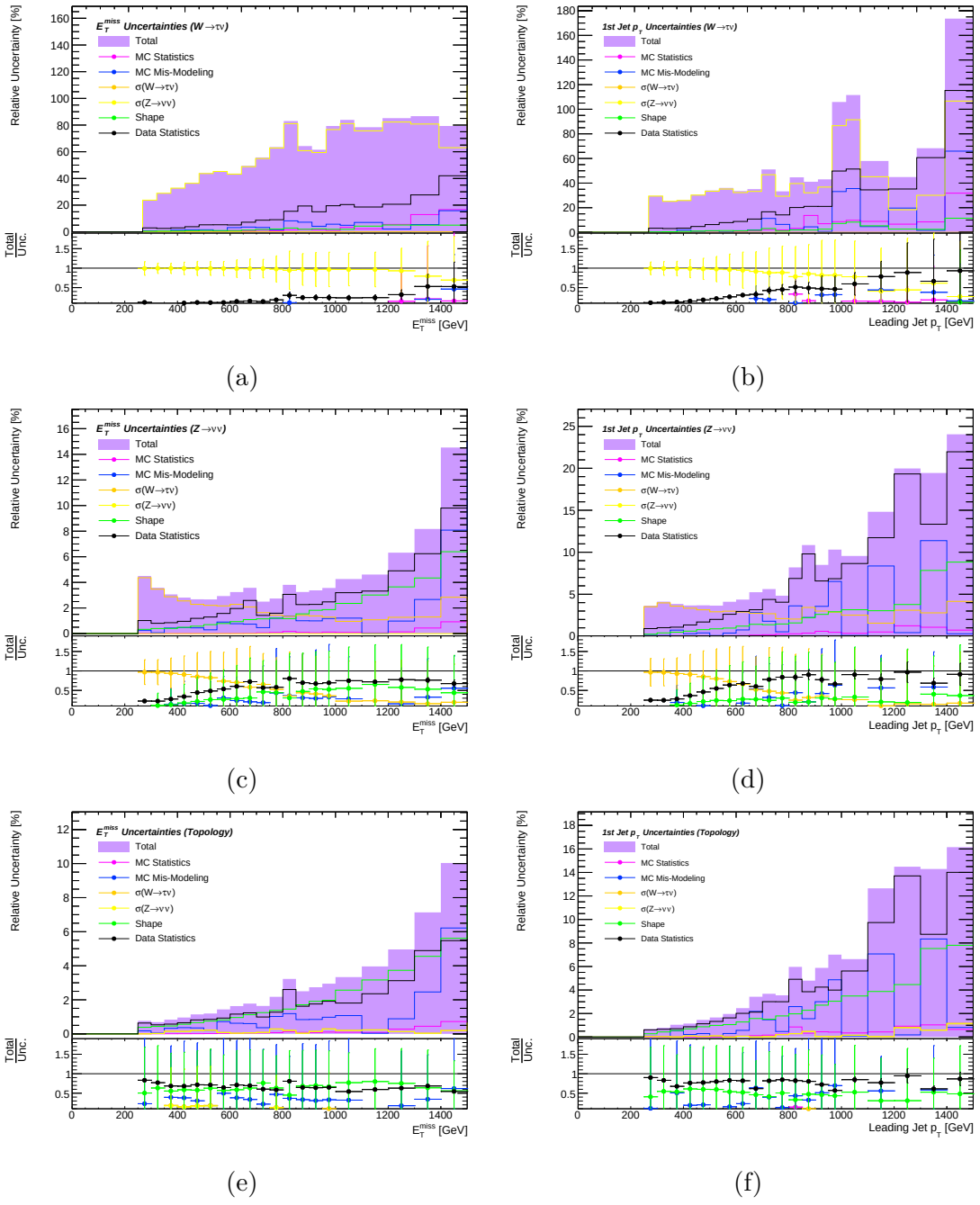

Figure 4.15.: The relative systematic uncertainties on the unfolded missing energy and the transverse momentum of the leading jet for unfolding the $W \to \tau\nu$ process (a,b), the $Z \to \nu\nu$ process (c,d) and topology unfolding (e,f).

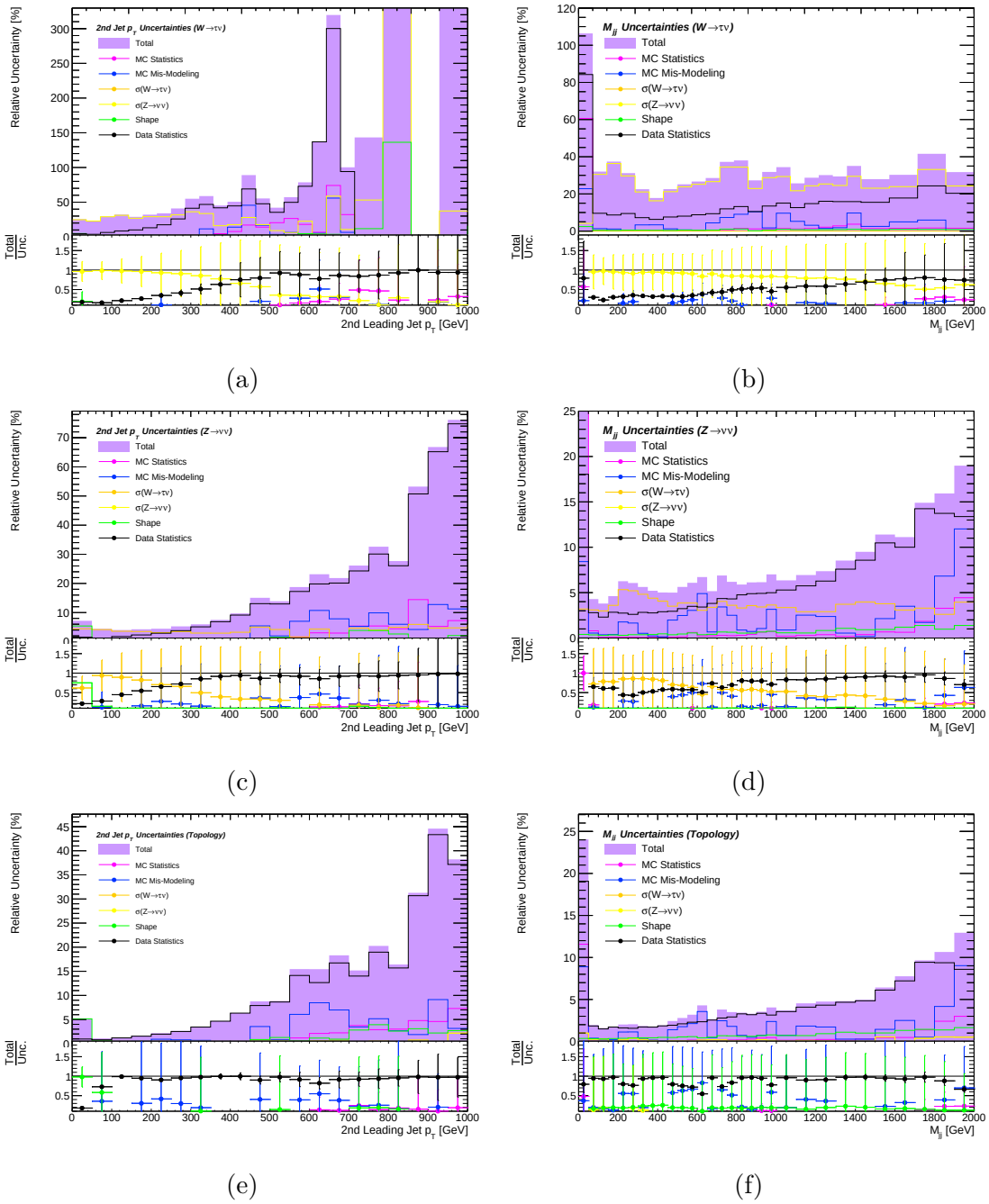

Figure 4.16.: The relative systematic uncertainties on the transverse momentum of the second leading jet and the invariant mass of the two leading jets for unfolding the $W \to \tau\nu$ process (a,b), the $Z \to \nu\nu$ process (c,d) and topology unfolding (e,f).

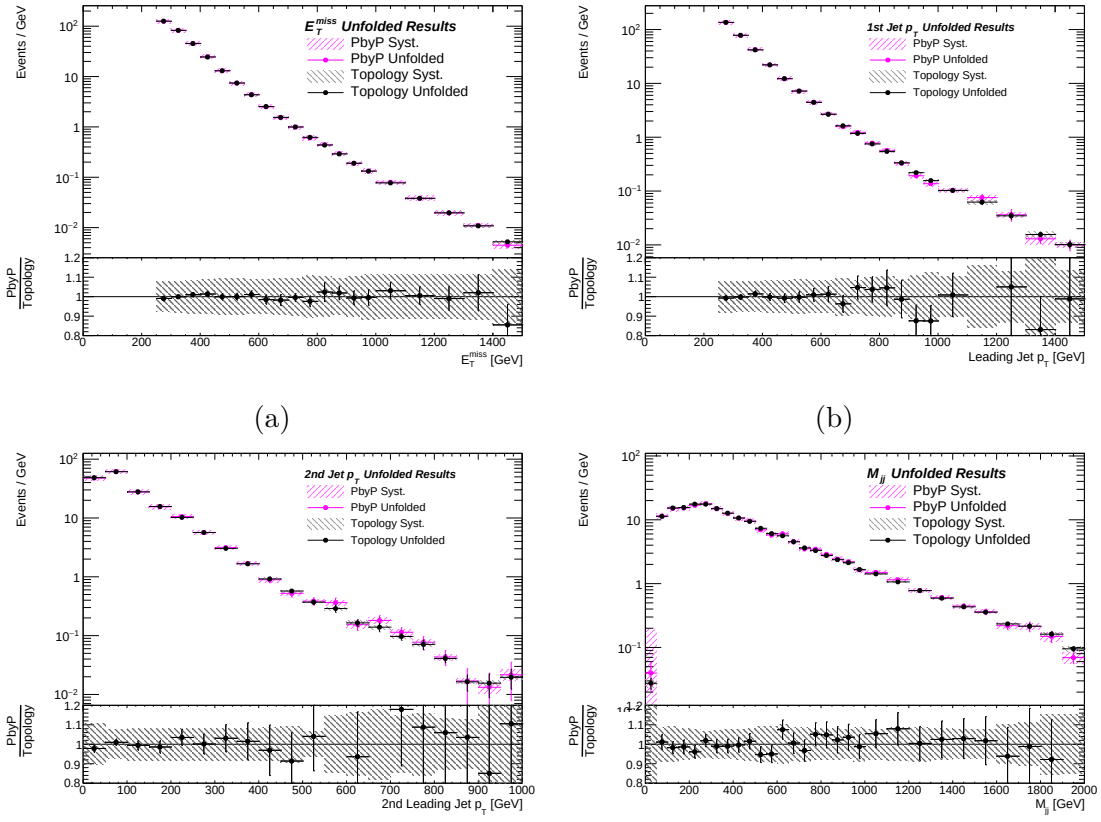

Figure 4.17.: Comparison of the topology unfolding method and the process by process (PbyP) unfolding. The lower plots show the ratio of the unfolded results obtained by the two different methods of unfolding. Here, the uncertainty band reflects the systematic uncertainties.

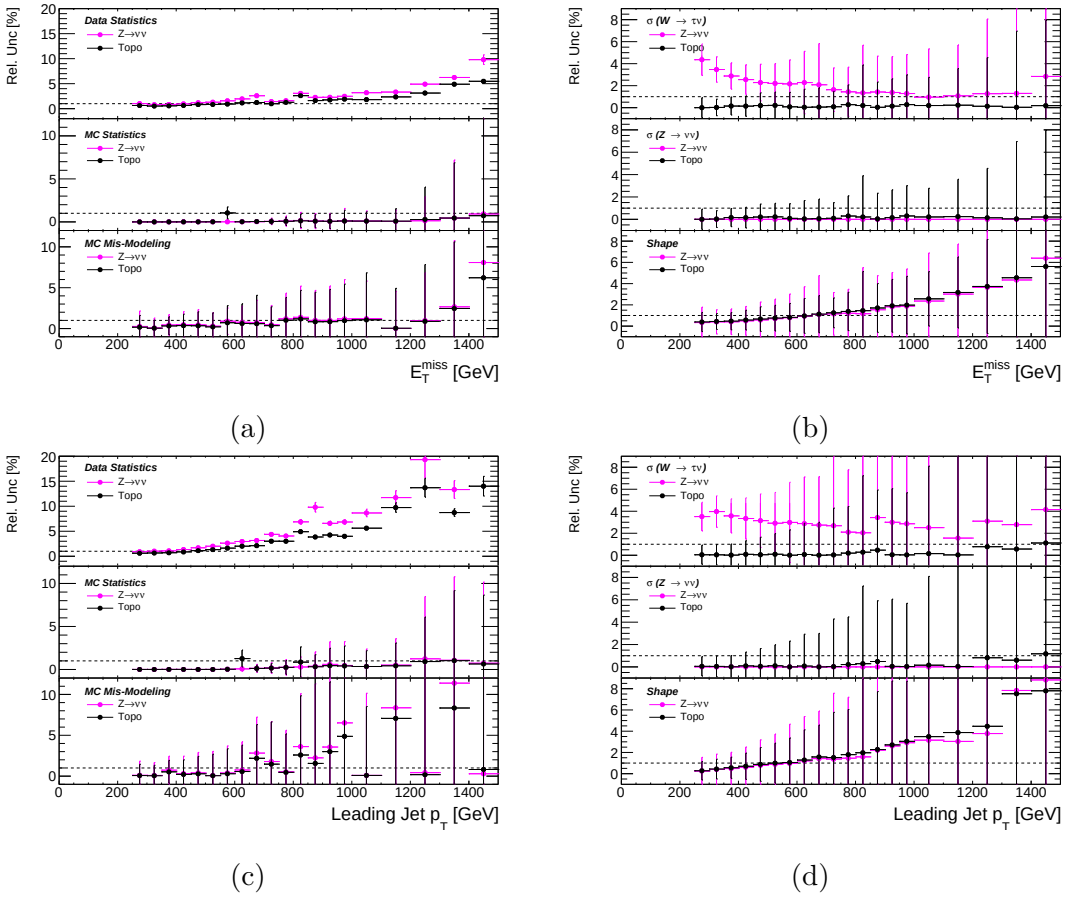

Figure 4.18.: Relative uncertainties for the $Z \to \nu\nu$ unfolding (magenta) and the topology unfolding (black) for the missing transverse energy (a,b) and the transverse momentum of the leading (c,d).

with some spikes towards the end of the spectra. The uncertainties on the $Z \to \nu\nu$ and the $W \to \tau\nu$ cross section are not affecting the topology unfolding significantly. This uncertainty stay below the one percent level except for the very last bin of the transverse momenta distribution of the leading and second leading jet. This shows again that the unfolding matrix of the topology unfolding matrix is largely unaffected by changes in the relative contribution of the different processes. The $Z \to \nu\nu$ unfolding is sensitive to the cross section of the $W \to \tau\nu$ through the background subtraction resulting in a significant uncertainty for all tested distributions. The shape uncertainty on the reconstructed distributions result in a significant uncertainty on the unfolded distributions at higher energies for the missing transverse energy and the transverse momentum of the leading jet. Both unfolding methods show a very similar behavior for this uncertainty.

In conclusion,

---

the difference in the uncertainty between the two unfolding methods is coming from the statistical uncertainty of the reconstructed distributions and the uncertainty on the MC background cross section,

---

which affects the $Z \to \nu\nu$ unfolding significantly through the background subtraction. This results in a much smaller overall uncertainty at low energies, which can be seen

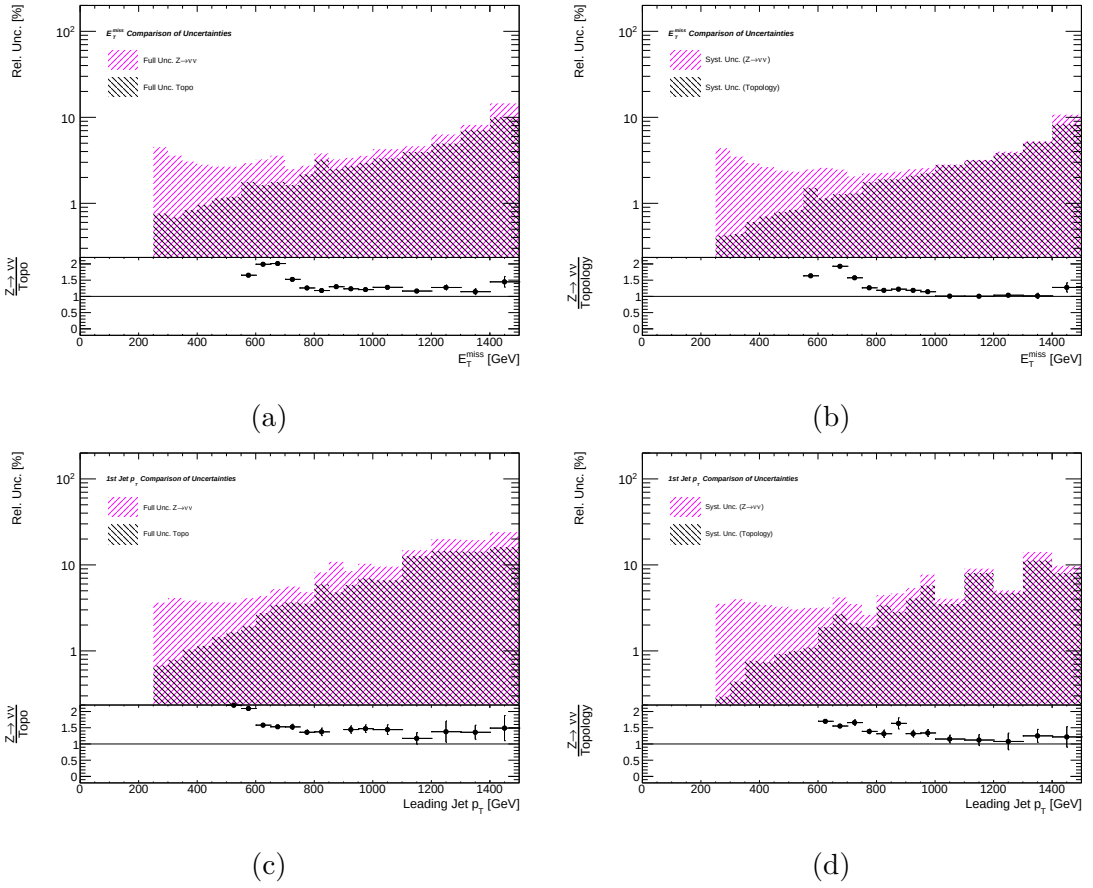

Figure 4.19.: Full relative uncertainty (a,b) and the full relative systematic uncertainty (c,d) for the missing transverse energy and the transverse momentum of the leading jet. The lower plots show the ratio of the relative uncertainties of the $Z \to \nu\nu$ unfolding and the topology unfolding.

in figure 4.19 for the missing transverse energy and the transverse momentum of the leading jet. Additional distributions are shown in appendix A.5. At higher energies, the statistical uncertainty dominates leading to a 20 % to 60 % smaller uncertainty for the topology unfolding method. The systematic uncertainty is compatible between the two methods at higher energies. All in all, the results of the topology unfolding method are shown to be compatible with the conventional way of unfolding and its uncertainties are smaller than or compatible with the uncertainties from unfolding the dominant SM process. These results are produced for different kinematic distributions having different reconstruction efficiencies and fake rates, which shows a robustness of the results against variations in these input parameters for the unfolding. Therefore, the topology unfolding method is validated and the smaller uncertainties compared to the conventional way of unfolding offers a promising opportunity to use topology unfolding in searches for new physics.

5. Topology unfolding for a monojet search

This chapter explores the possibility of setting limits on parameters of theories describing physics beyond the SM with the unfolded results of a monojet search. The object and event selection previously defined in section 4.2 is applied to the proton-proton collision data provided by the LHC in 2015, corresponding to an integrated luminosity of 3.2 fb^{-1}. After estimating the contribution from SM processes to the event yield (section 5.1), the detector level results are presented in section 5.2. The treatment of systematic uncertainties is discussed in section 5.2.1. Afterwards, the missing transverse energy distribution is unfolded using the topology unfolding method and, for comparison, the $Z \to \nu\nu$ unfolding in section 5.3. The limit setting procedure is explained in section 5.4.1. As a validation of the limit setting procedure model independent limits are obtained from the results on detector level (5.4.2) and compared to the result of [41]. Afterwards, the unfolded results are used to set limits on the fundamental planck scale of five different specifications of the ADD model (section 5.4.3). The resulting limits are compared between the two different methods of unfolding as well as to the limits obtained in [41] on detector level.

5.1. Background estimation

The contribution from SM processes to the event yield of the selection for the signal region is estimated by scaling the MC simulations in the signal region by an overall correction factor obtained from the $W \to \mu\nu$ control region. The correction factor accounts for an overall normalization discrepancy coming from the finite order calculation used in the MC simulation. The value of the correction factor is validated by comparing it to an alternative correction factor obtained from the $Z \to \mu\mu$ control region. Besides the simulation for the two dominant SM processes, $Z \to \nu\nu$ and $W \to \tau\nu$, already used in the previous chapter, the following subdominant processes are included as well: $W \to \mu\nu$, $W \to e\nu$, $t\bar{t}$ and single top quark processes as well as diboson and $Z \to \mu\mu$ events. Non-collision backgrounds, multijet as well as $Z \to ee$ and $Z \to \tau\tau$ events are neglected in this study, because their contribution to the event yield of the signal region is altogether smaller than 1 % [41].

The correction factor $f_{W\to\mu\nu}$ ($f_{Z\to\mu\mu}$) is obtained by dividing the overall event yield in data by the overall event yield of the MC simulations of the SM processes in the $W \to \mu\nu$ ($Z \to \mu\mu$) control region. The following values are obtained

$$f_{W\to\mu\nu} = \frac{N(\text{Data})^{\text{CR}_{W\to\mu\nu}}}{N(\text{MC})^{\text{CR}_{W\to\mu\nu}}} = 0.97 \pm 0.02 \tag{5.1}$$

$$f_{Z\to\mu\mu} = \frac{N(\text{Data})^{\text{CR}_{Z\to\mu\mu}}}{N(\text{MC})^{\text{CR}_{Z\to\mu\mu}}} = 0.92 \pm 0.03, \tag{5.2}$$

where the quoted uncertainty refers to the statistical uncertainty. Both correction factors have values close to one and agree within their statistical uncertainty validating the procedure. Figure 5.1 shows the missing energy distribution of the data and the MC simulation for the SM processes in the $W \to \mu\nu$ ($Z \to \mu\mu$) control region before and

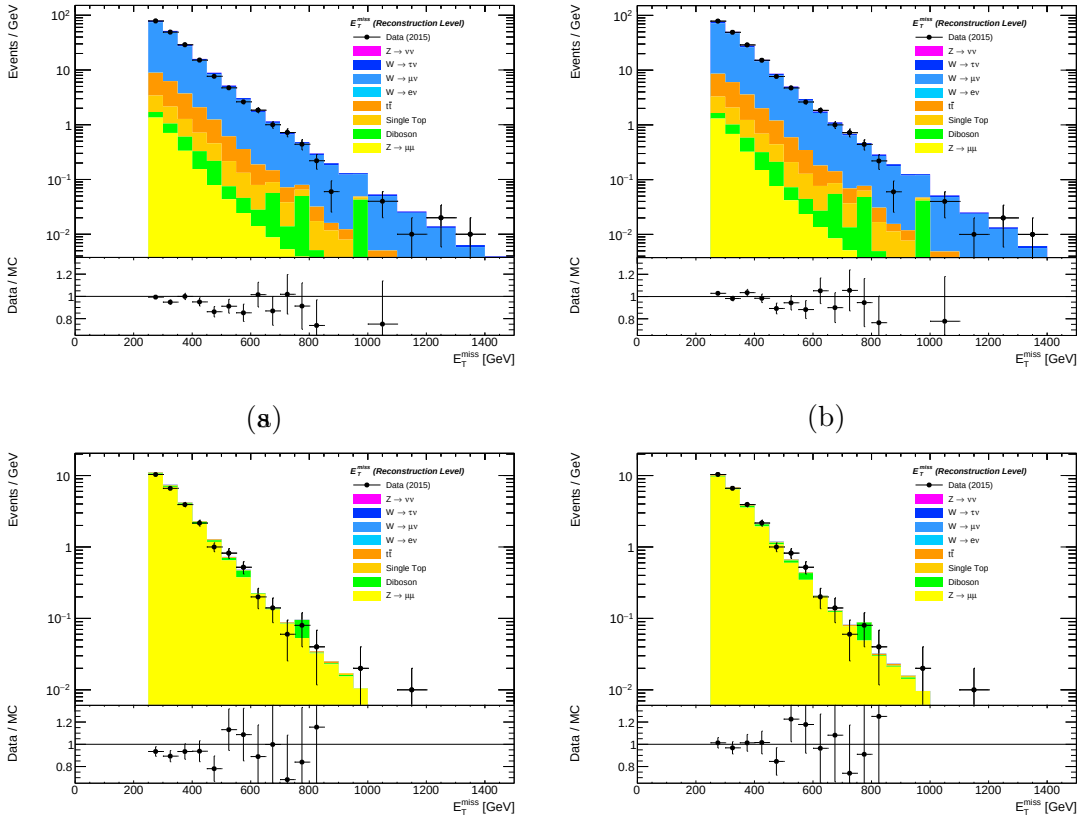

Figure 5.1.: The missing energy distribution for data (black) and the SM background estimate (colored) in the $W \to \mu\nu$ (a,b) and the $Z \to \mu\mu$ (c,d) control region before (a,c) and after (b,d) the application of the overall correction factor to the MC distributions.

after scaling the MC prediction with the correction factor $f_{W\to\mu\nu}$ ($f_{Z\to\mu\mu}$). Applying the correction factors to the MC distributions in the control region improves the agreement between data and MC background, which can be seen by comparing the lower ratio plots of figure 5.1 (a) and (b) or (c) and (d). The $W \to \mu\nu$ control region shows a higher statistical power for the underlying selection. Therefore, the factor $f_{W\to\mu\nu}$ is used to scale the reconstruction level MC distributions in the signal region for the following studies.

5.2. Results at reconstruction level

The distribution at reconstruction level for data and the background estimate of the SM processes after scaling the MC simulations by the correction factor $f_{W\to\mu\nu}$ can be seen in figure 5.2 for the transverse missing energy and the transverse momentum of the leading jet. Both distributions show a reasonable agreement between data and the SM prediction, since most of the bin values in the ratio plot agree with one within their statistical uncertainties. In addition, no singificant difference in the shape between the data and the sum of the SM processes is observed. This level of agreement is compatible with the level of agreement in the published monojet search [41]. No significant excess

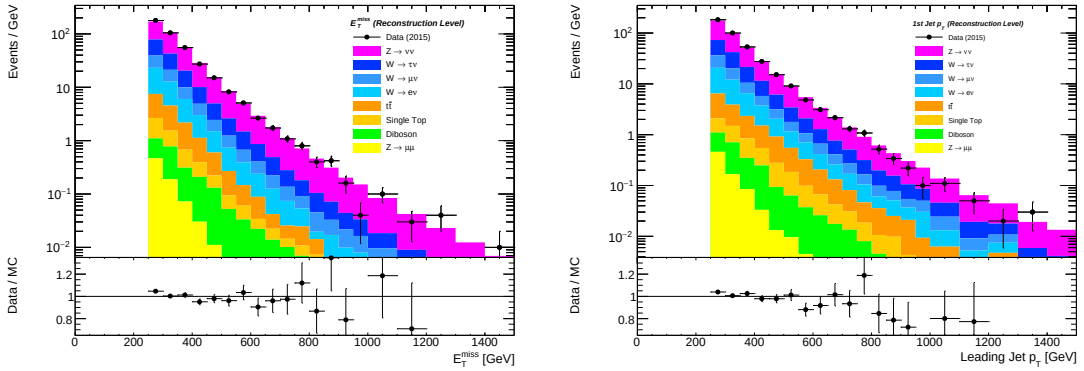

(a) (b)

Figure 5.2.: The missing transverse energy distribution (a) and the transverse momentum distribution of the leading jet (b) for data (black) and the estimate of the SM processes (colored). The lower plots show the ratio of the data and the sum of the SM processes with the statistical uncertainties.

above the SM expectation is observed in both distributions.

5.2.1. Systematic uncertainties and event yield

Since this thesis aims at exploring the possibilities of a new analysis concept based on topology unfolding using the selection of an already published ATLAS analysis [41], rather than carrying out an established analyzing method for a not yet published search signature, the estimate of the systematic uncertainties is not repeated. Instead, the estimate for the relative uncertainties in the signal region on detector level are obtained from [41]. In [41] the dominant SM background processes, $Z \to \nu\nu, \tau\tau, \mu\mu$ and $W \to e\mu, \mu\nu, \tau\nu$ in association with jets, are estimated with a semi data-driven method using several control regions. To estimate the contribution of a SM process in the signal region, the data yield of the control region is subtracted by the MC estimate of all other processes in that control region and multiplied by a transfer factor. The transfer factor is first estimated as the ratio of the MC yield of the process in the signal region and the MC yield of the process in the control region. In a simultaneous fit over all control regions the final transfer factors are obtained. All systematic uncertainties are treated as nuisance parameters with a Gaussian shape in this fit. This method has two main advantages. First, many experimental and theoretical uncertainties that affect the MC prediction are greatly reduced by taking the ratio of the MC distributions of the signal and the control region for the transfer factor. Second, the fit takes correlation of the uncertainties into account. The dominant systematic uncertainties are coming from the jet energy scale and resolution, the renormalization and factorization scale as well as uncertainties coming from the parton distribution function. For this analysis, the same relative uncertainties are used for the results of the previous section. The event yield in the signal region for data as well as the total SM prediction and the corresponding uncertainties are given in table 5.1 and table 5.2 for several inclusive and exclusive regions of the missing transverse energy. The inclusive regions are used later on to set model-independent limits, the exclusive ones are used for setting limits on the ADD model. The data event yield agrees within the uncertainties with the event yield of the total SM prediction for every inclusive and exclusive region. The fractional contribution of each process to the SM prediction

Region $E_{\mathrm{T}}^{\mathrm{miss}}$ [GeV]	> 250	> 300	> 350	> 400
Data (2015)	20063	11143	5919	3153
SM prediction	19728 ± 853	11205 ± 518	5997 ± 310	3265 ± 193
$Z \to \nu\nu$	59 %	62 %	65 %	67 %
$W \to \tau\nu$	21 %	19 %	18 %	17 %
$W \to \mu\nu$	8 %	7 %	7 %	6 %
$W \to e\nu$	8 %	7 %	6 %	5 %
$t\bar{t}$	3 %	3 %	3 %	2 %
t	1 %	1 %	1 %	1 %
Diboson	1 %	1 %	1 %	1 %
$Z \to \mu\mu$	< 1 %	< 1 %	< 1 %	< 1 %

Region $E_{\mathrm{T}}^{\mathrm{miss}}$ [GeV]	> 500	> 600	> 700
Data (2015)	1044	381	163
SM prediction	1071 ± 73	400 ± 35	165 ± 20
$Z \to \nu\nu$	71 %	73 %	76 %
$W \to \tau\nu$	16 %	14 %	12 %
$W \to \mu\nu$	6 %	6 %	6 %
$W \to e\nu$	5 %	4 %	4 %
$t\bar{t}$	2 %	1 %	1 %
t	1 %	1 %	1 %
Diboson	1 %	1 %	1 %
$Z \to \mu\mu$	< 1 %	< 1 %	< 1 %

Table 5.1.: Event yield for data and SM prediction in the signal region on reconstruction level for different *inclusive* missing transverse energy regions. The uncertainties given for the SM prediction include systematic and statistical uncertainties and take correlations into account. In addition the contribution of each SM process to the SM prediction is given.

shows that only the $Z \to \nu\nu$ and $W \to e\nu, \mu\nu, \tau\nu$ processes in association with jets give a significant contribution for the presented selection.

5.3. Unfolding

The missing energy distribution of the signal region is unfolded with two different methods, unfolding only the $Z \to \nu\nu$ process after subtracting the other backgrounds from the reconstructed data distribution and topology unfolding. The choice for the number of iterations is determined in the same way as in section 4.5.3. The corresponding χ^2_{red} values can be found in appendix B.2. The test yields two iterations for $Z \to \nu\nu$ unfolding and three iterations for topology unfolding. Since the reconstructed MC distributions are scaled by the factor $f_{W\to\mu\nu}$, the MC distribution on particle level and the response matrices are also scaled by the same factor in order to keep a consistent normalization between reconstruction and particle level. The response matrices used for the unfolding can be found in appendix B.3.

Region $E_{\mathrm{T}}^{\mathrm{miss}}$ [GeV]	250 - 300	300 - 350	350 - 400
Data (2015)	8920	5224	2766
SM prediction	8523 ± 372	5208 ± 235	2732 ± 145
$Z \to \nu\nu$	54 %	59 %	63 %
$W \to \tau\nu$	23 %	21 %	19 %
$W \to \mu\nu$	10 %	8 %	7 %
$W \to e\nu$	9 %	8 %	7 %
$t\bar{t}$	3 %	3 %	3 %
t	1 %	1 %	1 %
Diboson	< 1 %	1 %	< 1 %
$Z \to \mu\mu$	< 1 %	< 1 %	< 1 %

Region $E_{\mathrm{T}}^{\mathrm{miss}}$ [GeV]	400 - 500	500 - 600	600 - 700
Data (2015)	2109	663	218
SM prediction	2194 ± 136	671 ± 49	235 ± 24
$Z \to \nu\nu$	66 %	69 %	71 %
$W \to \tau\nu$	18 %	16 %	15 %
$W \to \mu\nu$	7 %	6 %	6 %
$W \to e\nu$	6 %	5 %	5 %
$t\bar{t}$	3 %	2 %	2 %
t	1 %	1 %	< 1 %
Diboson	1 %	1 %	1 %
$Z \to \mu\mu$	< 1 %	< 1 %	< 1 %

Table 5.2.: Event yield for data and SM prediction in the signal region on reconstruction level for different *exclusive* missing transverse energy regions. The uncertainties given for the SM prediction include systematic and statistical uncertainties and take correlations into account. In addition the contribution of each SM process to the SM prediction is given.

Figure 5.3 (a,c) shows the result of the two unfolding methods compared to bin-by-bin unfolding explained earlier and the corresponding MC distribution on particle level. In addition, three systematic uncertainties on the unfolding as well as the statistical uncertainty from the data distribution propagated through the unfolding are shown in figure 5.3 (b,c). This analysis considers the limited MC statistics used for the unfolding inputs, a potential mis-modeling on the MC particle level and the cross section of the different MC simulation processes used to determine the SM prediction and build the response matrices as sources for systematic uncertainties. The first two uncertainties are determined as explained in section 4.5.4. The uncertainty coming from the MC cross sections is also obtained as discussed in section 4.5.4 with the addition that the procedure described in section 4.5.4 is done for every SM process considered in this analysis. One cross section of the MC processes is varied at a time by 10 % and the unfolding procedure is repeated. The quoted overall uncertainty is the square root of the quadratic sum of the uncertainties for the different processes.

Both unfolding methods show a good agreement with the particle level distribution and the result from bin-by-bin unfolding. The effect of two underfluctuations in the reconstructed data distributions in the two bins $950\,\text{GeV} < E_{\text{T}}^{\text{miss}} < 1000\,\text{GeV}$ and $1200\,\text{GeV} < E_{\text{T}}^{\text{miss}} < 1300\,\text{GeV}$ can be observed in the unfolded distributions, especially in the range $1200\,\text{GeV} < E_{\text{T}}^{\text{miss}} < 1300\,\text{GeV}$ where no event in data is observed. In the determination of the uncertainty from a potential mis-modeling on MC particle level, the reconstructed MC distribution is reweighted to data (compare section 4.5.4), where a relatively large weight occurs in the two bins where the underfluctation is observed. This results in a relatively large uncertainty from a potential MC mis-modeling for these two bins, as seen in figure 5.3 (b,d). However, the increased uncertainty in these bins is understood as a result of the underfluctation in data being the reason for the discrepancy between the data and the MC distribution in these bins. Neglecting these two small subregions of the missing transverse energy, the uncertainty from a mis-modeling is moderate, which validates the choice for the number of iterations in addition to the χ^2 test. The other uncertainties behave similar to what was observed in the study using MC and pseudo-data (see section 4.5.5), with the difference that the statistical power of the reconstructed data distribution is far worse compared to the reconstructed pseudo-data. From figure 5.3 (b,d) it can clearly be seen that the statistical uncertainty coming from the reconstructed data distribution is by far the dominant uncertainty. The uncertainty coming from the limited MC statistics is subdominant throughout the whole energy range. An uncertainty in the MC cross section is only of importance for the $Z \to \nu\nu$ unfolding at lower energies. Here, the influence of the conceptual difference of how this particular uncertainty affects the two unfolding methods becomes important again, as discussed earlier. The overall relative uncertainty is smaller in all but one bin for the topology unfolding method although one more iteration was used for this unfolding procedure compared to the $Z \to \nu\nu$ unfolding. The one bin ($1200\,\text{GeV} < E_{\text{T}}^{\text{miss}} < 1300\,\text{GeV}$) with a higher uncertainty for topology unfolding is due to the underfluctuation in data and has a larger effect because one more iteration was used for topology unfolding.

The unfolded event yield for the exclusive regions is shown in table 5.3 together with the relative uncertainties. These results will be used in section 5.4.3 to set limits on the ADD model. In every exclusive region of the missing energy distribution, the overall uncertainty is smaller for topology unfolding. The difference in the relative uncertainty ranges from approximately 300 % at low energy to 80 % at high energies with the statistical uncertainty from the data distribution and the systematic uncertainties from the MC cross sections being mostly responsible for the difference.

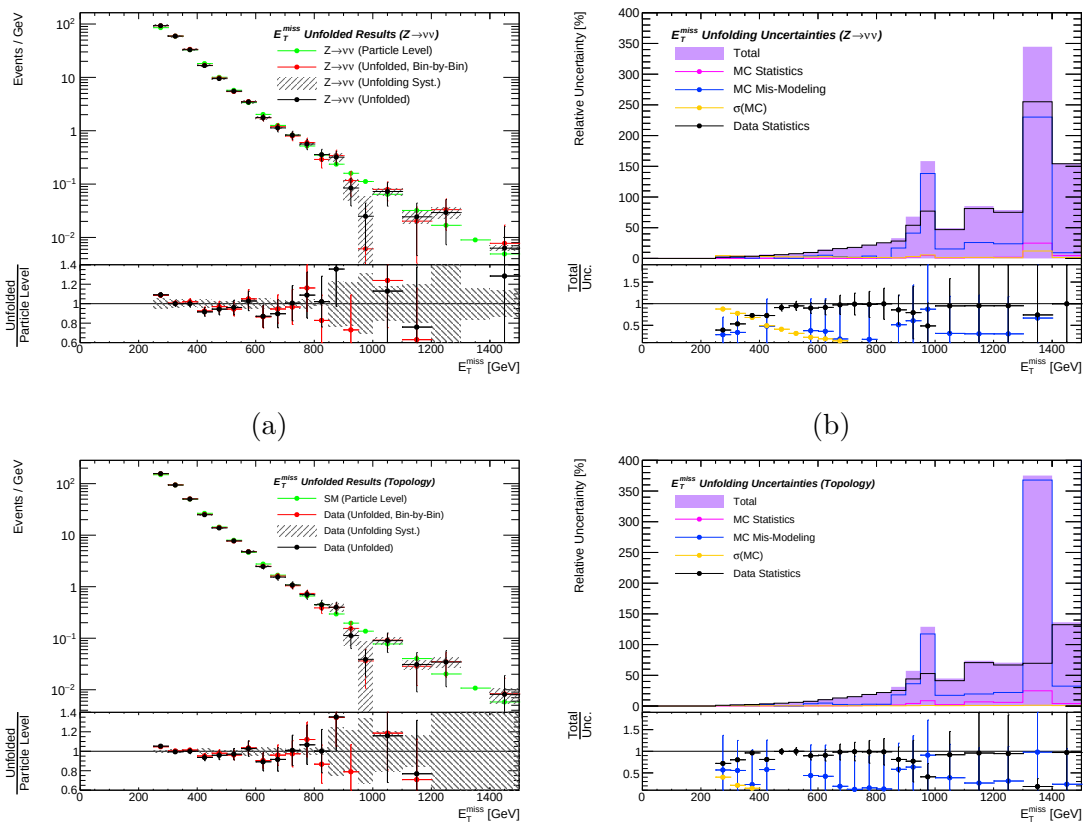

(a) (b)

(c) (d)

Figure 5.3.: The unfolded missing transverse energy distribution for $Z \to \nu\nu$ unfolding (a) using two iterations and topology unfolding (c) using three iterations. The corresponding systematic uncertainties and the statistical uncertainty are shown in (b) and (d) for $Z \to \nu\nu$ unfolding and topology unfolding.

Region $E_{\mathrm{T}}^{\mathrm{miss}}$ [GeV]	250 - 300	300 - 350	350 - 400
Topology Unfolding	7841 ± 130	4698 ± 108	2513 ± 65
σ(MC Statistics)	$< 0.1\,\%$	$< 0.1\,\%$	$<0.1\,\%$
σ(MC Mis-Modeling)	$0.9\,\%$	$1.3\,\%$	$0.6\,\%$
σ(MC Cross Section)	$0.7\,\%$	$0.5\,\%$	$0.4\,\%$
σ(Data Statistics)	$1.2\,\%$	$1.8\,\%$	$2.5\,\%$
σ(Total)	$1.7\,\%$	$2.3\,\%$	$2.6\,\%$
$Z \to \nu\nu$ Unfolding	4659 ± 247	2964 ± 151	1648 ± 80
σ(MC Statistics)	$< 0.1\,\%$	$< 0.1\,\%$	$< 0.1\,\%$
σ(MC Mis-Modeling)	$1.5\,\%$	$1.7\,\%$	$0.4\,\%$
σ(MC Cross Section)	$4.6\,\%$	$3.9\,\%$	$3.3\,\%$
σ(Data Statistics)	$2.1\,\%$	$2.7\,\%$	$3.5\,\%$
σ(Total)	$5.3\,\%$	$5.1\,\%$	$4.8\,\%$

Region $E_{\mathrm{T}}^{\mathrm{miss}}$ [GeV]	400 - 500	500 - 600	600 - 700	> 700
Topology Unfolding	1934 ± 85	626 ± 44	200 ± 24	156 ± 42
σ(MC Statistics)	$< 0.1\,\%$	$0.1\,\%$	$0.2\,\%$	$1.5\,\%$
σ(MC Mis-Modeling)	$1.6\,\%$	$1.4\,\%$	$3.9\,\%$	$9.2\,\%$
σ(MC Cross Section)	$0.4\,\%$	$0.3\,\%$	$0.3\,\%$	$0.5\,\%$
σ(Data Statistics)	$3.9\,\%$	$6.6\,\%$	$11.4\,\%$	$24.2\,\%$
σ(Total)	$4.4\,\%$	$7.0\,\%$	$12.1\,\%$	$27.2\,\%$
$Z \to \nu\nu$ Unfolding	1306 ± 87	449 ± 41	145 ± 22	122 ± 38
σ(MC Statistics)	$0.1\,\%$	$0.1\,\%$	$0.1\,\%$	$0.6\,\%$
σ(MC Mis-Modeling)	$2.2\,\%$	$1.6\,\%$	$4.4\,\%$	$8.9\,\%$
σ(MC Cross Section)	$3.1\,\%$	$2.5\,\%$	$2.6\,\%$	$1.6\,\%$
σ(Data Statistics)	$5.3\,\%$	$8.5\,\%$	$14.3\,\%$	$28.3\,\%$
σ(Total)	$6.7\,\%$	$9.1\,\%$	$15.3\,\%$	$30.8\,\%$

Table 5.3.: Unfolded event yield for exclusive missing transverse energy regions for topolgy unfolding and $Z \to \nu\nu$ unfolding together with the systematic and statistical uncertainties considered in the unfolding. The total uncertainty σ(Total) is the square root of the quadratic sum of the individual uncertainties.

5.4. Limit setting

5.4.1. Limit setting procedure

Search analyses observing no excess of events above the SM prediction are used to set exclusion limits on parameters of the given theory. These parameters could for example be the mass of a new particle or the modification of an expected cross section for a process of the given theory. This analysis uses the CL_s method [51] to set model independent limits on the visible cross section for new physics production as well as lower limits on the fundamental Planck scale for five different specification of the ADD model. The following section reviews the limit setting procedure.

In an analysis, the set of measurements carried out are denoted by

$$X = \{X_i\}. \tag{5.3}$$

In this analysis X_i corresponds to the number of events in a given energy i of the missing transverse energy distribution in the signal region. Next, a set of probability densities $g_i(X_i|\mu,\nu)$ is constructed for each observation X_i assuming an underlying theory with the parameters μ and ν. Here, μ, the so-called *parameter of interest*, is the fundamental parameter of the theory under study. In general, there can be more than one parameter of interest. Since this analysis uses a single parameter of interest for the limit setting procedure, the following discusses the case for one parameter of interest. The parameters $\nu = \{\nu_i\}$ are the *nuisance parameters*. These are parameters that are not under investigation in the analysis but that still have an influence on the prediction of a given theory, like the luminosity of the dataset used in the analysis. Nuisance parameters are usually derived from an independent measurement or physical assumptions. Since this analysis selects and counts events in different energy regions of a rather extreme phase space, the probability of an event to pass these selection is very small compared to the total cross-section of any scattering event happening. Therefore, $g(X_i|\mu,\nu)$ is chosen to be a Poisson distribution

$$g_i(X_i|\mu,\nu) = \frac{\lambda_i^{X_i} \mathrm{e}^{-\lambda_i}}{X_i!}, \tag{5.4}$$

where $\lambda_i = \lambda_i(\mu,\nu)$ is the expectation value of the prediction that a given theory makes. In this analysis, the prediction corresponds to the number of events that the SM predicts in the energy range i of the missing transverse energy distribution plus additional contributions from e.g. the ADD model. A distribution is suitable to test a theory if the additional contribution of that theory is sufficiently large compared to the SM prediction. In order to calculate the prediction of a theory $\lambda = \{\lambda_i(\mu,\nu)\}$ the nuisance parameters ν have to be fixed to certain values $\tilde{\nu}$. Therefore, the likelihood used for the CL_s method is chosen to be the product of the likelihood to observe the measured number of events X_i and the likelihood to observe the nuisance parameter values $\tilde{\nu}$, that where used to calculate the prediction, in an independent analysis

$$\begin{aligned}\mathcal{L} &= \prod_i g_i(X_i|\mu,\tilde{\nu}) \prod_j h_j(\tilde{\nu}_j|\nu_j) \\ &= \prod_i \frac{\tilde{\lambda}_i^{X_i} \mathrm{e}^{-\tilde{\lambda}_i}}{X_i!} \prod_j h_j(\tilde{\nu}_j|\nu_j).\end{aligned} \tag{5.5}$$

Here, the index i runs over all regions of the phase space that are considered in the limit setting procedure and the index j runs over all nuisance parameters. For those

nuisance parameters whose values are obtained from an independent experiment, like for example the luminosity, it is possible to argue how the underlying probability density h_j should look like based on the nature of the underlying experiment. However, for nuisance parameters that are not obtained from an underlying experiment a conceptional problem arises at this point, since it is not clear what probability density is suitable for these kind of nuisance parameters. In ATLAS, the usual policy is to use Gaussian probability densities for all nuisance parameters. However, it can be argued that this might not be the ideal choice in some cases. How the Likelihood looks and which nuisance parameters are considered in this analysis, will be explained in the sections that present the results of the limit setting. This section concentrates on the general procedure of the CL_s method.

In this method, the agreement of the observation X with a theoretical model providing the prediction $\lambda(\mu, \nu)$ is evaluated relative to the agreement of the observation with a second theoretical model $\lambda(\mu', \nu')$. The term *test-statistic* refers to a measure that quantifies the agreement of a theoretical prediction with an observation relative to the agreement of a second prediction with the observed data. In this analysis, the so-called *profiled log-likelihood ratio* $q_\mu(X)$ is used as the test-statistic, defined as

$$q_\mu(X) = \begin{cases} -2 \ln \frac{\mathcal{L}(X|\mu, \hat{\nu}_\mu)}{\mathcal{L}(X|\mu', \hat{\nu}_{\mu'})} & , \mu \geq \mu' \geq 0 \\ 0 & , \text{else} \end{cases} \qquad \geq 0. \tag{5.6}$$

The values of the nuisance parameters $\hat{\nu}_\mu$ are obtained from a constrained likelihood fit of the prediction to the observation for a given μ, so that

$$\mathcal{L}(X|\mu, \hat{\nu}_\mu) \geq \mathcal{L}(X|\mu, \nu) \qquad \forall \nu \tag{5.7}$$

and the likelihood of the observation is maximized. The parameters μ' and $\hat{\nu}_{\mu'}$ are obtained from an unconstrained likelihood fit, so that

$$\mathcal{L}(X|\mu', \hat{\nu}_{\mu'}) \geq \mathcal{L}(X|\mu, \nu) \qquad \forall \mu, \nu. \tag{5.8}$$

These values of the parameters correspond therefore to the global maximum of $\mathcal{L}$. The constraint of $\mu' \geq 0$ comes from the implication that only positive values for μ should be allowed, since μ corresponds in this analysis to the modification of a cross section which is defined to be non negative. The constrain of the test-statistic being zero for $\mu < \mu'$ gives rise to the fact that this analysis aims at setting one-sided limits in the sense of upper limits on the modification μ of a cross section describing a process arising from a theory beyond the SM. The *larger* the value of q_μ is, the *more disagrees* the observation X with the prediction $\lambda(\mu, \hat{\nu}_\mu)$ compared to the prediction $\lambda(\mu', \hat{\nu}_{\mu'})$. The here presented choice for the test-statistic follows the usual procedure used by the ATLAS collaboration [52].

Since the observation X corresponds to counting number of events in a specific phase space region, it is of a statistical nature meaning that a second independent measurement might observe a different number of events. Therefore, also the test-statistic $q_\mu(X)$ is affected by statistical fluctuations. The distribution $f(q_\mu|\mu, \hat{\nu}_\mu)$ of $q_\mu(X)$ assuming that the prediction $\lambda(\mu, \hat{\nu}_\mu)$ of a theory describes the expectation value of the observation cannot be evaluated analytically. In practice, two different ways exists how the distribution $f(q_\mu|\mu, \hat{\nu}_\mu)$ can be obtained.

1. The profiled log-likelihood ratio $q_\mu(X)$ is calculated for a large number of simulated toy measurements. Here, a replica of the measurement X^R is generated by drawing random numbers for each phase space region from a Poisson distribution around

the expectation $\lambda(\mu, \hat{\nu}_\mu)$. The values of all nuisance parameters are obtained from a constrained fit for a fixed value of μ, as explained above. In addition, a replica for each nuisance parameter $\hat{\nu}^R$ is created as well. To obtain these replica random numbers are drawn from the corresponding distribution of $h(\hat{\nu}|\hat{\nu}^R_\mu)$. Then, the test-statistic is computed for the replicas X^R and $\hat{\nu}^R$ in the same way as for X and ν. The procedure is repeated in order to obtain the distribution $f(q_\mu|\mu, \hat{\nu}_\mu)$. The disadvantage of this method is that the number of iterations for a sufficient precision and the computing time can be quite large, depending on the complexity of $\mathcal{L}$.

2. The second possibility is to use an analytical approximation for the distribution $f(q_\mu|\mu, \hat{\nu}_\mu)$. In [53] it is shown that $f(q_\mu|\mu, \hat{\nu}_\mu)$ follows a non central chi-square distribution for a sufficiently large sample size. Starting point of this approximation is

$$q_\mu = \frac{(\mu - \hat{\mu})^2}{\sigma^2} + \mathcal{O}(1/\sqrt{N}) \qquad \text{for } \mu \geq \mu' \geq 0, \tag{5.9}$$

where $\hat{\mu}$ is Gaussian distributed around the true value μ', according to which the data is assumed to be distributed, with a standard deviation σ [54]. The standard deviation σ can be estimated with the help of an artificial data set, called Asimov data set. This data set is defined as having infinite statistics and yielding the true value when it is used to evaluate an observable. True is understood with respect to the assumption that is made. In other words, the Asimov data set is the data set in which all observed quantities are set equal to their expected values. It is shown in [53] that the standard deviation σ can be obtained by

$$\sigma^2 = \frac{(\mu - \mu')^2}{q_\mu(X^A)}, \tag{5.10}$$

where $q_\mu(X^A)$ is the test-statistic for the Asimov data set X^A. The Asimov data set can be evaluated either by calculating the expected values of the hypothesis exactly or by using a MC simulation of the prediction. If the $\mathcal{O}(1/\sqrt{N})$ term can be ignored in equation (5.9) the test-statistic follows the non-central chi-square distribution

$$f(q_\mu|\mu, \hat{\nu}_\mu) = \frac{1}{2\sqrt{2\pi q_\mu}} \left(\mathrm{e}^{-\frac{1}{2}(\sqrt{q_\mu}+\sqrt{\Lambda})^2} + \mathrm{e}^{-\frac{1}{2}(\sqrt{q_\mu}-\sqrt{\Lambda})^2} \right) \tag{5.11}$$

with the non-centrality parameter Λ

$$\Lambda = \frac{(\mu - \mu')^2}{\sigma^2}. \tag{5.12}$$

In the absence of a signal contribution to the event yield, one has $\mu' = 0$, which corresponds to the background only hypothesis. The more signal, the larger μ, the smaller gets the non-centrality parameter and so the maximum of $f(q_\mu|\mu, \hat{\nu}_\mu)$ shifts towards zero.

The big advantage of using this approximation is a much smaller computing time needed to calculate the limits compared to the first approach. Inside ATLAS, it is recommended to use this approximation only if there are at least $\mathcal{O}(30)$ background events in the phase space region. For the selection of this analysis this requirement is fulfilled for all phase space regions.

So far, the outcome $X = \{X^i\}$ of a measurement was used to calculate the test-statistic $q_\mu(X)$ and the distribution $f(q_\mu|\mu, \hat{\nu}_\mu)$ of the test-statistic was obtained with the help of toy measurements or an analytical approximation.

$$X = \{X^i\} \xrightarrow{calculate} q_\mu(X) \xrightarrow[simulate]{approximate} f(q_\mu|\mu, \hat{\nu}_\mu)$$

The CL_s approach of testing a hypothesis is to compare the p-values of two different models with different predictions. In this analysis the hypothesis of new physics beyond the SM ($\mu > 0$) is compared to the so-called *background-only* hypothesis. This hypothesis predicts only events coming from SM processes and no additional signal contribution ($\mu = 0$). The aim is to set an upper limit on the modification μ of the cross section for a process beyond the SM predicted by the first hypothesis. First, the two distributions $f(q_\mu|\mu, \hat{\nu}_\mu)$ and $f(q_\mu|0, \hat{\nu}_0)$ are obtained from using toy measurements or the analytical approximation. The two p-values that are compared with each other are $CL_{S+B}(\mu)$ and $1 - CL_B(\mu)$. The first p-value

$$CL_{S+B}(\mu) = P(q_\mu(X') \geq q_\mu(X)|S + B) = \int_{q_\mu(X)}^{\infty} f(q_\mu|\mu, \hat{\nu}_\mu)\mathrm{d}q_\mu \tag{5.13}$$

is the probability of making a second observation X' with $q_\mu(X') \geq q_\mu(X)$ assuming that the prediction $\lambda(\mu, \hat{\nu}_\mu)$ describes correctly the outcome of the measurement. A large value of $CL_{S+B}(\mu)$ suggests that the observation X is compatible with the theory that is tested. The $CL_{S+B}(\mu)$ is compared to a second p-value

$$1 - CL_B(\mu) = P(q_\mu(X') \geq q_\mu(X)|B) = \int_{q_\mu(X)}^{\infty} f(q_\mu|0, \hat{\nu}_0)\mathrm{d}q_\mu, \tag{5.14}$$

which gives the probability to observe a second measurement X' with $q_\mu(X') \geq q_\mu(X)$ assuming that the background-only hypothesis describes the data. Large values of the $1 - CL_B(\mu)$ quantity indicate a *disagreement* of the observation X with the background-only hypothesis $\lambda(0, \hat{\nu}_\mu)$. The ratio of these two p-values, referred to as CL_s value,

$$CL_s = \frac{CL_{S+B}(\mu)}{1 - CL_B(\mu)} \tag{5.15}$$

is the measure that is used to judge if a certain value for μ of the given theory can be excluded or not. *Small* CL_s values suggest that the observation X *favors* the prediction of the background-only hypothesis compared to the prediction from the new physics model $\lambda(\mu, \hat{\nu}_\mu)$, suggesting an exclusion of this theory for physics beyond the SM. The devision by $1 - CL_B(\mu)$ prevents the analyzer from excluding models to which the analysis is not sensitive to. This can be understood with the help of figure 5.4 showing illustrations for the two distributions $f(q_\mu|0, \hat{\nu}_0)$ and $f(q_\mu|0, \hat{\nu}_0)$ for three different cases. They represent different specifications of a non-central chi-square distribution, where the non-centrality parameter is always larger for the background only hypothesis ($\mu' = 0$) according to equation (5.12). The three scenarios represent typical situations encountered during the limit setting when the parameter space of μ is scanned. For small values of μ, the additional signal contribution from a theory describing new physics is small and cannot be statistically distinguished from the background only hypothesis. Therefore, this value of μ cannot be excluded. This scenario is shown in figure 5.4 (a). The two distributions $f(q_\mu|0, \hat{\nu}_0)$ and $f(q_\mu|\mu, \hat{\nu}_\mu)$ show a relatively large overlap and the CL_{S+B} value (green)

is large and compatible with the $1 - CL_B$ (yellow) value. This results in a moderate CL_s value being larger than the exclusion threshold. The scenario (b) shows a case where a clear exclusion can be made. The observation is located at the tail of $f(q_\mu|\mu, \hat{\nu}_\mu)$ yielding a very small value of CL_{S+B} value and a moderate value of $1 - CL_B$. This combination drives the CL_s value down and the particular value of μ can be excluded. For the scenarios (a) and (b), it would in principle be sufficient to evaluated only the CL_{S+B}, where large values (a) indicate that the theory is compatible with the observation and small values (b) recommend an exclusion. The last scenario (c) shows why it makes sense to base the exclusion on the CL_s value. In this scenario the two distributions of the test statistics are quite compatible at the upper end of the distributions. The observed value of the profiled log-likelihood ratio is located in the tail of the distributions. This results in a very small CL_{S+B} value and the model might be exclude by a limit setting procedure based on only the CL_{S+B} value. However, the $1 - CL_B(\mu)$ is very small as well. An observation so far out on the tail of the background only distribution is highly unlikely assuming that the background only assumption describes the data. This might indicate a general problem in the analysis or be the result of a large underfluctuation in the data. Since the CL_{S+B} and $1 - CL_B(\mu)$ value are both small but compatible the CL_s value is located close to one preventing an exclusion of the theory. In this sense, the CL_s method is conservative but presents a good handling of the exclusion because the fact that the two distributions show a large overlap really means that the analysis might not be sensitive to the specific model and an unlikely small value of $1 - CL_B(\mu)$ might result from a problem in the analysis. After calculating the CL_s values for many values of the parameter of interest μ, the upper limit can be identified. Values of $\tilde{\mu}$ are excluded if

$$CL_s(\tilde{\mu}) < \alpha, \tag{5.16}$$

where α is for a 95 % CL_s confidence level equal to $1 - 0.95 = 0.05$. The upper limit μ_{up} corresponds to the smallest value of μ for which this condition is fulfilled.

The observed upper limit is usually quoted with an *expected* limit. The expected limit is used to characterize the sensitivity of an analysis while several definitions of an expected limit exist. This analysis replaces the observed value of the test statistic $q_\mu(X)$ by the median of the background only distribution $f(q_\mu|0, \hat{\nu}_0)$ and recalculates the upper limit, which is interpreted as the expected limit. To obtain uncertainty bands the observed value of the test statistic is replaced by the median of the background only distribution plus or minus one or two standard deviations.

5.4.2. Model-independent limits

In order to validate the limit setting procedure and the construction of the likelihood the results on reconstruction level (section 5.2.1) are used to set model-independent upper limits on the visible cross section σ_{vis} for new physics phenomena entering the considered phase space of the analysis. The visible cross section can be understood as the product of the cross section of the new process times the acceptance and the efficiency $\sigma_{\text{vis}} = \sigma \cdot A \cdot \epsilon$. The following likelihood function $\mathcal{L}_i$ will be used to set a separate upper limit for each inclusive region i, as defined in table 5.1,

$$\mathcal{L}_i = \mathcal{P}\left(N^i_{\text{obs}} | \underbrace{\sigma^i_{\text{vis}} \cdot L \cdot \left(\frac{\sigma(L)}{L} + 1 \right)^{\theta^i_L}}_{\text{signal}} + \underbrace{N^i_b \cdot \left(\frac{\sigma(N^i_b)}{N^i_b} + 1 \right)^{\theta^i_b}}_{\text{background}} \right) \cdot \mathcal{G}(0|\theta^i_L, 1) \cdot \mathcal{G}(0|\theta^i_b, 1),$$

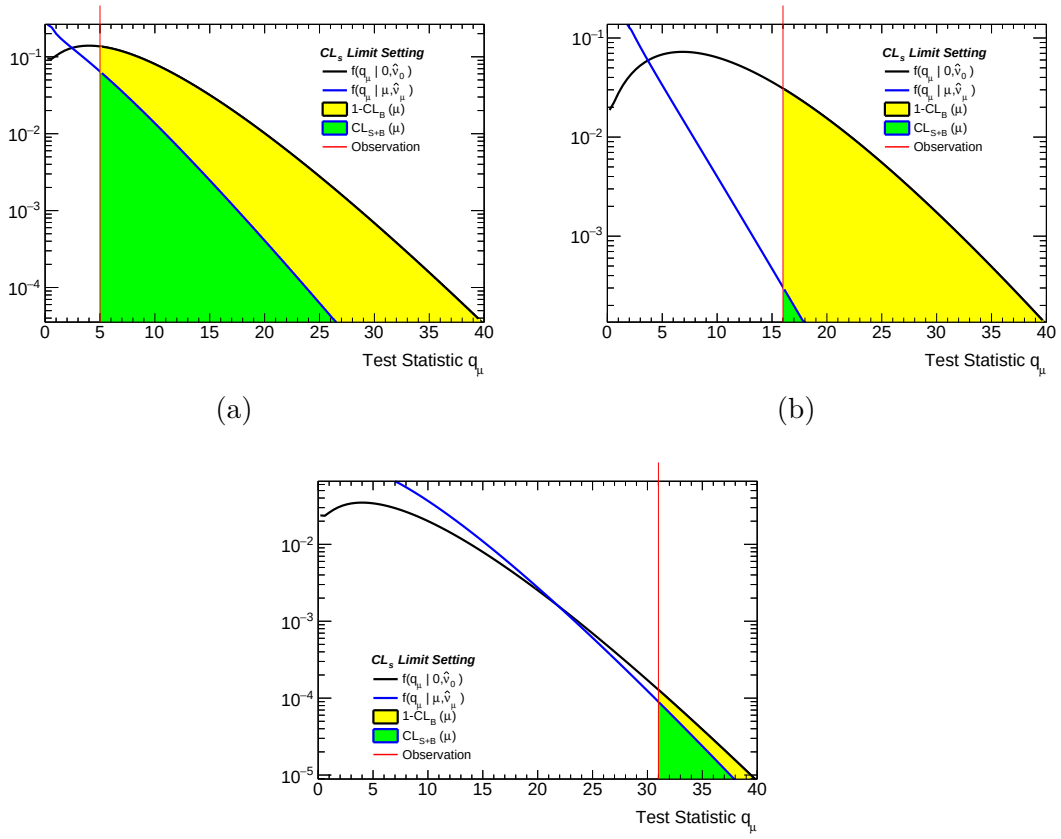

Figure 5.4.: Visualizations of the non-central chi-squared distributions of the test statistics for the background only hypothesis (black) and a signal hypothesis (blue). The vertical red lines show the observed value of the test statistic and the green area indicates CL_{S+B}, the yellow area $1-CL_B$. Three typical scenarios are show: (a) a parameter of interest value that cannot be excluded, (b) a value that can be excluded and (c) a parameter of interest value that will not be not excluded by the CL_s method but might be excluded by other limit setting procedures.

(5.17)

where

- N^i_{obs} is the number of observed events in the region i (given in table 5.1),
- σ^i_{vis} is the visible cross section in the region i and the parameter of interest,
- L is the luminosity,
- $\sigma(L)$ is the uncertainty of the luminosity, assumed to be 5 %,
- N^i_b is the number of events predicted by the SM in region i (given in table 5.1),
- $\sigma(N^i_b)$ is the overall statistical and systematic uncertainty on N^i_b (given in table 5.1),
- θ^i_L and θ^i_b the nuisance parameters for L and N^i_b.

$\mathcal{P}$ stands for a Poisson distribution and $\mathcal{G}$ for a Gaussian. As discussed in the previous section, the underlying probability density of the measurement is a Poisson distribution. It is evaluated at N_{obs} and has a mean of $N_{\text{signal}} + N_{\text{background}}$. The two nuisance parameters of the luminosity and the background uncertainty are chosen to follow a Gaussian distribution. The response function for these two nuisance parameters is chosen to be the so-called log-normal response $R(\theta) = (\sigma(N)/N + 1)^\theta$, which is discussed in more detail in appendix B.1.

Figure 5.5 (a) shows the observed upper limits on the visible cross section for all seven inclusive regions obtained from the CL_s method at a 95 % confidence level using the analytical approximation for the test statistic distribution. In addition, the expected limits and the limits from the published monojet analysis [41] are shown as well. The limits obtained by this analysis are compatible with the ones from [41]. The small differences that are observed between the limits come mainly from the fact that [41] includes several control regions in the likelihood and the limit setting procedure, which makes the limits in general more reliable, whereas this analysis uses for simplicity only the signal region for the limit setting. Nevertheless, the limits obtained in this analysis are very similar, which validates the presented limit setting procedure. Figure 5.5 (b) shows an example for the different CL_s values obtained from the parameter scan of the parameter of interest σ_{vis} for the inclusive region $E^{\text{miss}}_{\text{T}} > 300\,\text{GeV}$. The smaller the visible cross section the less events are produced in the signal region. Small values of σ_{vis} can statistically not be distinguished from the background only hypothesis and are therefore not excluded. The red horizontal line represents the 0.05 threshold of the CL_s value at a 95 % confidence interval. All visible cross sections with a CL_s value below that line are excluded. For the inclusive region shown in figure 5.5 (b) this is the case for $\sigma_{\text{vis}} \gtrapprox 300\,\text{fb}$. The observed limit is slightly better than the expected limit because in this inclusive region of the missing transverse energy slightly less events are observed in data than predicted by the SM expectation.

5.4.3. Limits on the fundamental Planck scale in the ADD model

This section presents the results of the limit setting on the ADD model. First, the limit setting procedure described in section 5.4.1 is performed at reconstruction level. This allows a comparison with the results from [41] and to the later on discussed limits obtained on particle level after the unfolding.

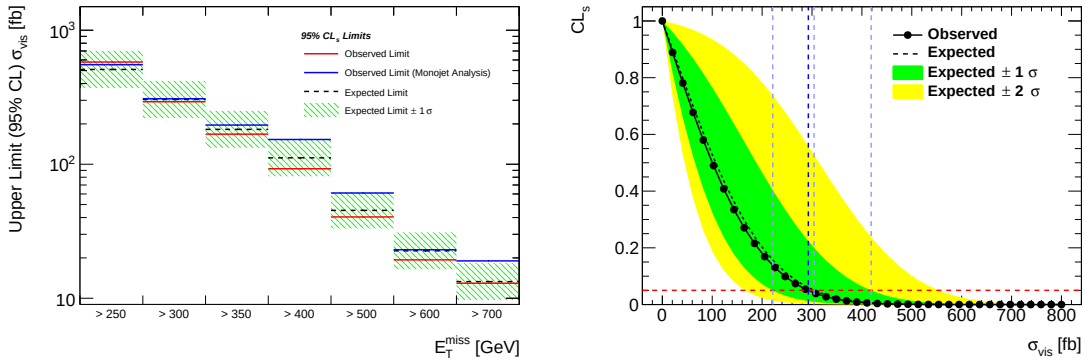

(a) (b)

Figure 5.5.: Reconstruction level limits on the visible cross section for seven inclusive $E_{\mathrm{T}}^{\mathrm{miss}}$ regions (a): observed (red) and expected (black) limits as well as the $\pm 1\sigma$ interval around the expected limit (green) from this analysis, observed limits from [41] (blue). The observed and expected CL_s values as a function of the parameter of interetest σ_{vis} are shown in (b) for $E_{\mathrm{T}}^{\mathrm{miss}} > 300\,\mathrm{GeV}$. The vertical blue line indicates the observed limit, the vertical light blue lines the expected limits and the $\pm 1\sigma$ interval.

5.4.4. Limits at reconstruction level

Figure 5.9 shows the missing transverse energy and the transverse momentum distribution of the leading jet at reconstruction level for the observed data, the SM prediction and five different specifications of the ADD model with the difference being the number of extra dimensions ranging from two to six, the fundamental Planck scale and the mass of the graviton. More details on the ADD models used in the analysis are presented in appendix B.4. As can be seen in Figure 5.9 the ADD models predict a significant amount of events at higher energies in addition to the SM prediction demonstrating the sensitivity of these two distributions to the ADD models. The transverse momentum distribution of the leading jet is in addition to the $E_{\mathrm{T}}^{\mathrm{miss}}$ distribution sensitive to these new physics models because the leading jet recoils against the missing transverse energy for Z and W boson production in association with one jet and also for hypothetical final states involving a graviton and a quark or gluon. This analysis follows the approach of [41] to use the missing transverse energy distribution from $E_{\mathrm{T}}^{\mathrm{miss}} = 400\,\mathrm{GeV}$ up to higher energies for the limit setting. The missing transverse energy distribution is divided from this energy upwards into exclusive regions as defined in table 5.2. In each of these regions a counting experiment is performed comparing the observed to the expected event yield. The expectation includes the SM prediction for the background only hypothesis and in addition the contribution from the ADD model for the signal hypothesis. Dividing the missing transverse energy in several exclusive regions means that the shape information of the distribution is used in the limit setting. At reconstruction level, the following

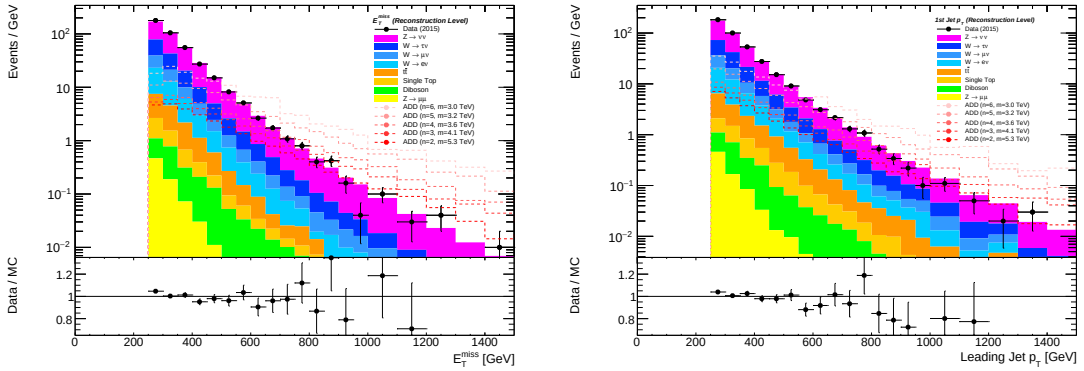

(a) (b)

Figure 5.6.: Missing transverse energy (a) and the transverse momentum distribution of the leading jet (b) at reconstruction level for data (black), the SM prediction (colored) and five different specification of the ADD model (red, dashed).

likelihood function is used,

$$
\begin{aligned}
\mathcal{L} = \prod_{i=1}^{4} \mathcal{P}_i \Bigg[N^i_{\text{obs}} \Big| \mu \cdot \sigma_{\text{ADD}} \cdot \left(\frac{\sigma(\sigma^i_{\text{ADD,Jet/E}_\text{T}^\text{miss}})}{\sigma_{\text{ADD}}} + 1 \right)^{\theta_{\sigma_{\text{ADD}},\text{Jet/E}_\text{T}^\text{miss}}} \\
\cdot \left(\frac{\sigma(\sigma^i_{\text{ADD,PDF}})}{\sigma_{\text{ADD}}} + 1 \right)^{\theta_{\sigma_{\text{ADD}},\text{PDF}}} \cdot \left(\frac{\sigma(\sigma^i_{\text{ADD,Ren/Fac}})}{\sigma_{\text{ADD}}} + 1 \right)^{\theta_{\sigma_{\text{ADD}},\text{Ren/Fac}}} \\
\cdot \epsilon^i_{\text{ADD}} \cdot \left(\frac{\sigma(\epsilon^i_{\text{ADD}})}{\epsilon^i_{\text{ADD}}} + 1 \right)^{\theta^i_{\epsilon_{\text{ADD}}}} \cdot A^i_{\text{ADD}} \cdot \left(\frac{\sigma(A^i_{\text{ADD,Ini/Fin}})}{A_{\text{ADD}}} + 1 \right)^{\theta_{A_{\text{ADD}},\text{Ini/Fin}}} \\
\cdot \left(\frac{\sigma(A^i_{\text{ADD,PDF}})}{A_{\text{ADD}}} + 1 \right)^{\theta_{A_{\text{ADD}},\text{PDF}}} \cdot \left(\frac{\sigma(A^i_{\text{ADD,Ren/Fac}})}{A_{\text{ADD}}} + 1 \right)^{\theta_{A_{\text{ADD}},\text{Ren/Fac}}} \\
\cdot \epsilon^i_{\text{filter}} \cdot L \cdot \left(\frac{\sigma(L)}{L} + 1 \right)^{\theta_L} + N_b \cdot \left(\frac{\sigma(N^i_b)}{N^i_b} + 1 \right)^{\theta_b} \Bigg] \\
\cdot \mathcal{G}(0|\theta_{\sigma_{\text{ADD}},\text{Jet/E}}, 1) \cdot \mathcal{G}(0|\theta_{\sigma_{\text{ADD}},\text{PDF}}, 1) \cdot \mathcal{G}(0|\theta_{\sigma_{\text{ADD}},\text{Ren/Fac}}, 1) \\
\cdot \mathcal{G}(0|\theta_{A_{\text{ADD}},\text{Ini/Fin}}, 1) \cdot \mathcal{G}(0|\theta_{A_{\text{ADD}},\text{PDF}}, 1) \cdot \mathcal{G}(0|\theta_{A_{\text{ADD}},\text{Ren/Fac}}, 1) \\
\cdot \mathcal{G}(0|\theta_L, 1) \cdot \mathcal{G}(0|\theta_b, 1) \cdot \mathcal{G}_i(0|\theta^i_{\epsilon_{\text{ADD}}}, 1)
\end{aligned}
\tag{5.18}
$$

where i runs over the four exclusive region of the E_T^miss distribution and in addition to the variables μ, L, $\sigma(L)$, N^i_{obs}, N_b, $\sigma(N^i_b)$ (explained in the previous section) the following variables where used:

- σ_{ADD}: cross section of the ADD model with uncertainties $\sigma(\sigma^i_{\text{ADD,Jet/E}_\text{T}^\text{miss}})$, $\sigma(\sigma^i_{\text{ADD,PDF}})$ and $\sigma(\sigma^i_{\text{ADD,Ren/Fac}})$ coming from jet energy and missing transverse energy scale, the parton density function (PDF) and the renormalization and factorization scale
- $\epsilon^i_{ADD} = N(\text{reco})^i / N(\text{particle})^i$: signal efficiency, defined as the number of events passing the reconstruction level selection divided by the number of events passing the particle level requirements in region i with a statistical uncertainty $\sigma(\epsilon^i_{\text{ADD}})$,

- $A^i_{\mathrm{ADD}} = N(\mathrm{particle})^i / N(\mathrm{generated})^i$: acceptance defined as the number of events passing the particle level selection divided by the overall generated number of events in region i with uncertainties $\sigma(A^i_{\mathrm{ADD,Ini/Fin}})$, $\sigma(A^i_{\mathrm{ADD,PDF}})$ and $\sigma(A^i_{\mathrm{ADD,Ren/Fac}})$ coming from the modeling of the initial and final state radiation, the PDF as well as the renormalization and factorization scale.

- $\epsilon^i_{\mathrm{filter}}$: filter efficiency.

The luminosity uncertainty is assumed again to be 5 %. The statistical and systematic uncertainty on the background prediction are taken from table 5.2. The uncertainties on the cross section and the signal acceptance are taken from [41] and are summarized in appendix B.4. The cross section uncertainty coming from the PDF ranges from 16 % for the ADD model specification with two extra dimensions up to 42 % for six extra dimensions, the uncertainty from the renormalization and factorization scale from 23 % to 36 %. The uncertainty from the jet energy and the missing transverse energy scale is 3 % for all specifications of the ADD model. The uncertainty on the acceptance is dominated by the PDF uncertainty, ranging from 10 % up to 20 % and the uncertainties from the initial and final state modeling and the renormalization and factorization scale are estimated to be 10 %. To every uncertainties a nuisance parameter θ_x is assigned in the likelihood. The nuisance parameters of the signal efficiency $\theta^i_{\epsilon_{\mathrm{ADD}}}$ are uncorrelated because the statistical uncertainty in one exclusive region is independent from the statistical uncertainty in the other regions. Therefore, each region has one independent nuisance parameter. The individual cross section and acceptance uncertainties are fully correlated among the different exclusive $E_{\mathrm{T}}^{\mathrm{miss}}$ regions. That is the reason why there is only one nuisance parameter for all regions per uncertainty. Also the overall background uncertainty is assumed to be fully correlated throughout the exclusive regions and only one nuisance parameter θ_b is introduced. That simplification is due to the fact that the real correlation of the uncertainties is not published in [**2**]. The response function is chosen to be the log-normal response for every uncertainty and the distribution of the nuisance parameters is assumed to be Gaussian. For some uncertainties like the PDF uncertainty also other choice would be possible. The Gaussian choice is another simplification which does not affect the analysis too heavily. The definition of $\mathcal{L}$ and the simplification mentioned before are validates by reproducing the limits on detector level and comparing them to the results from [41].

The limit setting procedure is performed for each specification of the ADD model separately and one upper limit on the modification μ of the cross section that is assumed by the model is extracted. The results can be seen in figure 5.9 (a). The observed limits are compatible with the expected limits since no excess above the SM is observed. Figure 5.9 (b) shows one example for the CL_s value as a function of μ for the model with three extra dimension. The values of μ to the right of the vertical blue line are excluded because their CL_s values are below 5 % indicated by the red horizontal line. These upper limits on μ can be translated into lower limits of the fundamental Planck scale M_D in the ADD model. This is done by using the relation

$$\sigma_{\mathrm{ADD}} \propto \frac{1}{M_D^{n+2}}, \tag{5.19}$$

where n is the number of extra dimensions. For a given number of n and a given center of mass energy, the proportional constant is just a constant number A. Therefore the lower limit on the fundamental Planck Scale M_D^{lim} can be calculated from the upper limit

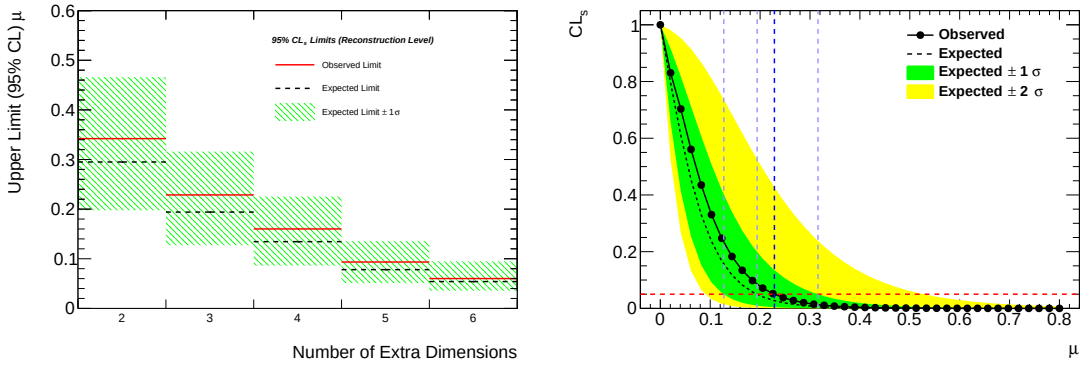

(a) (b)

Figure 5.7.: Observed (red) and expected (black) limits (a) obtained at reconstruction level with the $\pm 1\sigma$ interval on the modification μ of the cross section σ_{ADD}. (b) shows the CL_s value as a function of the parameter of interest μ for the ADD model with three extra dimensions. The blue vertical line indicates the observed limit on μ corresponding to the value smallest value of μ with $CL_s < 0.05$. The light blue vertical lines indicate the expected limit as well as the $\pm 1\sigma$ variations.

μ^{lim} as

$$M_D^{\mathrm{lim}} = \left(\frac{A}{\sigma_{\mathrm{ADD}} \cdot \mu^{\mathrm{lim}}} \right)^{\frac{1}{n+2}} . \tag{5.20}$$

The results for the lower limits on M_D are given in figure 5.8. These results can be compared to the limits quoted in [41] which are also shown in figure 5.8. Both sets of limits show a good agreement validating once again the limit setting procedure and the small impact of the simplification that have been made in this analysis.

5.4.5. Limits on particle level

The unfolded missing energy distribution is used to set lower limits on the fundamental Planck scale of the ADD model for $Z \to \nu\nu$ unfolding and topology unfolding. The results are compared to the limits obtained on particle level. The same likelihood function is used as in the previous chapter with some modifications. The signal efficiency is dropped since the prediction of the different specifications of the ADD model are used on particle level. The prediction of the SM contribution is also evaluated on particle level. The uncertainties on that prediction are assumed to be the same uncertainties at reconstruction level. In addition, the unfolding uncertainties as discussed in section 5.2.1 are included. In order to avoid a bias these uncertainties are associated to the background prediction and not to the observed number of events. This complication is briefly discussed in [55]. Taking

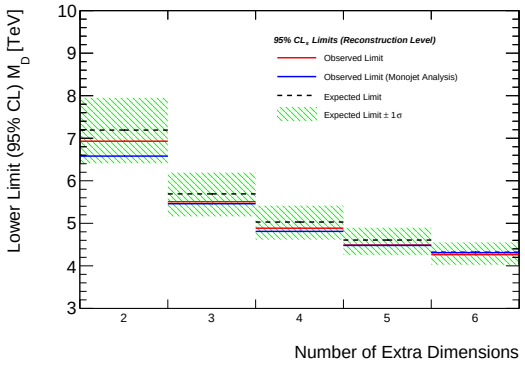

(a)

Figure 5.8.: Observed (red) and expected (black) limits (reconstruction level) with the $\pm 1\sigma$ interval as well as the observed limits from [41] on the fundamental Planck scale M_D for five different specifications of the ADD model predicting two to six large extra dimensions.

these modifications into account yields the following likelihood

$$
\begin{aligned}
\mathcal{L} = \prod_{i=1}^{4} \mathcal{P}_i \Bigg[N^i_{\text{obs}} \Big| \mu \cdot \sigma_{\text{ADD}} \cdot & \left(\frac{\sigma(\sigma^i_{\text{ADD,Jet/E}^{\text{miss}}_{\text{T}}})}{\sigma_{\text{ADD}}} + 1 \right)^{\theta_{\sigma_{\text{ADD}},\text{Jet/E}^{\text{miss}}_{\text{T}}}} \\
& \cdot \left(\frac{\sigma(\sigma^i_{\text{ADD,PDF}})}{\sigma_{\text{ADD}}} + 1 \right)^{\theta_{\sigma_{\text{ADD}},\text{PDF}}} \cdot \left(\frac{\sigma(\sigma^i_{\text{ADD,Ren/Fac}})}{\sigma_{\text{ADD}}} + 1 \right)^{\theta_{\sigma_{\text{ADD}},\text{Ren/Fac}}} \\
& \cdot A^i_{\text{ADD}} \cdot \left(\frac{\sigma(A^i_{\text{ADD,Ini/Fin}})}{A_{\text{ADD}}} + 1 \right)^{\theta_{A_{\text{ADD}},\text{Ini/Fin}}} \\
& \cdot \left(\frac{\sigma(A^i_{\text{ADD,PDF}})}{A_{\text{ADD}}} + 1 \right)^{\theta_{A_{\text{ADD}},\text{PDF}}} \cdot \left(\frac{\sigma(A^i_{\text{ADD,Ren/Fac}})}{A_{\text{ADD}}} + 1 \right)^{\theta_{A_{\text{ADD}},\text{Ren/Fac}}} \\
& \cdot \epsilon^i_{\text{filter}} \cdot L \cdot \left(\frac{\sigma(L)}{L} + 1 \right)^{\theta_L} + N_b \cdot \left(\frac{\sigma(N^i_b)}{N^i_b} + 1 \right)^{\theta_b} \\
& \cdot \left(\frac{\sigma(N^i_{b,\text{MC Stat}})}{N^i_b} + 1 \right)^{\theta_{b,\text{MC Stat}}} \cdot \left(\frac{\sigma(N^i_{b,\text{MC Mis-Mod}})}{N^i_b} + 1 \right)^{\theta_{b,\text{MC Mis-Mod}}} \\
& \cdot \left(\frac{\sigma(N^i_{b,\sigma(\text{MC})})}{N^i_b} + 1 \right)^{\theta_{b,\sigma(\text{MC})}} \Bigg] \\
& \cdot \mathcal{G}(0|\theta_{\sigma_{\text{ADD}},\text{Jet/E}},1) \cdot \mathcal{G}(0|\theta_{\sigma_{\text{ADD}},\text{PDF}},1) \cdot \mathcal{G}(0|\theta_{\sigma_{\text{ADD}},\text{Ren/Fac}},1) \\
& \cdot \mathcal{G}(0|\theta_{A_{\text{ADD}},\text{Ini/Fin}},1) \cdot \mathcal{G}(0|\theta_{A_{\text{ADD}},\text{PDF}},1) \cdot \mathcal{G}(0|\theta_{A_{\text{ADD}},\text{Ren/Fac}},1) \\
& \cdot \mathcal{G}(0|\theta_L,1) \cdot \mathcal{G}(0|\theta_b,1) \cdot \mathcal{G}(0|\theta_{b,\text{MC Stat}},1) \cdot \mathcal{G}(0|\theta_{b,\text{MC Mis-Mod}},1) \\
& \cdot \mathcal{G}(0|\theta_{b,\sigma(\text{MC})},1). \qquad (5.21)
\end{aligned}
$$

Figure 5.9 shows the obtained limits from the unfolded distribution on the fundamental Planck scale M_D for $Z \to \nu\nu$ unfolding and topology unfolding. Both unfolding methods result in a very similar limit. No significant difference can be observed although the $Z \to \nu\nu$ limit is constantly above the topology unfolding limit. This can be seen better in

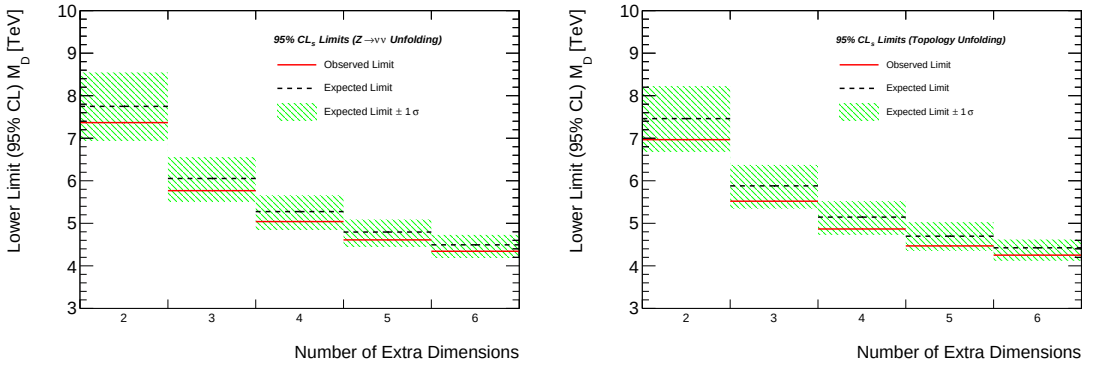

(a) (b)

Figure 5.9.: Observed (red) and expected (black, green) limits obtained from the unfolded missing transverse energy distribution on the fundamental Planck scale M_D in the ADD model for $Z \to \nu\nu$ unfolding (a,c) and topology unfolding (b,d).

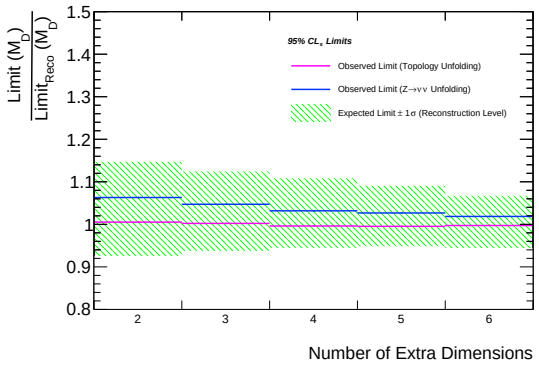

(a)

Figure 5.10.: The limits on the fundamental Planck scale from $Z \to \nu\nu$ (blue) and topology (magenta) unfolding divided by the limit obtained at reconstruction level. The green band indicates the $\pm 1\sigma$ interval of the expected limit at reconstruction level.

figure 5.10 which shows the ratio between the observed limit from the unfolding methods and the observed limit on detector level on M_D. Both ratios are very close to one and well within the $\pm 1\sigma$ interval of the expected limit at reconstruction level.

Therefore, it is shown that

---

limits obtained from unfolded distributions and limits obtained at reconstruction level are compatible. The results from topology unfolding agree well with results from the conventional way of unfolding.

The underlying assumption of this study is the fact that the relative uncertainties of the SM prediction at particle level are the same at reconstruction level. As explained earlier, some experimental and theoretical uncertainties at reconstruction level are reduced because the background estimation of [41] includes ratios of MC predictions. If the full

uncertainties at particle level were estimated instead of assuming the same uncertainties at reconstruction level, the uncertainties could become larger. However, the uncertainties can in principle also be derived from control regions including ratios canceling some fraction of the uncertainties. These control regions would then be unfolded control regions. This idea is not investigated in this analysis but might be subject of further studies.

The promising results obtained using the topology unfolding method clear the way for a second attractive possibility. A new concept could be developed which relies not on a background subtraction any longer, but only on topology unfolding. The selected data would be unfolded with the topology unfolding technique using MC simulations and directly compared to calculated cross sections or MC distributions on particle level. This analysis strategy involves two main advantages. First, the background estimation is no longer needed, which results in a massive shortening of the time scale of an analysis. Second, as mentioned earlier the treatment of theoretical and experimental uncertainties would follow a more natural way. Besides the unfolding uncertainties, the observation would be affected only by experimental uncertainties, because no MC simulations are used to subtract a background. In most analysis in which a background subtraction *is* performed a semi datadriven method is applied using at some point MC simulations. Therefore, the observed number of events are affected by theoretical uncertainties after the background subtraction. Furthermore, the expectation of the analysis using topology unfolding would be of a pure theoretical nature. This results in a clean separation of theoretical and experimental uncertainties.

6. Conclusion

This thesis presents a proof of concept analysis for a newly introduced unfolding method, topology unfolding. This method makes no distinction between signal and background processes and performs no background subtraction before the unfolding. Instead, the inclusive reconstructed data distribution is unfolded using MC simulations of all SM processes that pass the selection criteria. This approach follows the general idea of unfolding, namely to provide an unfolded data distribution which is as independent of other assumptions or measurements as possible. In the conventional way of unfolding, only one signal process is unfolded after a background subtraction is performed. The resulting distribution is independent of the detector, which offers several advantages like the possibility to use the provided data in future analysis or for comparisons with other experiments. A distribution unfolded with the topology unfolding technique is in addition to that also independent of the estimation of the SM processes because here no background subtraction is performed. This analysis shows in the context of a monojet search for new physics that the results obtained by topology unfolding are consistent with the results from the conventional way of unfolding. In addition, topology unfolding results in smaller uncertainties, mostly because the higher statistics of the inclusive reconstructed data distribution is used through this technique and the topology unfolding matrix is more stable against shifts in the normalization of the different SM processes than the background subtraction performed in the conventional unfolding method. Furthermore, it is shown that the unfolded results from the topology unfolding method and from the conventional unfolding technique can be used to set limits on models predicting physics beyond the standard model that are compatible with limits obtained at reconstruction level. This study is performed with the 2015 dataset provided by the LHC corresponding to an integrated luminosity of $3.2\,\mathrm{fb}^{-1}$ in the context of large extra dimensions and the ADD model probed by a monojet search. Limits are set on the fundamental Planck scale of five different specifications of the ADD model. The results are validated by a comparison to a recently published monojet search of the ATLAS collaboration. The general advantages of unfolding and the here presented proof that unfolded distributions result in the same limits as obtained at reconstruction level recommend that unfolding should be used commonly in searches for new physics. The topology unfolding offers additional advantages. This techniques results in smaller uncertainties, provides a more intuitive separation of theoretical and experimental uncertainties and could be used to design a new analysis concept in which the huge effort of estimating the SM contribution to an event selection could be omitted. The here presented study understands itself as a proof of concept analysis. The promising results of the new unfolding method offer the possibility of testing topology unfolding in an independent search for new physics in near future.

A. Topology unfolding

A.1. Resolution

Figure A.1 shows the resolution for the invariant mass of the two leading jets and the transverse momentum of the second leading jet. The procedure to obtain the resolution is described in section 4.3.

A.2. Efficiency, fake rate, purity and response matrix

For completeness of section 4.5.1, the response matrices of the transverse momentum of the second leading jet and the invariant mass of the two leading jets are shown in figure A.2.

A.3. Closure test

Figure A.3 shows further results of the closure test for $Z \to \nu\nu$ and topology unfolding in addition to the ones shown in section 4.5.2. Figure A.4 present the full results of the closure test from section 4.5.2 for unfolding the $W \to \tau\nu$ process.

A.4. Unfolded results

Figure A.5 and figure A.6 show the unfolded results from section 4.5.3 for the transverse momentum of the second leading jet and the invariant mass of the two leading jets, together with the corresponding correlation matrices for each unfolded distribution of the statstical uncertainties of the reconstructed distribution.

A.5. Comparison of uncertainties

Figure A.7 shows the relative fractions of different uncertainties as a function of the transverse momentum of the second leading jet and the invariant mass of the two leading jets as discussed in section 4.7. The full relative and the full systematic uncertainties for the transverse momentum of the second leading jet and the invariant mass of the two leading jets are shown in figure A.8 for both unfolding methods.

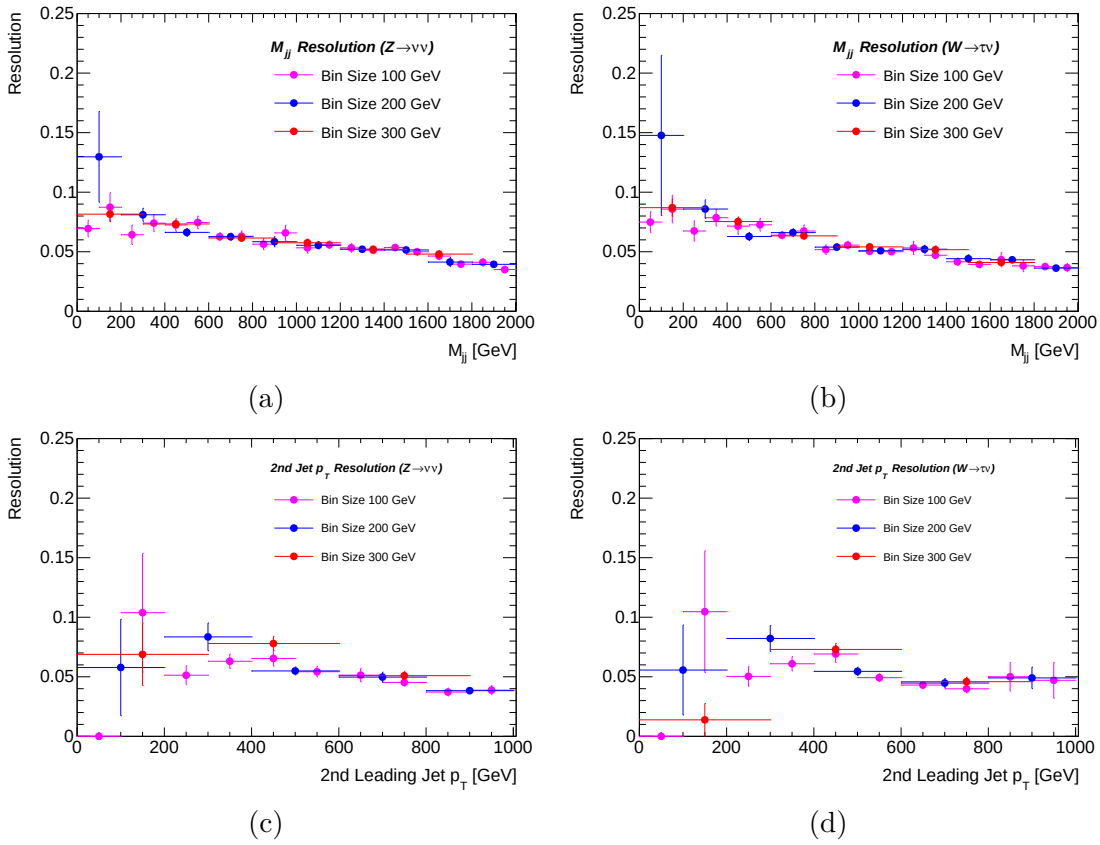

Figure A.1.: The resolution of the invariant mass of the two leading jets (a,b) and the transverse momentum of the second leading jet (c,d) for the $Z \to \nu\nu$ (a,c) and $W \to \tau\nu$ (b,d) simulation.

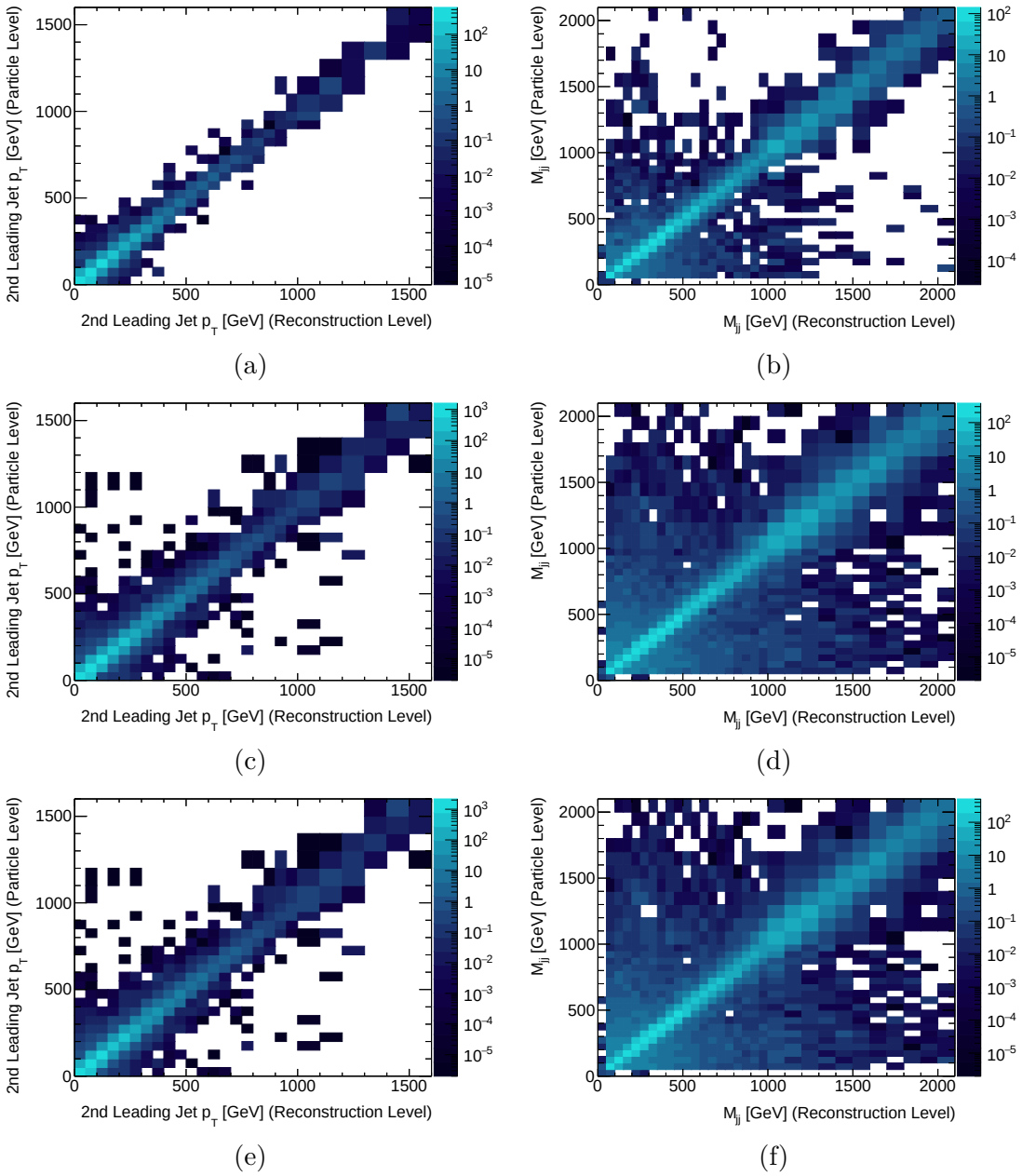

Figure A.2.: The response matrices for the transverse momentum of the second leading jet (a,c,e) and the invariant mass of the two leading jets (b,d,f) for the $W \to \tau\nu$ (a,b), the $Z \to \nu\nu$ process (c,d) and the sum of the two processes (e,f) as used for the topology unfolding method.

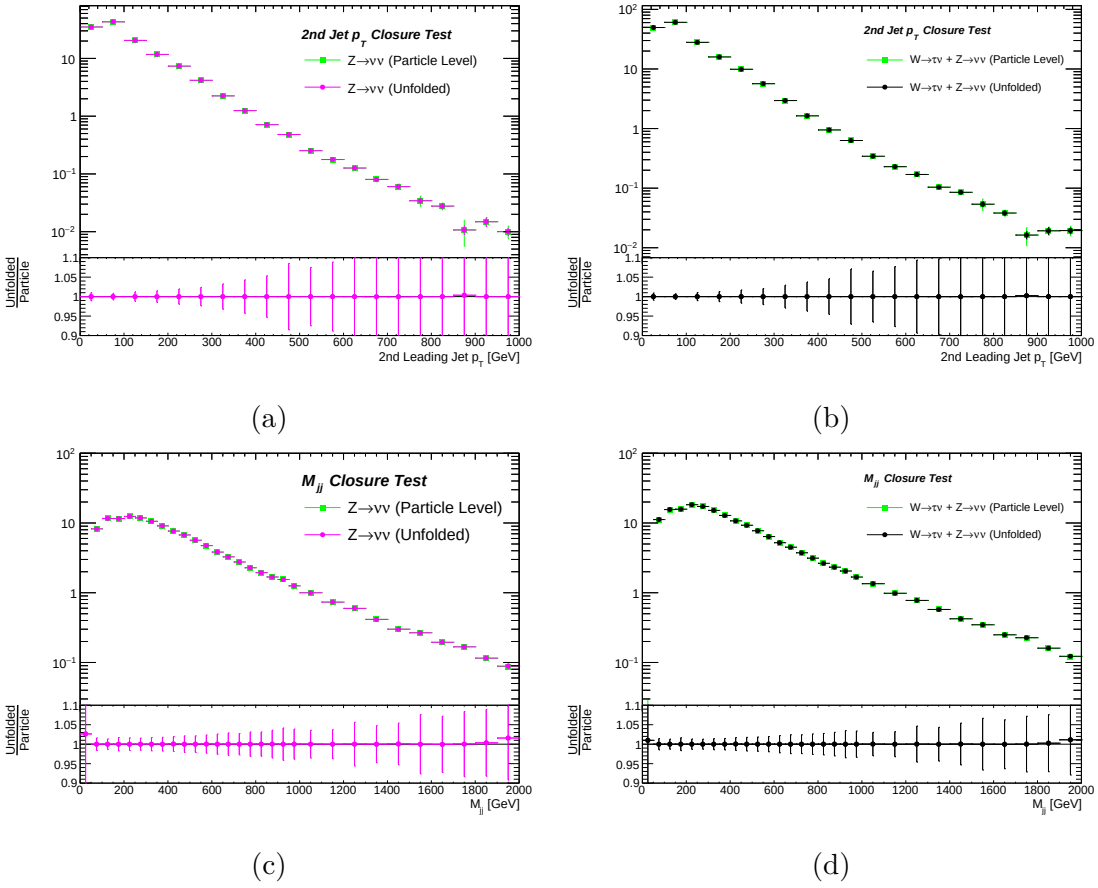

Figure A.3.: The results of the closure test for the transverse momentum of the second leading jet (a,b) and the invariant mass of the two leading jets (c,d) for unfolding the $Z \to \nu\nu$ process (a,c) and for topology unfolding (b,d). The lower plots show the ratio between the unfolded result and the particle level distribution.

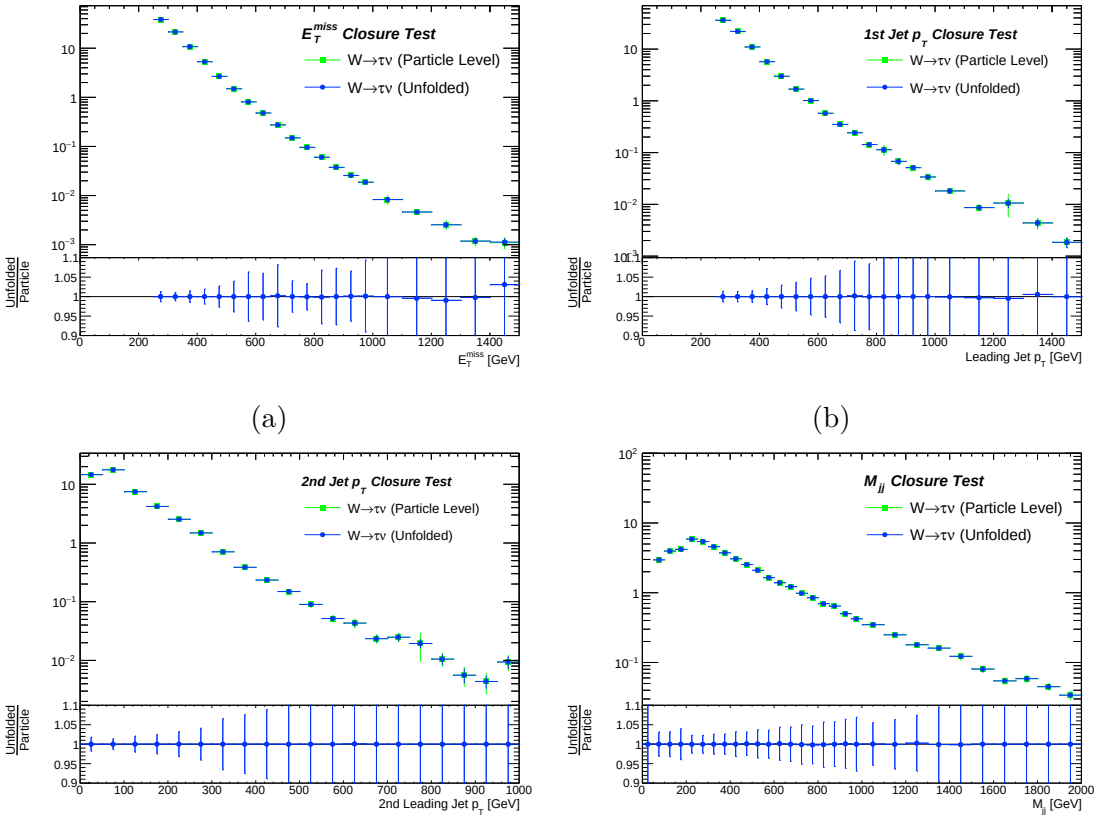

Figure A.4.: The results of the closure test for the missing transverse energy (a), the transverse momentum of the leading (b) and second leading (c) jet as well as for the invariant mass of the two leading jets (d) for unfolding the $W \to \tau\nu$ process. The lower plots show the ratio between the unfolded result and the particle level distribution.

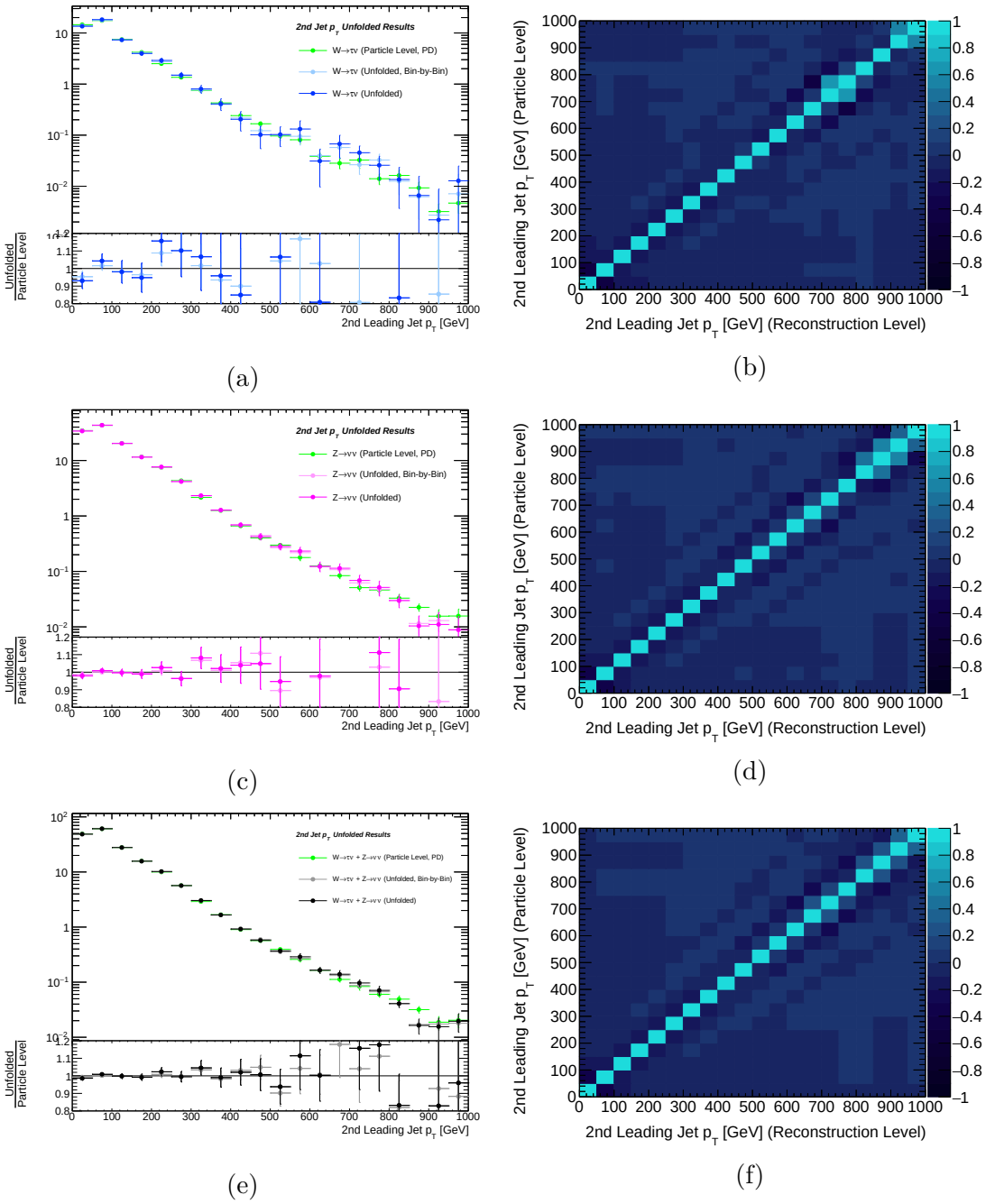

Figure A.5.: Unfolded distributions for the transverse momentum of the second leading jet and the correlation matrices of the statistical uncertainty coming from the reconstructed pseudo-data distribution for unfolding the $W \to \tau\nu$ (a,b), the $Z \to \nu\nu$ (c,d) process and topology unfolding (e,f). The unfolded result is compared to the result obtained from bin-by-bin unfolding and the particle level distribution of the pseudo-data (PD).

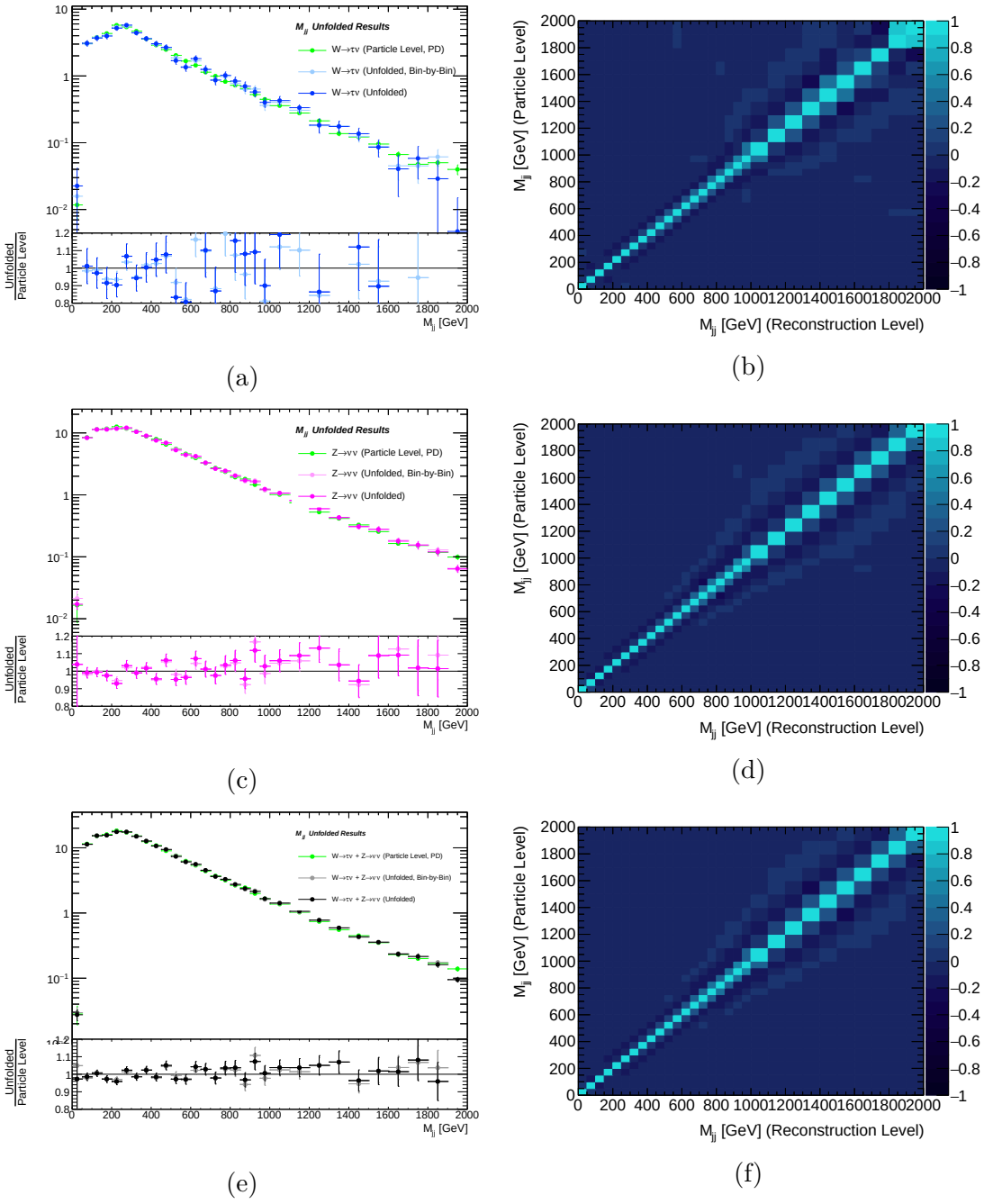

Figure A.6.: Unfolded distributions for the invariant mass of the leading and second leading jet and the correlation matrices of the statistical uncertainty coming from the reconstructed pseudo-data distribution for unfolding the $W \to \tau\nu$ (a,b), the $Z \to \nu\nu$ (c,d) process and topology unfolding (e,f). The unfolded result is compared to the result obtained from bin-by-bin unfolding and the particle level distribution of the pseudo-data (PD). .

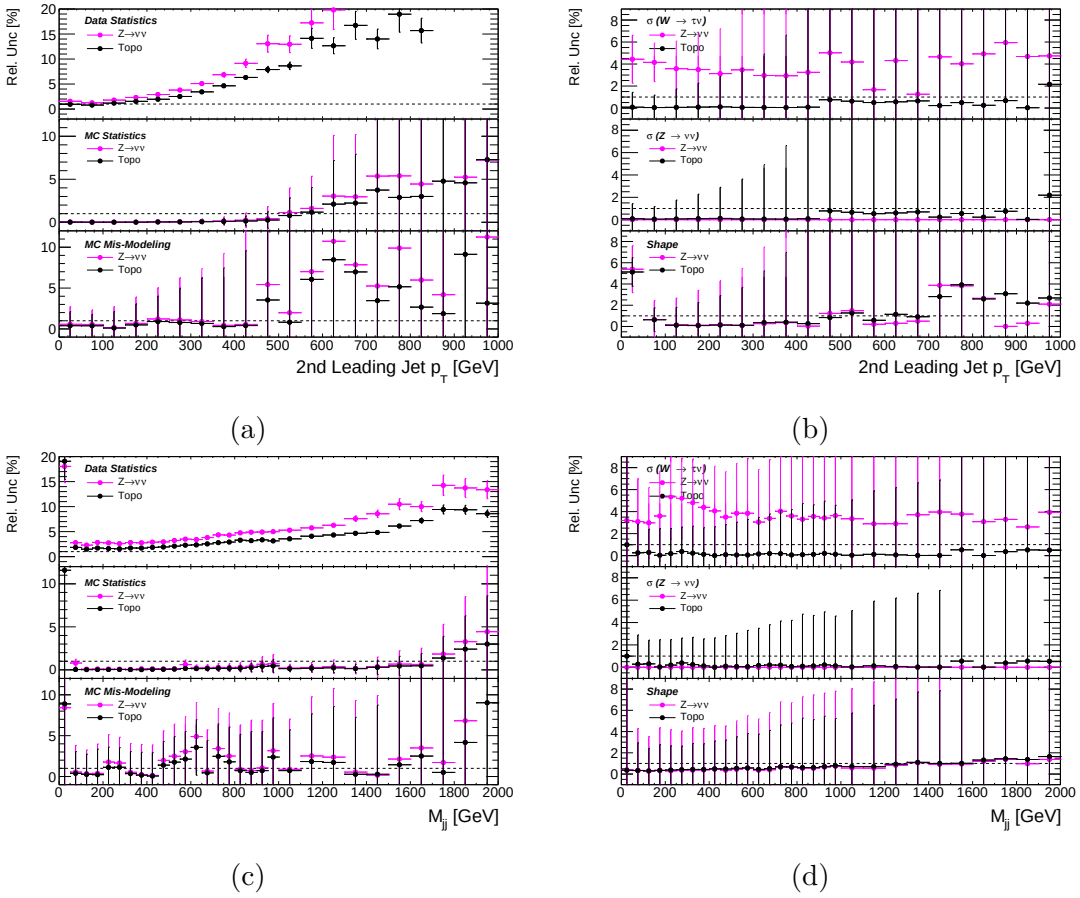

Figure A.7.: Relative uncertainties for the $Z \to \nu\nu$ unfolding (magenta) and the topology unfolding (black) for the transverse momentum of second leading jet (a,b) and the invariant mass of the two leading jets (c,d).

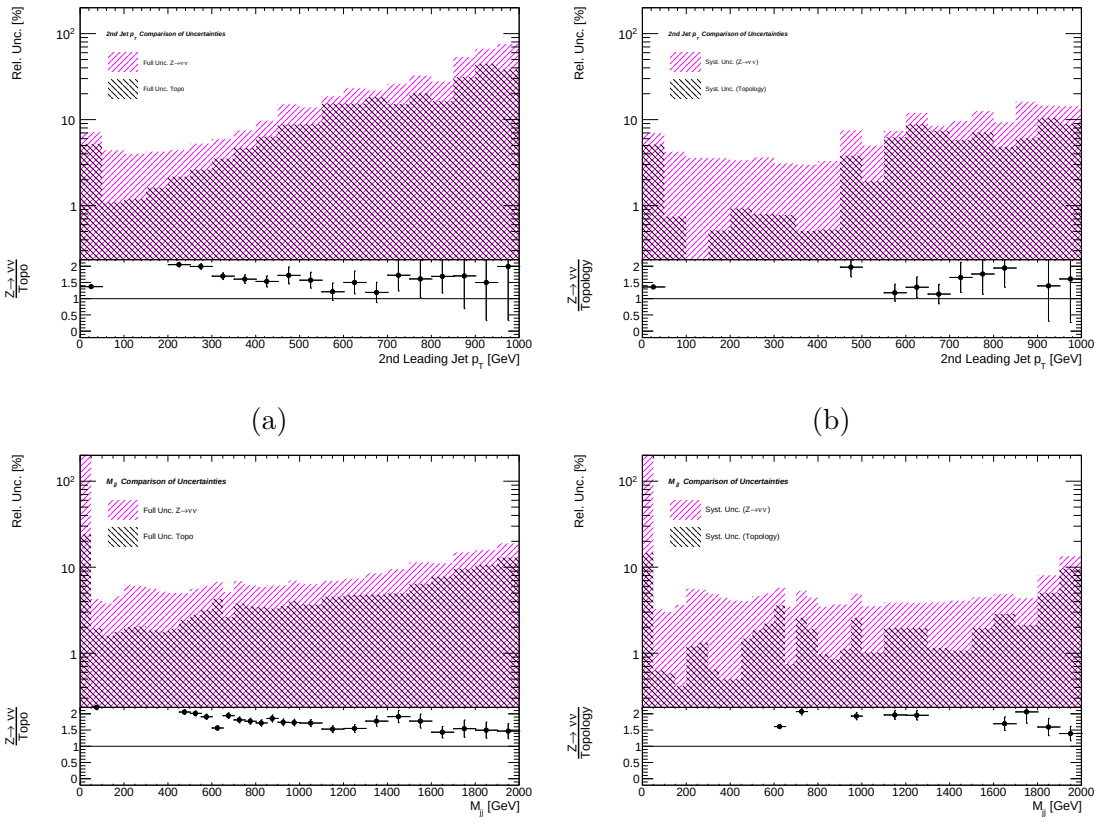

Figure A.8.: Full relative uncertainty (a,b) and the full relative systematic uncertainty (c,d) for the transverse momentum of the second leading jet and the invariant mass of the two leading jets. The lower plots show the ratio of the relative uncertainties of the $Z \to \nu\nu$ unfolding and the topology unfolding.

B. Topology unfolding for a monojet search

B.1. Log-normal Response

This section discusses briefly the idea of the log-normal response. Starting point is a counting experiment in a single phase space region with an observed number of events of N and an expectation of $s + b$, where s refers to the parameter of interest, namely additional contribution from a new process, and b to the expected background events. The background prediction has an uncertainty σ_b. The underlying measurement of the corresponding nuisance parameter is assumed to follow a Gaussian distribution. Therefore, the likelihood is defined as a Poisson distribution times Gaussian with mean b and width σ_b

$$\mathcal{L} = \mathcal{P}(N|s+b) \cdot G(b_0|b, \sigma_b) \tag{B.1}$$

$$= P(N|s+b) \cdot \frac{1}{\sqrt{2\pi\sigma_b^2}} \cdot \exp\left(-\frac{1}{2}\frac{\cdot(b-b_0)^2}{\sigma_b^2}\right). \tag{B.2}$$

Substituting $\theta = (b - b_0)/\sigma_b$ gives

$$\mathcal{L} = \mathcal{P}(N|s+\theta\cdot\sigma_b+b_0) \cdot \frac{1}{\sqrt{2\pi\sigma_b^2}} \cdot \exp\left(-\frac{1}{2}\cdot\theta^2\right) \tag{B.3}$$

$$= \mathcal{P}(N|s+b_0(\frac{\sigma_b}{b_0}\cdot\theta+1)) \cdot \frac{1}{\sqrt{2\pi\sigma_b^2}} \cdot \exp\left(-\frac{1}{2}\cdot\theta^2\right) \tag{B.4}$$

$$= \mathcal{P}(N|s+b_0(\frac{\sigma_b}{b_0}\cdot\theta+1)) \cdot \frac{1}{\sigma_b} \cdot \mathcal{G}(0|\theta, 1), \tag{B.5}$$

with $R(\theta) = (\sigma_b/b_0 \cdot \theta + 1)$ being the response function. Now, the Gaussian is centered around θ and evaluated at zero. θ can be interpreted as the new nuisance parameter. This definition is useful for the case that more than one (overall) uncertainty is considered for b. The new nuisance parameter θ gives the nominal value of b for $\theta = 0$ since $R(\theta = 0) = 1$. However, θ is not bounded from below and can in principle produce negative number of events $R(\theta) \to -\infty$ for $\theta \to -\infty$. This happens predominantly for a small number of expected events. Negative numbers of events should be avoided since they are not physical. This can be done by redefining the response function to the so-called log-normal response:

$$R(\theta) = (\sigma_b/b_0 + 1)^\theta. \tag{B.6}$$

This response function yields again the nominal value of b for $\theta = 0$, but it cannot yield a negative number of events because of the behavior $R(\theta) \to 0$ for $\theta \to -\infty$. Therefore, a good model for the likelihood function is

$$\mathcal{L} = \mathcal{P}\left(N\middle|s + b_0\left(\frac{\sigma_b}{b_0}+1\right)^\theta\right) \cdot \mathcal{G}(0|\theta, 1). \tag{B.7}$$

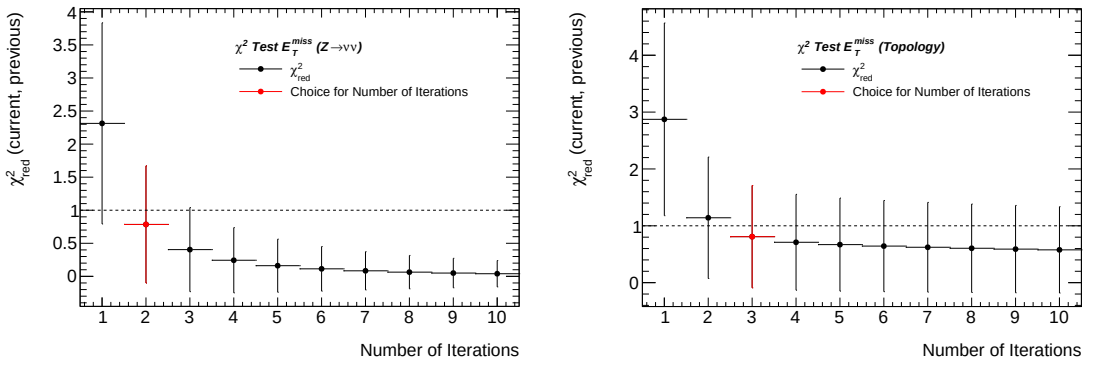

(a) (b)

Figure B.1.: The reduced χ^2 values of the unfolded missing energy distributions from the current and the previous iteration for $Z \to \nu\nu$ unfolding (a) and topology unfolding (b).

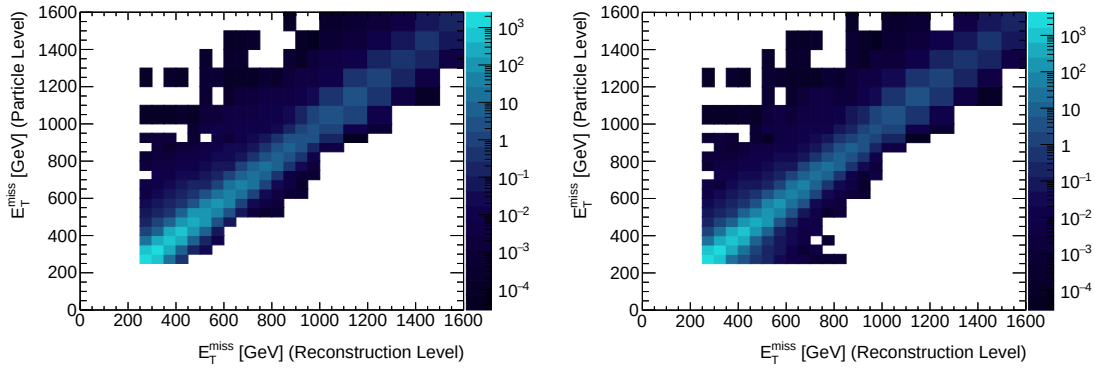

(a) (b)

Figure B.2.: The response matrices for $Z \to \nu\nu$ unfolding (a) and topology unfolding (b).

The constant $1/\sigma_b$ was omitted because it would cancel in a likelihood ratio. The name for this specific response function comes from the fact that $\ln(R) \propto \theta$ and θ is normally distributed.

B.2. Number of iterations

The distribution of the reduced χ^2 values obtained from the current and the previous iteration of unfolding of the missing transverse energy distribution as performed in section 5.3 is shown in figure B.1.

B.3. Response matrices

The response matrices used for unfolding the missing transverse energy distributions in section 5.3 are shown in figure B.2.

Specifications of the ADD model			
n	M_D [GeV]	m_0 [GeV]	σ [pb]
2	5300	800	1.500 ± 0.006
3	4100	1500	1.823 ± 0.006
4	3600	2200	2.289 ± 0.008
5	3200	2800	4.18 ± 0.02
6	3000	3300	7.22 ± 0.03

Table B.1.: Details of the ADD models: the number of extra dimensions n, the fundamental Planck mass M_D, the mass of the graviton m_0 and the cross section σ.

	Uncertainties on the signal cross section σ		
	$\sigma(\sigma_{\mathrm{ADD,Jet/E_T^{miss}}})$	$\sigma(\sigma_{\mathrm{ADD,PDF}})$	$\sigma(\sigma_{\mathrm{ADD,Ren/Fac}})$
$n = 2$	3 %	16 %	23 %
$n = 3$	3 %	22 %	26 %
$n = 4$	3 %	28 %	29 %
$n = 5$	3 %	35 %	32 %
$n = 6$	3 %	42 %	36 %

Table B.2.: Systematic uncertainties for the different ADD models on the signal cross section. The sources for the systematic uncertainties are the jet energy and missing transverse energy scale, the parton density function (PDF) and the renormalization and factorization scale.

B.4. ADD model

Table B.1 shows some details of the five specifications of the ADD model. Given are the number of extra dimensions n, the fundamental Planck mass M_D, the mass of the graviton m_0 and the cross section σ.

The systematic uncertainties on the signal cross section and the signal acceptance are shown in table B.2 and table B.3.

	Uncertainties on the signal acceptance A		
	$\sigma(A_{\mathrm{ADD,Ini/Fin}})$	$\sigma(A_{\mathrm{ADD,PDF}})$	$\sigma(A_{\mathrm{ADD,Ren/Fac}})$
$n = 2$	10 %	10 %	10 %
$n = 3$	10 %	12 %	10 %
$n = 4$	10 %	15 %	10 %
$n = 5$	10 %	17 %	10 %
$n = 6$	10 %	20 %	10 %

Table B.3.: Systematic uncertainties for the different ADD models on the signal acceptance. The sources for the systematic uncertainties are initial and final state modeling, the parton density function (PDF) and the renormalization and factorization scale.

Bibliography

[1] Steven Weinberg. "The Making of the standard model". In: *Eur. Phys. J.* C34 (2004). [,99(2005)], pp. 5–13. DOI: 10.1142/9789812567147_0005,10.1140/epjc/s2004-01761-1. arXiv: hep-ph/0401010 [hep-ph].

[2] Wikipedia. "Standard Model". In: (2016). URL: https://commons.wikimedia.org/wiki/File:Standard_Model_of_Elementary_Particles.svg.

[3] S. L. Glashow. "Partial Symmetries of Weak Interactions". In: *Nucl. Phys.* 22 (1961), pp. 579–588. DOI: 10.1016/0029-5582(61)90469-2.

[4] Georges Aad et al. "Observation of a new particle in the search for the Standard Model Higgs boson with the ATLAS detector at the LHC". In: *Phys. Lett.* B716 (2012), pp. 1–29. DOI: 10.1016/j.physletb.2012.08.020. arXiv: 1207.7214 [hep-ex].

[5] Serguei Chatrchyan et al. "Observation of a new boson at a mass of 125 GeV with the CMS experiment at the LHC". In: *Phys. Lett.* B716 (2012), pp. 30–61. DOI: 10.1016/j.physletb.2012.08.021. arXiv: 1207.7235 [hep-ex].

[6] Y. Fukuda et al. "Evidence for oscillation of atmospheric neutrinos". In: *Phys. Rev. Lett.* 81 (1998), pp. 1562–1567. DOI: 10.1103/PhysRevLett.81.1562. arXiv: hep-ex/9807003 [hep-ex].

[7] Q. R. Ahmad et al. "Measurement of the rate of $\nu_e + d \rightarrow p + p + e^-$ interactions produced by ^8B solar neutrinos at the Sudbury Neutrino Observatory". In: *Phys. Rev. Lett.* 87 (2001), p. 071301. DOI: 10.1103/PhysRevLett.87.071301. arXiv: nucl-ex/0106015 [nucl-ex].

[8] Adam G. Riess et al. "Observational evidence from supernovae for an accelerating universe and a cosmological constant". In: *Astron. J.* 116 (1998), pp. 1009–1038. DOI: 10.1086/300499. arXiv: astro-ph/9805201 [astro-ph].

[9] P. de Bernardis et al. "A Flat universe from high resolution maps of the cosmic microwave background radiation". In: *Nature* 404 (2000), pp. 955–959. DOI: 10.1038/35010035. arXiv: astro-ph/0004404 [astro-ph].

[10] P. Salucci and A. Borriello. "The intriguing distribution of dark matter in galaxies". In: *Lect. Notes Phys.* 616 (2003), pp. 66–77. arXiv: astro-ph/0203457 [astro-ph].

[11] Jörg P Dietrich et al. "A filament of dark matter between two clusters of galaxies". In: *Nature* 487.7406 (2012), pp. 202–204.

[12] Pieter van Dokkum et al. "A high stellar velocity dispersion and 100 globular clusters for the ultra-diffuse galaxy Dragonfly 44". In: *The Astrophysical Journal Letters* 828.1 (2016), p. L6.

[13] G't Hooft. "Naturalness, chiral symmetry, and spontaneous chiral symmetry breaking". In: *Recent Developments in Gauge Theories* (1980), pp. 135–157.

[14] Nima Arkani-Hamed, Savas Dimopoulos, and G. R. Dvali. "The Hierarchy problem and new dimensions at a millimeter". In: *Phys. Lett.* B429 (1998), pp. 263–272. DOI: 10.1016/S0370-2693(98)00466-3. arXiv: hep-ph/9803315 [hep-ph].

[15] Lyndon Evans and Philip Bryant. "LHC Machine". In: *JINST* 3 (2008), S08001. DOI: 10.1088/1748-0221/3/08/S08001.

[16] Mark Thomson. *Modern particle physics*. Cambridge University Press, 2013.

[17] G. Aad et al. "The ATLAS Experiment at the CERN Large Hadron Collider". In: *JINST* 3 (2008), S08003. DOI: 10.1088/1748-0221/3/08/S08003.

[18] Joao Pequenao. "Computer generated image of the whole ATLAS detector". In: (2008). URL: http://cds.cern.ch/record/1095924.

[19] M Capeans et al. "ATLAS Insertable B-Layer Technical Design Report". In: CERN-LHCC-2010-013. ATLAS-TDR-19 (2010). URL: http://cds.cern.ch/record/1291633.

[20] Joao Pequenao. "Computer generated image of the ATLAS inner detector". In: (2008). URL: http://cds.cern.ch/record/1095926.

[21] "Vertex Reconstruction Performance of the ATLAS Detector at $\sqrt{s} = 13$ TeV ". In: ATL-PHYS-PUB-2015-026 (2015). URL: http://cds.cern.ch/record/2037717.

[22] Ewa Stanecka. "ATLAS Inner Tracker Performance at the beginning of LHC Run-2." In: ATL-INDET-PROC-2016-002 (2016). URL: https://cds.cern.ch/record/2147407.

[23] Georges Aad et al. "Muon reconstruction performance of the ATLAS detector in proton–proton collision data at $\sqrt{s}$ =13 TeV". In: *Eur. Phys. J.* C76.5 (2016), p. 292. DOI: 10.1140/epjc/s10052-016-4120-y. arXiv: 1603.05598 [hep-ex].

[24] M Aharrouche et al. "Energy linearity and resolution of the ATLAS electromagnetic barrel calorimeter in an electron test-beam". In: *Nuclear Instruments and Methods in Physics Research* 568.2 (2006), pp. 601–623.

[25] T Davidek et al. "ATLAS Tile Calorimeter performance for single particles in beam tests". In: *Journal of Physics: Conference Series*. Vol. 160. 1. IOP Publishing. 2009, p. 012057.

[26] B. Dowler et al. "Performance of the ATLAS hadronic end-cap calorimeter in beam tests". In: *Nucl. Instrum. Meth.* A482 (2002), pp. 94–124. DOI: 10.1016/S0168-9002(01)01338-9.

[27] J. P. Archambault et al. "Energy calibration of the ATLAS liquid argon forward calorimeter". In: *JINST* 3 (2008), P02002. DOI: 10.1088/1748-0221/3/02/P02002.

[28] Joao Pequenao. "Computer Generated image of the ATLAS calorimeter". In: (2008). URL: http://cds.cern.ch/record/1095927.

[29] Joao Pequenao. "Computer generated image of the ATLAS Muons subsystem". In: (2008). URL: http://cds.cern.ch/record/1095929.

[30] Antonio Salvucci. "Measurement of muon momentum resolution of the ATLAS detector". In: *EPJ Web Conf.* 28 (2012), p. 12039. DOI: 10.1051/epjconf/20122812039. arXiv: 1201.4704 [physics.ins-det].

[31] Morad Aaboud et al. "Performance of the ATLAS Trigger System in 2015". In: (2016). arXiv: 1611.09661 [hep-ex].

[32] Francesca Pastore. "ATLAS Run-2 status and performance". In: (2015). URL: https://cds.cern.ch/record/2032788.

[33] Bo Andersson et al. "Parton Fragmentation and String Dynamics". In: *Phys. Rept.* 97 (1983), pp. 31–145. DOI: 10.1016/0370-1573(83)90080-7.

[34] B. R. Webber. "A QCD Model for Jet Fragmentation Including Soft Gluon Interference". In: *Nucl. Phys.* B238 (1984), pp. 492–528. DOI: 10.1016/0550-3213(84)90333-X.

[35] Matteo Cacciari, Gavin P. Salam, and Gregory Soyez. "The Anti-k(t) jet clustering algorithm". In: *JHEP* 04 (2008), p. 063. DOI: 10.1088/1126-6708/2008/04/063. arXiv: 0802.1189 [hep-ph].

[36] Jeffrey Rogers Dandoy et al. "Jet energy scale measurements and their systematic uncertainties in proton-proton collisions at $\sqrt{s} = 13$ TeV with the ATLAS detector". In: ATL-COM-PHYS-2016-213 (2016). URL: https://cds.cern.ch/record/2136864.

[37] Georges Aad et al., The ATLAS collaboration. "Selection of jets produced in 13TeV proton-proton collisions with the ATLAS detector". In: (2015). URL: http://cds.cern.ch/record/2037702.

[38] G. D'Agostini. "A Multidimensional unfolding method based on Bayes' theorem". In: *Nucl. Instrum. Meth.* A362 (1995), pp. 487–498. DOI: 10.1016/0168-9002(95)00274-X.

[39] Tim Adye. "Unfolding algorithms and tests using RooUnfold". In: *Proceedings, PHYSTAT 2011 Workshop on Statistical Issues Related to Discovery Claims in Search Experiments and Unfolding, CERN,Geneva, Switzerland 17-20 January 2011*. CERN. Geneva: CERN, 2011, pp. 313–318. DOI: 10.5170/CERN-2011-006.313. arXiv: 1105.1160 [physics.data-an]. URL: https://inspirehep.net/record/898599/files/arXiv:1105.1160.pdf.

[40] C. Patrignani et al., Particle Data Group. "Review of Particle Physics". In: *Chin. Phys.* C40.10 (2016), p. 100001. DOI: 10.1088/1674-1137/40/10/100001.

[41] Morad Aaboud et al., ATLAS Collaboration. "Search for new phenomena in final states with an energetic jet and large missing transverse momentum in *pp* collisions at $\sqrt{s} = 13$TeV using the ATLAS detector". In: *Phys. Rev.* D94.3 (2016), p. 032005. DOI: 10.1103/PhysRevD.94.032005. arXiv: 1604.07773 [hep-ex].

[42] Georges Aad et al. "Measurement of the muon reconstruction performance of the ATLAS detector using 2011 and 2012 LHC proton–proton collision data". In: *Eur. Phys. J.* C74.11 (2014), p. 3130. DOI: 10.1140/epjc/s10052-014-3130-x. arXiv: 1407.3935 [hep-ex].

[43] Georges Aad et al., ATLAS Collaboration. "Muon reconstruction performance of the ATLAS detector in proton–proton collision data at $\sqrt{s}$ =13 TeV". In: *Eur. Phys. J.* C76.5 (2016), p. 292. DOI: 10.1140/epjc/s10052-016-4120-y. arXiv: 1603.05598 [hep-ex].

[44] Georges Aad et al., ATLAS Collaboration. "Electron efficiency measurements with the ATLAS detector using the 2015 LHC proton-proton collision data". In: (2016).

[45] Georges Aad et al., ATLAS Collaboration. "Photon identification in 2015 ATLAS data". In: ATL-PHYS-PUB-2016-014 (2016). URL: https://cds.cern.ch/record/2203125.

[46] Georges Aad et al., ATLAS Collaboration. "Performance of missing transverse momentum reconstruction for the ATLAS detector in the first proton-proton collisions at at $\sqrt{s}$= 13 TeV". In: ATL-PHYS-PUB-2015-027 (2015). URL: https://cds.cern.ch/record/2037904.

[47] Elisabetta Luigia Barberio et al. "Search for new phenomena in monojet plus missing transverse momentum final states in pp collisions at $\sqrt{s} = 13$ TeV with the ATLAS detector". In: ATL-COM-PHYS-2015-296 (2015). URL: https://cds.cern.ch/record/2010840.

[48] Remi Lafaye, Tilman Plehn, and Dirk Zerwas. "SFITTER: SUSY parameter analysis at LHC and LC". In: (2004). arXiv: hep-ph/0404282 [hep-ph].

[49] Tim Adye. "Unfolding algorithms and tests using RooUnfold". In: (2011), pp. 313–318. DOI: 10.5170/CERN-2011-006.313. arXiv: 1105.1160 [physics.data-an]. URL: https://inspirehep.net/record/898599/files/arXiv:1105.1160.pdf.

[50] ATLAS Collaboration. "Public plots: Jet energy scale uncertainties updated for ICHEP 2016 using full 13 TeV 2015 dataset". In: (2016). URL: https://atlas.web.cern.ch/Atlas/GROUPS/PHYSICS/PLOTS/JETM-2016-010/.

[51] Alexander L. Read. "Presentation of search results: The CL(s) technique". In: *J. Phys.* G28 (2002). [,11(2002)], pp. 2693–2704. DOI: 10.1088/0954-3899/28/10/313.

[52] *Procedure for the LHC Higgs boson search combination in Summer 2011*. Tech. rep. CMS-NOTE-2011-005. ATL-PHYS-PUB-2011-11. Geneva: CERN, 2011. URL: https://cds.cern.ch/record/1379837.

[53] Glen Cowan et al. "Asymptotic formulae for likelihood-based tests of new physics". In: *Eur. Phys. J.* C71 (2011). [Erratum: Eur. Phys. J.C73,2501(2013)], p. 1554. DOI: 10.1140/epjc/s10052-011-1554-0,10.1140/epjc/s10052-013-2501-z. arXiv: 1007.1727 [physics.data-an].

[54] Abraham Wald. "Tests of statistical hypotheses concerning several parameters when the number of observations is large". In: *Transactions of the AMS* 54.3 (1943), pp. 426–482.

[55] S. Alekhin et al. "HERAFitter". In: *Eur. Phys. J.* C75.7 (2015), p. 304. DOI: 10.1140/epjc/s10052-015-3480-z. arXiv: 1410.4412 [hep-ph].

Acknowledgements

First of all, I would like to thank Monica and Pavel for supervising me throughout this project and Prof. Tilman Plehn for co-reviewing this thesis. It was fun! Many thanks also to Prof. Schultz-Coulon for letting me and to Alessandra for getting me into the KIP ATLAS group in the first place as well as motivating me for the CERN summer student program.

For reading parts of this thesis and providing feedback I would like to thank Julia, Hanno, Pavel and Clara. Special thanks goes to Anja Butter and Tilman Plehn for helping me understand the point of view of a theoretician when it comes to using LHC data and combining ATLAS analyses in order to set limits on theoretical models. Thanks also to my awesome office mates Thomas, Merve and Farbizio. It was a blast!

Most important, I want to thank the whole ATLAS and ILC group of KIP for a splendid time and a lot of support in many ways.

Erklärung:

Ich versichere, dass ich diese Arbeit selbstständig verfasst habe und keine anderen als die angegebenen Quellen und Hilfsmittel benutzt habe.

Heidelberg, den 15.12.2016 .....